Hierarchical Design and Simulation of Tissue Engineering Scaffold Mechanical, Mass Transport, and Degradation Properties

by

Hee Suk Kang

A dissertation submitted in partial fulfillment
of the requirements for the degree of
Doctor of Philosophy
(Mechanical Engineering)
in The University of Michigan
2010

Doctoral Committee:

Professor Scott J. Hollister, Co-Chair
Assistant Research Professor Chia-Ying Lin, Co-Chair
Professor Noboru Kikuchi
Associate Professor Trachette L. Jackson

To Minyoung, Minkyu and Hyunkyu

ACKNOWLEDGMENTS

I would like to express sincere appreciation to Professor Scott J. Hollister, who gave me this wonderful opportunity, endless support with patience and invaluable guidance during this PhD study at the University of Michigan, Ann Arbor. I gratefully acknowledge the practical guidance from Professor Chia-Ying Lin for his valuable advice and thoughtful attention. I also would like to sincerely acknowledge the helpful suggestions and guidance by my doctoral committee members, Professor Noboru Kikuchi and Professor Trachette L Jackson. In addition, my special thanks are expressed to Dr Frank LaMarca and Dr Paul Park, in the Department of Neurosurgery, who broadened my understanding of the scientific and clinical aspects of spine biomechanics studies.

Without help from my colleagues and friends in the Scaffold Tissue Engineering Group and Spine Research Laboratory, I would not have made it through this long tunnel: Brandon Busuito, Shelley Brown, Alisha Diggs, Colleen Flanagan, Claire Jeong, Leena Jongpaiboonkit, Jessica Kemppainen, Elly Liao, Sara Mantila, Francesco Migneco, Annie Mitsak, Erin Moffitt, Chan-Ho Park, Eiji Saito, Rachel Schek, Auresa Thomas, Louis Tseng, Frank Winterroth, Darice Wong, Huina Zhang, and Lin Wang.

To Ann Arbor Hope Church members including pastor Tom Humpreys and Hunseok Bae, I would also like to express special thanks for their prayers and encouragements. I especially appreciate the guidance and support of pastor in Korea,

Heechang Kang, in my life and belief. I also extend my gratitude for the support of all the members of the 2004 Korean Mechanical Engineering Student. My very special thanks go to Jeonghun Seo for his discussion and advice regarding topology optimization and to Taekyung Lee for his advice on practical FE modeling techniques. My special thanks are expressed to Mini Adam for her time instructing me in effective editing in English.

Lastly, I would like to express my sincere gratitude to my parents and parent-in-laws for their love, support and encouragement. To my sons, Minkyu and Hyunkyu, who were given to us during this period, my greatly thanks for their growing-up without any problems. Finally, to my wife, Minyoung, my warmest thanks for your endurance and long sacrificing support during this period.

TABLE OF CONTENTS

DEDICATION ..... **ii**

ACKNOWLEDGMENTS ..... **iii**

LIST OF FIGURES ..... **viii**

LIST OF TABLES ..... **xiii**

ABSTRACT ..... **xiv**

CHAPTER 1 INTRODUCTION **1**

1.1 Overview 1

1.2 Integrated Design Framework for Tissue Engineering Scaffolds 4

1.2.1 The Tissue Engineering Scaffold 6

1.2.2 The Homogenization Theory 9

1.2.3 Topology Optimization 12

1.2.4 Solid Freeform Fabrication 16

1.3 Biodegradable Fusion Cages 17

1.3.1 Spinal Fusion Cages 17

1.3.2 Biodegradable Cages 19

1.3.3 Design of Porous Biodegradable Fusion Cages Using the Integrated Global-Local Topology Optimization 21

1.4 Hydrolytic Degradation of Biodegradable Polymers 21

1.5 Outline of Thesis 25

CHAPTER 2 HOMOGENIZATION of scaffold mechanical and mass transport properties **27**

2.1 Overview 27

2.2 Preliminary 29

2.3 Homogenization of Linear Elasticity 30

2.4 Homogenization of Diffusion 33

2.5 Implementation of the Homogenization of Elasticity and Diffusivity 36

2.6 Cross-Property Bounds on Diffusivity and Bulk Modulus....36
2.7 Homogenization of a Diffusion-Reaction Equation in Porous Media....39
2.7.1 Derivation....39
2.7.2 Solution Process....47
2.8 Homogenization of Stokes Flow....48
2.8.1 Derivation....48
2.8.2 Implementation and Validation....53
2.9 Conclusion....55

CHAPTER 3 SCAFFOLD MICROSTRUCTURE DESIGN USING THE MICROSCTRUCTURAL OPTIMIZATION....56

3.1 Introduction....56
3.2 Tailoring Scaffold Properties....59
3.2.1 Material Interpolations....59
3.2.2 Problem Statement for Target Optimization....60
3.2.3 Implementation....61
3.3 Results....62
3.3.1 Microstructures with High Diffusivity....63
3.3.2 Microstructures with Low Diffusivity....65
3.3.3 Microstructure targeting Low Diffusivity and Low Bulk Modulus....68
3.3.4 Microstructures with the same porosity but different bulk modulus and diffusivity 69
3.3.5 Comparison of Designed Properties with Experimental Measurements....71
3.4 Discussion....75

CHAPTER 4 POROUS BIODEGRADABLE INTERBODY FUSION CAGE DESIGN USING THE INTEGRATED GLOBAL-LOCAL TOPOLOGY OPTIMIZATION....80

4.1 Overview....80
4.2 Fusion Cage Design by Integrated Global-Local Topology Optimization....83
4.2.1 Finite Element Modeling for the Global Topology Optimization....83
4.2.2 Microstructure Design using Local Topology Optimization....87
4.2.3 Fusion Cage Design for an in situ large animal model....88
4.2.4 Fabrication and Testing:....89
4.3 Results....91
4.3.1 Global Density Map and Local Microstructures....92
4.3.2 Integrated Design....97
4.3.3 Fabrication and Mechanical Test....98
4.3.4 Estimation of Yield from the Stress Analysis....103
4.4 Discussion....106

CHAPTER 5 Multiscale Modeling of Hydrolytic Degradation of Hierarchical Scaffolds.....113

5.1 Introduction.....113

5.1.1 Hydrolysis Kinetics: Autocatalysis.....116

5.2 Computational Modeling of Hydrolytic Degradation.....119

5.2.1 Diffusion-Reaction Based Model for Erosion Mechanisms.....119

5.2.2 Heterogeneous Degradation in Bulk Erosion.....123

5.2.3 Degradation of Porous Scaffolds.....128

5.3 Homogenization Model for Hydrolytic Degradation of Porous Scaffold.....131

5.3.1 The Governing System of Equations.....131

5.3.2 Investigation of the Macroscopic Equation.....134

5.3.3 Evaluation of the Non-Dimensional Parameters.....137

5.3.4 Solving the coupled Multiscale Degradation Model.....138

5.3.5 Results.....139

5.4 Conclusion and Future Work.....143

CHAPTER 6 CONCLUSION.....145

6.1 Summary and Conclusion.....145

6.2 Future Study.....148

BIBLIOGRAPHY.....151

LIST OF FIGURES

Figure 1.1 Hierarchical structure of long bone from lacunar-canliculi network through trabecular and cortical bones to whole bone level. The properties of tissue engineering scaffolds are compared at the whole bone level (Liebschner and Wettergreen 2003). 5

Figure 1.2 Schematic diagram of the complex interplay between degradation of the scaffold and tissue regeneration. From initial scaffold fabrication through cell/tissue culture in vitro and in vivo remodeling of the tissue, the scaffold-tissue construct is expected to maintain the desired functional properties. (Hutmacher 2000) 8

Figure 1.3 Homogenization process finds a macroscopic equivalent (averaged) description from the analysis of the local microstructure. 10

Figure 1.4 Illustration of (a) size optimization, (b) shape optimization, and (c) topology optimization. (figure from (Guest 2005))..... 13

Figure 1.5 Microstructures are designed to match the bulk modulus (K^H) and diffusivity (D^H) of a porous scaffold with those of normal healthy tissue (K^* and D^*, respectively). 15

Figure 1.6 Structural formula of PLA, PGA, and PCL (Ueda and Tabata 2003)..... 22

Figure 2.1 Normalized theoretical bounds on isotropic diffusivity and bulk modulus plotted as a function of solid phase volume fraction..... 38

Figure 2.2 An example of cross-property bounds on the effective bulk modulus and diffusivity for ill-ordered composite, adapted from Gibiansky and Torquato (Gibiansky and Torquato 1996). 38

Figure 2.3 Schematic of a unit microstructure domain, showing two sub-regions with different diffusivities. 40

Figure 2.4 Unit microstructure of Wigner-Seitz grain, from (Lee et al. 1996). 54

Figure 2.5 The effective permeability by the homogenization code was compared to an empirical formulation used in (Lee et al. 1996). 54

Figure 3.1 Microstructures obtained by targeting bulk modulus and diffusivity close to the upper cross-property bounds, for 30% porosity (a, b and c), 50% porosity (d, e and f) and 60% porosity (g and h)..... 64

Figure 3.2 Microstructures designed to achieve properties close to the upper cross-property bounds are specified within the cross-property bounds..... 66

Figure 3.3 The achieved diffusivities (upper) and bulk moduli (lower) were compared with target properties for the microstructures presented in Figure 3.1 67

Figure 3.4 (A) Microstructures with low diffusivity and low bulk modulus, (B) 1/8 of the designed microstructure and (C) representative cross-sectional view of the structure. 68

Figure 3.5 Microstructure designs with ranges of diffusivities for 50% porosity 70

Figure 3.6 Scaffolds with optimal microstructures were designed and fabricated using SFF. 72

Figure 3.7 Stress-strain curves obtained from compression tests of the fabricated scaffolds designed with the optimal microstructures. 73

Figure 3.8 Theoretical Young's modulus was correlated to experiments. 74

Figure 3.9 Histograms of densities of three microstructure designs targeting K = 0.2 and D = 0.3, K = 0.15 and D = 0.2, and K = 0.1 and D = 0.1 78

Figure 4.1 Ligamentous finite element models of minipig lumbar spine segments (L2~L5) and the design domain for the global topology optimization at L4-L5 level. 84

Figure 4.2. Global density maps obtained using the global topology optimization, under (A) flexion, (B) extension, (C) lateral bending and (D) torsion. (E) represents the combination of all loading modes used for the final integrated design. 93

Figure 4.3 Segmented global density maps, under (A) flexion, (B) extension, (C) lateral bending and (D) torsion. (E) represents the combination of all loading modes used for the final integrated design. 94

Figure 4.4. All the property pairs of the microstructures are on the cross-property upper bounds, which indicates the microstructures are optimal. (A) and (C) were designed using the microstructural topology optimization and (B) and (D) were designed using primitive pore geometry (cylindrical holes). 95

Figure 4.5 Final integrated design of the porous fusion cage. (A) Top, side, and isometric views of the optimized pore architecture, and (B) final integrated design with detailed geometric features. 99

Figure 4.6 (A) A prototype fabricated using SFF and (B) prototypes scaled to fit the minipig (upper) and human(lower) intervetebral disc spaces. (C) The customized cage was checked in the domestic pig lumbar intervertebral disc space. 99

Figure 4.7. For compression tests, the the fusion cages (A) with cylindrical pore microstructures and (B) with optimized microstructures, and the conventional TLIF cage were fabricated without detailed features to eliminate the initial yield caused by the teeth-like geometric features. 101

Figure 4.8 Compression test results confirmed that the superior stiffness and strength of the optimized designs over the conventional TLIF design. 101

Figure 4.9 Stress-strain curve obtained from the compression test of a bulk cylindrical specimen to determine the Young's modulus and yield stress for the finite element analysis. 102

Figure 4.10 (A) Von Mises stress level for optimal fusion cage without pore structures is below the yield stress (8.5 MPa). With initial pore structures (B) and (C), the stress level increased over the yield compared to (A). However, after initial bony fusion inside the pores (D) and (E), the stress level decreased below the yield (9 MPa). These results indicate that major loading support is provided by outer wall. Although local yield at the microstructures increases initially, ingrown bone will take over the loads from the fusion cage, alleviating the load burden at the microstructures. 104

Figure 4.11 Cummulative histogram of von Mises stress distribution (dotted curves) and Weibull fittings (solid curves) over the entire voxels under different compressive loads. Computationally predicted maximum load was (A) Fy=1403 N for fusion cage with cylindrical pores and (B) Fy=1724 N for fusion cage with optimal pores..... 105

Figure 4.12 The deformation of the optimal fusion cage under compression up to 50% strain showed typical behavior of ductile material..... 109

Figure 5.1 Acid-catalyzed hydrolysis reaction 117

Figure 5.2 The diffusion reaction problem in a large plate of PLA is approximated as one dimensional problem. 122

Figure 5.3 Bulk erosion occurs if water diffusion is much faster than the hydrolysis reaction(ε_W=100), and surface erosion occurs when water diffusion is much slower than hydrolysis(ε_W=0.01). The X axis is perpendicular to polymer plate with its origin at the center of the thickness. The local ester bond concentration along the x axis was assumed to be proportional to the local molecular weight. 123

Figure 5.4 Heterogeneous erosion was simulated with different ε_A and $\bar{k}_{12}$ values. Larger ε_A tends to increase heterogeneity in the ester bond concentration while larger $\bar{k}_{12}$ accelerates the overall degradation speed. 126

Figure 5.5 Molecular weight profiles (degradation) along time were demonstrated with different ε_A and $\bar{k}_{12}$ values: The left hand plot is for $\bar{k}_{12}$=0.1 with varying ε_A, the center plot is for $\bar{k}_{12}$=1, and the right hand plot is for $\bar{k}_{12}$=10. For $\bar{k}_{12}$ =10, the effect of ε_A vanishes. (curves in green: ε_A=0.1, curves in blue: ε_A =1, and curves in red: ε_A=10) 126

Figure 5.6 Fluxes of the small carboxylic acid end groups out of the polymer matrix were plotted over simulation time with varying ε_A values..... 127

Figure 5.7 The simulation domain consists of 2x2x2 unit microstructure array (implemented by symmetric boundary conditions), and surrounding medium. 129

Figure 5.8 Comparison of molecular weight profiles between scaffolds with 2mm and 5mm unit microstructures. Scaffold with large unit microstructures degrade faster than those with small unit microstructures. 129

Figure 5.9 Molecular weight profiles were compared among scaffolds with different strut size microstructures. Larger strut size, or thickness, were shown to be related to faster degradation. 131

Figure 5.10 Without considering porosity at the time derivative term, the effective diffusivity affects the flux profile..... 136

Figure 5.11 Effluxes were measured for a bell shaped time dependent source term. The effect of the effective diffusivity (D^H) was not observed..... 136

Figure 5.12 Schematics of the simulation domain. An infinite plate was modeled one dimensional problem, where x=0 at the center of the plate and x=1 at the plate surface. two dimensional microscopic domains were defined at five sampling points in the global domain for the local boundary value problems. Local boundary flux serves as a global source term. 138

Figure 5.13 Characteristic concentration distribution in the pore domain. Volume averaging gives the effective diffusivity. 139

Figure 5.14 The change of distribution of carboxlyic acid end group concentrations were plotted at different time points. Note that at x=0, acid concentration is maximum while its time derivative is zero. Also note that at x=1, acid concentration is zero while its time derivative is maximum. 140

Figure 5.15 (A) Nondimensionalized efflux of carboxylic acid end groups at five representative unit microstructures were plotted as the simulation time. (B) Nondimensionalized efflux of carboxylic acid end groups at the boundary (x=1) of the global domain. 140

Figure 5.16 Normalized ester bond concentration (molecular weight profile) within the polymer matrix (solid region of porous scaffold) was demonstrated for k_1=0.35, k_2=0.1, D^H=0.343, and D_2=1.0. 142

Figure 5.17 The cumulative efflux from the outer surface of the infinite plate (x=1). 142

LIST OF TABLES

Table 3.1 Properties of microstructures tailored with target bulk moduli and diffusivities. 65

Table 3.2 Comparison of theoretical Young's modulus calculated from the homogenization method, and experimental Young's modulus measured compression tests. 74

Table 4.1 Mechanical Properties of Components of the Finite Element Models..... 85

Table 4.2 Mechanical and mass transport properties of the microstructures used in the design of porous fusion cages. 96

Table 4.3 Stiffness and yield loads of two designed cages with and without microstructures were compared with those of conventional TLIF cage and PLLA cages in reference (van Dijk et al. 2003). 97

Table 4.4 Surface to volume ratio of the microstructures used in this study 111

Table 5.1 Autocatalytic hydrolysis reaction rates of linear aliphatic polymers (Pitt et al. 1981; Antheunis et al. 2009). 119

Table 5.3 Parameters used in this study. 137

ABSTRACT

Hierarchical Design and Simulation of Tissue Engineering Scaffold Mechanical, Mass Transport, and Degradation Properties

by

Hee Suk Kang

Co-Chairs: Scott J. Hollister and Chia-Ying Lin

In this study, a computational design framework was developed and demonstrated for hierarchical scaffold mechanical, mass transport and degradation properties. As a composite, multiscale structure, the tissue engineering scaffold should be designed to match tissue specific requirements such as tissue elastic modulus and diffusivity/permeability, for better tissue regeneration. In addition to these functional properties, the design of the tissue engineering scaffolds should include the time dependent change of the functions along with material degradation and erosion. With the aid of multiscale homogenization method and topology optimization technique, scaffold microstructures were designed and applied to the design of biodegradable spinal fusion cages. The degradation characteristics by the presence of microstructures were addressed using multiscale homogenization model of diffusion reaction system.

The mechanical properties (bulk modulus) of the topology optimized microstructures range from 10% to 37% of base material property, whereas the mass

transport properties (diffusivity) range from 12% to 41% of free diffusivity. The designed properties were optimal within known cross-property bounds connecting diffusivity and bulk modulus. Mechanical compression test confirmed the good correlation between the designed and experimentally measured Young's moduli. As a clinical application, the topology optimization technique was adapted to the design of biodegradable fusion cages with the integrated global-local topology optimization. The mechanical strength of the fusion cage made of PCL was demonstrated to support physiological loads at human lumbar spine. Degradation of the porous scaffolds was characterized using a multiscale homogenization technique, demonstrating the effect of the release profiles of acidic products from polymer hydrolysis at local microstructure scale on the release at the global scaffold scale.

The precise characterization and controlled design and fabrication within same theoretical framework will provide the basis of a consistent knowledge regarding the correlation between scaffold design parameters and the tissue regeneration.

CHAPTER 1

INTRODUCTION

1.1 Overview

As recent engineering and technology demand materials with more functions at lower cost, the needs for tailoring material properties have increased in the design of composite material. Composite materials, due to its inherent versatility offered by their different components and hierarchies, are currently widely investigated, especially as potential replacements for naturally occurring composite, such as biological tissue. However, the analysis and characterization of composites is extremely difficult due to its complex hierarchical structures. Intuitively, various combinations of the material constituents, as well as their configurations, alter the properties of the composite, whereas the pore configuration, or pore architecture, is one of the main design parameters that control the properties of the composite.

Computational multiscale modeling methods, such as the homogenization method, can provide rigorous and efficient theoretical background for the analysis and characterization of the hierarchical structures by connecting the pore architecture to the effective properties of the composite. Such multiscale modeling is crucial to the

engineering of tissue scaffolds which, in turn, are keys to tissue regeneration, supporting and guiding cells, as well as delivering biologics and external stimuli through the pores. The aim of engineered tissue scaffolds is to provide temporary support for cells, mimicking the roles of the natural extracellular matrix (ECM) (Hollister et al. 2009). ECM not only provides structural support to the cells within, but also actively interacts with the cells to perform other active functions. As proposed by Brand (Brand 1992), ECM also serves as a filter to cells from external mechanical and mass transport stimuli. Furthermore, ECM adapts itself according to external mechanical stimuli, which is obvious evidence of the structure-property relation. Likewise, tissue engineering scaffolds can play more active roles as temporary substitutes for ECM, being designed by controlling their internal architectures to specific requirements.

Combined with the multiscale homogenization, topology optimization allows designers to find an optimal pore architectural layout for the desired mechanical and mass transport properties of the scaffold itself. Indeed, for the design of hierarchical structures, topology optimization may be a particularly promising technique in the design of microstructure. Because tissue functions are best approximated or measured by the mechanical and mass transport properties, the design of the tissue engineering scaffolds must incorporate optimal pore configuration or material layout at the microscopic scale to match the properties of natural tissues at the macroscopic scale.

The degradation of the scaffolds further complicates the hierarchical design by introducing a dynamic change of the properties of the initial scaffold. Failure to properly model this dynamic could easily undercut the ability of the scaffolds to properly function *in vivo*. In vivo, the scaffold structure is expected to degrade at a predictable rate in line

with the generation of tissue (i.e. bone) destined to take over the necessary functions of the original structure. Furthermore, the transfer of the functions from scaffold to tissue should occur seamlessly during the process of degradation. Hence, the initially designed functional properties of scaffolds may need to remain at a consistent level throughout the tissue regeneration. In fact, in a recent study (Jiya et al. 2009), biodegradable cages used in spinal fusion failed due to premature loss of device integrity, which is in turn was the direct result of the inability to predict and correlate structural degradation in respect to bone regeneration. Without being able to model the dynamic of degradation and necessary functional properties, device integrity in hierarchical scaffold design is relegated to chance.

In response to the issues of degradation, several mathematical models have been proposed to explain the underlying mechanisms of the degradation of biodegradable polymers. Particularly, models based on diffusion-reaction equations under continuum assumptions are often adapted to investigate the spatial differences of the degradation as well as the temporal change. However, prediction of the degradation of scaffolds may need multiscale modeling because the degradation can be altered in the presence of the porous architecture. In fact, the pore architecture affects the degradation of scaffolds as well as the mass transport properties through their pores, which can again affect the diffusion of the degradation products. The multiscale homogenization theory, in this regard,can model the degradation of hierarchical scaffolds, accurately considering the effect of the microstructures.

To tailor the properties of scaffolds as well as to compensate for the loss of functions due to degradation, the study goal was to provide a systemic design framework

for tissue engineering scaffolds based on multiscale homogenization method and topology optimization. First, homogenization of linear elasticity and homogenization of diffusivity were derived to evaluate scaffold mechanical and mass transport properties. Then, microstructural topology optimization in a multiobjective form was applied to obtain various microstructures with different mechanical and mass transport properties. To demonstrate the hierarchical scaffold design in a clinical application, *in situ* porous biodegradable fusion cages were designed, fabricated, and tested. Finally, the degradation behavior of the hierarchical scaffolds was predicted based on multiscale diffusion-reaction equations.

1.2 Integrated Design Framework for Tissue Engineering Scaffolds

In order to provide an integrated design framework for tissue engineering scaffolds, rigorous design method that support the property-structure relations as well as the fabrication methods that reproduce the designed architecture and properties are indispensible. In addition, the knowledge of the design parameters and their target values is of paramount importance. Based on these targets, the computational design framework can produce optimal designs with controlled pore architecture and functional properties. Furthermore, as scaffolds degrade, the controlled architecture and properties can change and must be accounted for in a systemic design approach.

With regard to the designed and target properties, the comparison between tissues and scaffolds is made at tissue or organ scale. As shown in Figure 1.1, natural tissues, say, long bone has several hierarchical levels ranging from the lacunar-canliculi network through trabecular and cortical bone to whole bone level. The pore architecture of

scaffolds mimicks the microstructures by trabecular and cortical bones. Because the functions of the tissues are measured at the whole bone level, the properties of the scaffolds are characterized at the (global) scaffold scale. Thus, the properties of tissues and scaffolds are compared at the global scale while the design is conducted at the microstructural level. A hierarchical scaffold design framework should, therefore, be able to consider the rigorous relation between microstructures and the global level properties and functions of a scaffold.

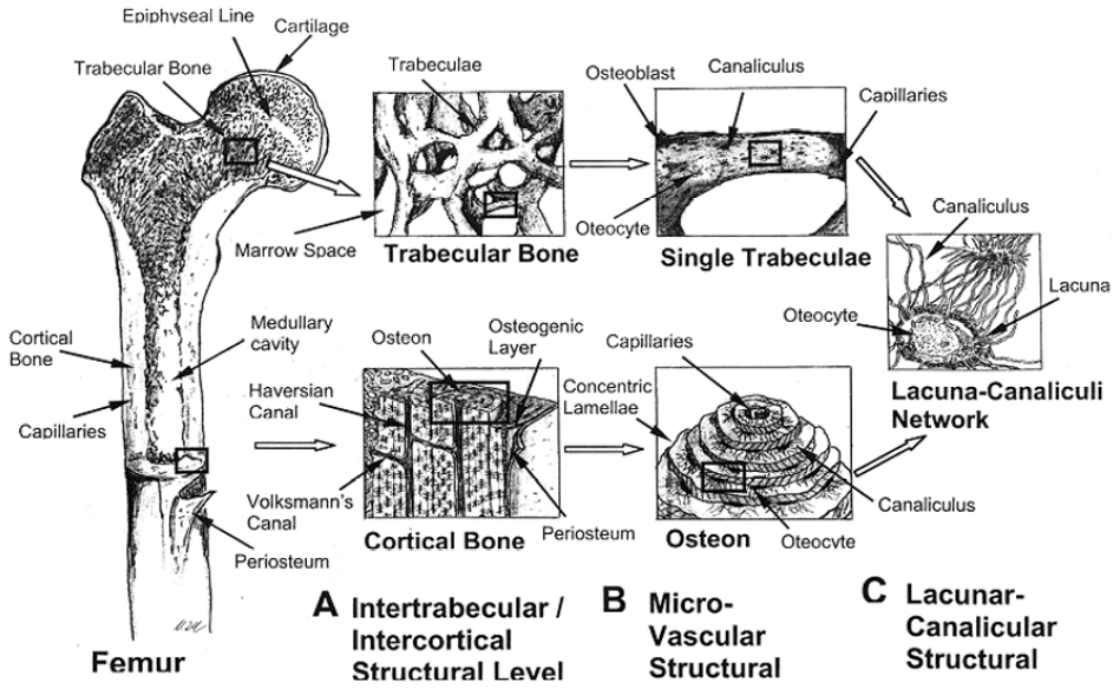

Figure 1.1 Hierarchical structure of long bone from lacunar-canliculi network through trabecular and cortical bones to whole bone level. The properties of tissue engineering scaffolds are compared at the whole bone level (Liebschner and Wettergreen 2003).

1.2.1 The Tissue Engineering Scaffold

The tissue engineering approach for repairing diseased or damaged tissues utilizes biomaterial scaffolds delivering biologics, including cells, genes, and/or proteins. Isolated donor cells are cultured on a scaffold and the cell-scaffold construct is implanted into a tissue defect site (Langer and Vacanti 1993; Kim and Mooney 1998). During in vitro cell culture and after implantation, a scaffold serves several roles in tissue regeneration. The tissue engineering scaffolds should provide anatomical tissue shape to fill in the tissue defect site and preserve three-dimensional space to guide tissue formation, provide temporary functional support under physiological conditions, and enhance cell functions and tissue regeneration via mass transport of nutrients, wastes and other biologics (Hollister 2005). These scaffold roles are influenced by its internal architectures including porosity, pore size, and interconnectivity, which also determine the effective properties. Thus, the goal of scaffold design should be to find a pore geometry, or microstructure that best achieves a desirable functional environment for a regenerated tissue.

However, the appropriate or optimal design parameters a scaffold should provide are generally tissue specific and often conflict with each other. Furthermore, there is little consensus among researches as to the optimal properties of scaffolds. Regarding pore morphological parameters, pore size and void volume were demonstrated to affect the bone healing with spatial variation (Aronin et al. 2009). Pore sizes between 100 and 400 μm were proposed for better osteoconduction (Cyster et al. 2005), while no significant differences in the bone formation was found for scaffolds with pore size greater than 300 μm (Roosa et al. 2010). Kuboki et al. found that a pore size of 300–400 μm was optimal

for bone formation (Kuboki et al. 1998). Porosity, or void volume fraction, has been considered as one of scaffold design parameters.

With regard to the scaffold effective properties, it is hypothesized that scaffold elastic or aggregate modulus should match that of healthy tissues at the defect (Hutmacher 2001), which spans 10 ~ 1500 MPa (elastic modulus) for trabecular bone (Goulet et al. 1994) and 0.5~3.0 MPa (aggregate modulus) for articular cartilage (Boschetti et al. 2004; Demarteau et al. 2006). While satisfying these mechanical requirements, the bone tissue engineering scaffolds should be designed with high diffusivity, permeability or porosity for better cell migration and biologics transport. On the other hand, scaffolds for cartilage regeneration are often designed with limited transport property due to the avascular and low metabolic nature of cartilage (Malda et al. 2003). Kemppainen and Hollister demonstrated that low permeability environment is favorable for cartilage regeneration, whereas high permeability was correlated to more matrix production (Kemppainen and Hollister 2010).

In the aforementioned scaffold roles, "temporary support" implies that the scaffold should eventually disappear and transfer the functional role to regenerate tissues (Figure 1.2). The degradability of the scaffold introduces more complexity into the scaffold design, since the initially designed properties are altered during *in vitro* cell preparation and *in vivo* implantation. The scaffolds must retain the mechanical integrity up to a certain juncture in tissue remodeling, typically 6 month for bone regeneration (Hutmacher 2000). However, since the timeline for degradation starts during in vivo cell culture, the design target should be adjusted to reflect the pre-implantation and implantation degradation.

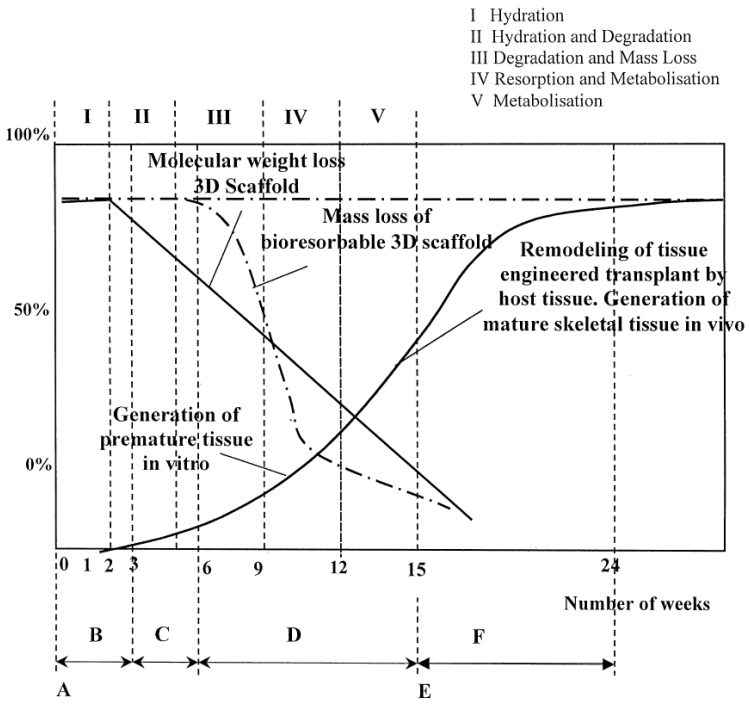

Figure 1.2 Schematic diagram of the complex interplay between degradation of the scaffold and tissue regeneration. From initial scaffold fabrication through cell/tissue culture in vitro and in vivo remodeling of the tissue, the scaffold-tissue construct is expected to maintain the desired functional properties. (Hutmacher 2000)

The proposed integrated scaffold design framework in this study is based on the computational homogenization theory combined with topology optimization in order to tailor scaffold internal architectures, thus providing an “optimal” environment for cells and regenerate tissues. Based on the broad ranges and time dependency of design requirements, a design technique should be able to rigorously control the pore architecture and its properties. Furthermore, the design technique should be able to address the time dependent changes of the morphological and mechanical characteristics

of the scaffolds. In order to design the best scaffold for a particular reconstruction application, we must be able engineer scaffolds by combining hierarchical design and computational simulation with biomaterial fabrication to achieved desired properties. The systemic design of scaffolds using homogenization method and topology optimization will allow us to experimentally test the engineered scaffolds in *in vitro* cell models to large *in vivo* functional animal models to determine relevant and critical scaffold characteristics.

1.2.2 The Homogenization Theory

Theoretical background supporting the hierarchical scaffold design is the asymptotic homogenization method. The homogenization method enables us to estimate the effective properties of composite or porous scaffolds with periodic microstructures as well as model porous media as continuum with homogenized properties. The homogenization method, which was developed and extensively investigated by French mathematicians, was first studied to solve fluid flow problem in porous media. The method have since been applied to linear and nonlinear mechanics problems in mechanics, head transfer problems, vibration, electromagnetism, and wave propagation in porous media (Bensoussan et al. 1978; Sanchez-Palencia et al. 1987; Auriault et al. 2009).

Major assumption of the mathematical formulation is the separation of the scale. For a composite with large numbers of microstructures, the physical processes become difficult and often impossible because of the large heterogeneities. If the scale of the microstructure is sufficiently small, an averaged behavior or properties of the system can be described by phenomenological or experimental investigation. The homogenization

method here provides a method to investigate the local structural effect to the macroscopic description, with assumptions of separation of scale and periodicity of microstructures. That is, the homogenization process converts a problem in a composite into local problem in unit microstructure and an equivalent macroscopic problem (Figure 1.3).

With periodic boundary condition, the macroscopic flux driven microscopic quantity distribution within the local domain is averaged to give the effective properties of the equivalent continuum. The final solution including the local structural contribution can be obtained through the localization process by summing the solutions for different scales. If the small parameter for the separation of scale approaches zero, the description at the equivalent continuum serves as the final solution.

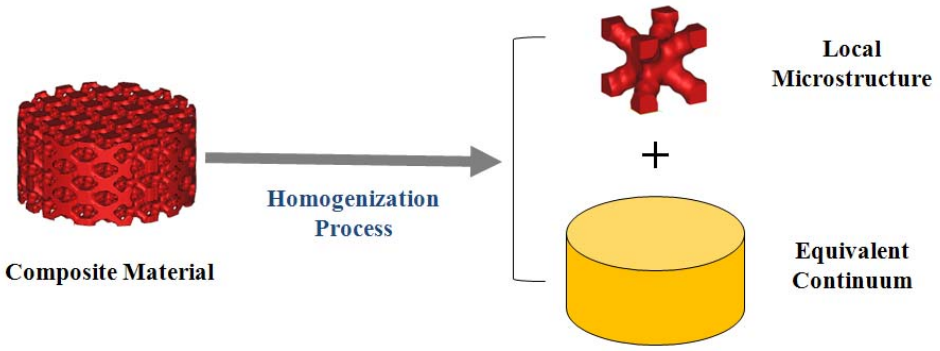

Figure 1.3 Homogenization process finds a macroscopic equivalent (averaged) description from the analysis of the local microstructure.

The effective properties of composite materials have theoretical bounds for given material volume fractions, or porosity. Hashin and Shtrikman derived variational bounds on the effective magnetic permeability (Hashin and Shtrikman 1962), the effective bulk modulus and shear modulus (Hashin and Shtrikman 1963). Those bounds were improved by coupling bulk modulus and shear modulus, using the translation method (Cherkaev and Gibiansky 1993). Various bounds including fluid permeability and electrical conductivity are derived in (Torquato 2002).

However, when multiple properties are considered simultaneously, there are cross-property bounds that link the properties through the microstructure. Gibiansky and Torquato derived cross-property bounds between conductivity and elastic modulus were derived (Gibiansky and Torquato 1993; Gibiansky and Torquato 1995; Gibiansky and Torquato 1996). Rigorous link between permeability and electrical conductivity was derived in (Avellaneda and Torquato 1991). As noted by the authors of these studies, the bounds of electrical conductivity can be effective to thermal conductivity, diffusion, dielectric constant and magnetic permeability due to mathematical equivalency.

In cross-property bounds with competing properties, or ill-ordered material phases, the tradeoff between properties is readily apparent. For example of cross-property bounds between bulk modulus and diffusivity, achieving the higher bulk modulus can only be achieved with reduced diffusivity while the higher diffusivity can only be achieved at reduced bulk modulus. This cross-property bound can be utilized in defining design targets when multiple properties are involved simultaneously.

Mimicking the hierarchical nature of biological tissues, scaffolds can be designed by repeating representative unit structures, called unit cells, in 3-dimensional space. The

theoretical characterization of the porous scaffold can be obtained by the homogenization analysis of the unit cell, assuming sufficiently small unit cell dimension relative to the entire porous scaffold. Scaffold dimensions in our study vary from 5 mm to 25 mm while the size of unit microstructures ranges 1 mm to 2.7 mm, which typically yields the small scale parameter of 0.2. Note that the smallest possible unit cell size is limited by the fabrication resolution in the hierarchical scaffold design. In comparison of the homogenization method with standard mechanics in this case, Hollister and Kikuchi demonstrated that homogenization method predicted local strain energy density within 30% of deviation from direct analysis of composite, compared to 70% error with standard mechanics approach (Hollister and Kikuchi 1992). Furthermore, error correction with higher order terms in the asymptotic expansion can be considered as suggested by Auriault et al. (Auriault et al. 2005).

1.2.3 Topology Optimization

Topology optimization distributes limited material volume within a predefined design domain such that the final structural architecture satisfies the optimization objective and constraints. There are three categories in the structural optimization: size optimization, shape optimization, and topology optimization (Figure 1.4). Size optimization problems seek an optimal thickness distribution of predefined structural members. By changing the dimensions of each structural member, it finds a structure with main contribution. Shape optimization changes the boundary of structures without altering the structural interconnectivity, or topology. That is, the number of holes remains constant during optimization. It should be noted that these methods depend on the *a*

priori knowledge of the structural configuration. On the other hand, the topology optimization seeks optimal structural topology when the structure is not known. Typically, the design domain is composed of regular finite elements, each of which is assigned a design variable. The design variables represent the structural topology. The optimization algorithm adjusts the design variables to determine the optimal structural topology.

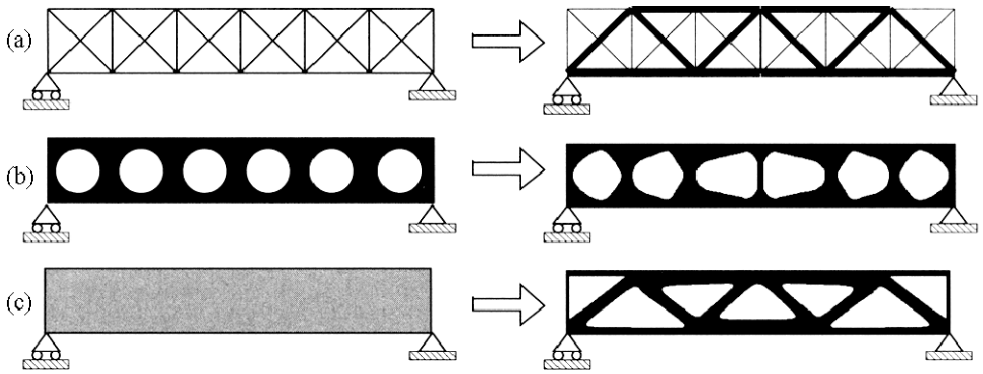

Figure 1.4 Illustration of (a) size optimization, (b) shape optimization, and (c) topology optimization. (figure from (Guest 2005))

Topology optimization has gained popularity after the pioneering work by Bendsøe and Kikuchi (Bendsoe and Kikuchi 1988). Introduction of continuous variables based on the homogenization of materials with solids and voids expanded the practical engineering applications of the topology optimization. The problem, which was redefined as the distribution of micro-holes in the design domain, could now determine the final structural topology. Bendsøe (1989) later proposed a simpler alternative, artificial material law, to homogenized materials (Bendsøe 1989). Although it is not physically based, the artificial material law gained popularity because of its simplicity.

The above methods of the artificial material law have been successfully adopted into structural optimization in the problems of mechanics, such as minimum compliance design, compliant mechanism design (Sigmund 2001), structural vibration problems (Diaz and Kikuchi 1992), heat conduction (Gersborg-Hansen et al. 2006), fluid flow problems (Gersborg-Hansen et al. 2005; Guest and Prevost 2006), crashworthiness of vehicles (Pedersen 2004) and the design of material microstructures (Sigmund 1994; Sigmund 1994; Sigmund 1995).

Among these applications, material microstructure design problems, so called inverse homogenization, have been extensively studied since Sigmund demonstrated the design of microstructures with prescribed properties (Sigmund 1994). Recently, two effective properties were concurrently optimized in the design objective or constraints. Heat conductivity and electric conductivity were optimized in an ill-ordered composite to be matched with Schwarz primitive minimal surface (Torquato et al. 2003). Effective permeability and bulk modulus were simultaneously maximized in the multiobjective formulation and demonstrated the variations of the optimal microstructures by the choice of weight values (Guest and Prevost 2006). Bulk modulus and thermal conductivity were maximized by minimizing both mechanical and thermal compliances in 2D (de Kruijf et al. 2007). The authors explored Pareto optimality by varying weights for mechanical and transport properties. Isotropic microstructures with maximized bulk modulus and conductivity were designed (Challis et al. 2008). The authors also explored design changes with the different combinations of weighting factors.

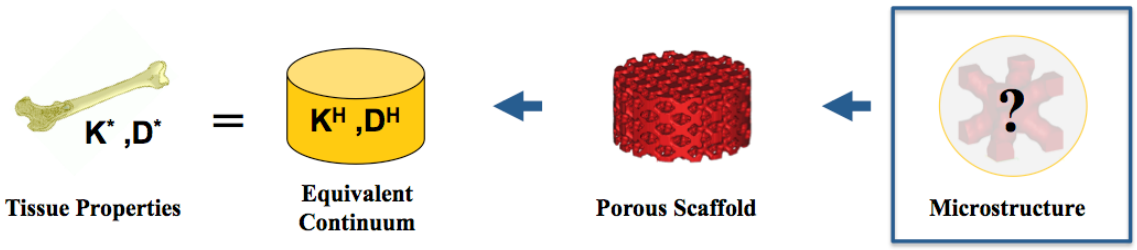

Figure 1.5 Microstructures are designed to match the bulk modulus (K^H) and diffusivity (D^H) of a porous scaffold with those of normal healthy tissue (K^* and D^*, respectively).

It is well known that topology optimization in its relaxed form suffers from numerical instabilities such as checkerboard patterns and mesh dependent solutions (Sigmund and Petersson 1998). To avoid these instabilities, filtering techniques were introduced following the idea of digital image processing (Sigmund 1994). The filtering technique is most popular and generally adapted in the topology optimization. Highly oscillating element density values are smoothed by averaging element densities over a range of neighborhood elements or by averaging the design sensitivity derivatives. In addition, filtering techniques have been utilized to control minimum structural member size by assigning the radius value. The density filtering, however, interferes with design density evolution by design sensitivity, producing non-converged density distribution. The sensitivity filtering, applied to the design sensitivity derivative, can produce converged solutions.

In this study, we adapted the inverse homogenization method with multiple property consideration. Effective diffusivity and bulk modulus were simultaneously optimized to achieve prescribed target properties. The error between the effective

properties and target properties were minimized in the objective function. The numerical instability was controlled with a nonlinear sensitivity filtering technique.

1.2.4 Solid Freeform Fabrication

The fabrication of custom designed scaffold architectures becomes feasible with the aid of solid freeform fabrication (SFF) technique. With its accuracy and reproducibility, SFF has become popular for manufacturing of tissue engineering scaffolds. Compared to conventional methods such as solvent casting and particulate leaching (Mikos et al. 1994), gas foaming (Mooney et al. 1996), and freeze drying (Whang et al. 1995), SFF provides more flexibility to fabricate 3D shapes for anatomic defects as well as more accuracy to reproduce intricate pore architecture. The conventional methods can also control scaffold functional properties by changing porogen size, temperature or pressure, yet limited within certain ranges (Taboas et al. 2003). However, the conventional methods are difficult when producing shapes with precise anatomy to fit in a tissue defect site. The particular strength of SFF is for fabrication of scaffolds designed for high load bearing applications such as orthopedic fixation devices and fusion cages.

Several types of SFF techniques are available for tissue engineering scaffolds. Hutchmer et al. demonstrated the fabrication of PCL scaffolds by Fused deposition modeling (FDM). Williams et al. fabricated poly(ε-caprolactone) (PCL) scaffolds using selective laser sintering technique (Williams et al. 2005). Shor et al. used precision extruding deposition (PED) to manufacture scaffolds with PCL and hydroxyapatite (HA) mixture (Shor et al. 2008). Among these, a selective laser sintering SFF technique was used in this study for fabrication of optimal scaffolds and biodegradable fusion cages

using PCL and HA. These scaffold samples were used for mechanical tests to validate the theoretically designed properties.

1.3 Biodegradable Fusion Cages

1.3.1 Spinal Fusion Cages

Spinal fusion is a surgical intervention for patients with disc degenerative condition. When conventional non-surgical treatments fail, two or more vertebral bodies are fused to remove segmental instability, which can cause nerve root irritation and low back pain. In 2001, 357,000 patients underwent lumbar spinal surgery in the US alone, of which over 122,000 were lumbar spinal fusions for degenerative disc conditions (Deyo et al. 2005). It was 220% increase from 1990 and the increase was accelerated after FDA approval of intervertebral cages in 1996.

Spinal fusion can be categorized to posterolateral fusion and interbody fusion. Posterolateral fusion combines posterior elements by placing bone graft between transverse processes with pedicle screws, while intervertebral disc space remains intact. Interbody fusion unites anterior vertebral bodies by placing bone grafts at the intervertebral disc space. The use of interbody fusion cages as an adjunct for bone graft was attributed to the high rate of failure associated with use of bone graft alone or use of posterior pedicle screws and rods (McAfee 1999). With superior rigidity, the interbody fusion cages can bring immediate stability and enhance fusion rate by removing relative motion at the treated site. Furthermore, the amount of grafting bone can be reduced with the introduction of the fusion cages.

Bagby first introduced a perforated stainless steel basket for treating horses with Wobbler Syndrome and eliminated the need for autograft harvesting by packing cancellous bone chips from the reaming procedure of the vertebral endplates (Bagby 1988). Then, Kuslish and Bagby made modifications of the strainless steel basket and developed the Bagby and Kuslish (BAK) cage (Kuslich et al. 1998). This cylindrical titanium cage has threads for increased stability of the device and fusion rate with a stand-alone anterior device. Ray also developed a titanium interbody fusion cage with deep threads for posterior lumbar interbody fusions (PLIF) (Ray 1997).

There are several different types of lumbar fusion cages according to the cage placement approach: Posterior lumbar interbody fusion (PLIF), Anterior lumbar interbody fusion (ALIF), and Transforminal lumbar interbody fusion. With PLIF, the spine is approached from posterior along with laminectomy for better visualization of the nerve roots. Then, the nerve roots are retracted to one side and the intervebral discs are removed. An interbody cage with bone graft is then inserted into the disc space, through which, new bone grows from a vertebral body to the next one. PLIF has advantage of leaving less scar tissue due to minimal incision of muscles. However, posterior approach has potential risks of nerve root injury. In addition, the removal of anterior disc material may not be sufficient compared to anterior approach, which leaves less space to bone graft or fusion cages.

ALIF, on the other hand, approaches the spine through the abdomen. The ALIF can avoid nerve injury and incision of back muscles. It also allows better access to the intervertebral disc space and complete removal of disc material. However, the removal of

anterior longitudinal ligaments is not favorable for maintaining segmental stability. In addition, anterior approach may damage the large blood vessels and result in hemorrhage.

TLIF is a minimal invasive procedure where the spine is approached through a foramen from posterior. Unlike PLIF, the TLIF removes only one facet joint to decompress the disc space and fusion cage is placed from one side. A portion of annulus fibrosus is dissected, nucleus pulposus removed, and single fusion cage or bone graft is inserted. Further stabilization is augmented by posterior fixation such as pedicle screws and rods.

1.3.2 Biodegradable Cages

Early clinical reports on using these cages, which were mostly made of metals, are generally positive. However, these metallic cages were often associated with several complications, including device related osteopenia, subsidence, and migration (Smith et al. 1991; Aoki et al. 2009). The excessive rigidity of the device might cause the absorption of adjacent bones by stress shielding effects, loosening the device fixation to host bone. In addition, these metallic cages often fail to effectively transfer loads to stimulate bony tissue remodeling (Kanayama et al. 2000; van Dijk et al. 2002). These can cause retarded fusion, which may be ended up with pseudarthrosis (nonunion) and cage migration (Chen et al. 2005). Radiopacity of metallic cages also interfere with visualization of bony fusion at the treated site during postoperative follow up evaluation (Cizek and Boyd 2000; Robertson et al. 2009), making it difficult to determine the progress of bony healing. Finally, the permanent material may cause long-term foreign body reaction. In some cases, wear debris or corrosion of material causes inflammation of surrounding soft tissues (Brantigan and Steffee 1993).

The shortcomings and complications of non-degradable metallic and polymeric cages made researchers to explore the utility of biodegradable material in the high load bearing fusion devices. The apparent advantage of biodegradable cages is that the material will disappear after complete bony fusion. This can avoid possible foreign body reaction as well as secondary removal surgery. The radiolucency of the biodegradable material confers better visualization and evaluation after surgery. With reduced cage stiffness to adjacent bone level, the biodegradable cages are less likely related to stress shielding effects and more transfer load to the ingrown bone. Van Dijk and colleagues have investigated the utility of poly L lactic acid (PLLA) cages in a large animal goat model. They demonstrated that reduced cage stiffness enhanced bony fusion (van Dijk et al. 2002). The feasibility for lumbar interbody fusion and biocompatibility of the PLLA cages were also demonstrated in four years of in vivo animal study (van Dijk et al. 2005).

Despite these advantages, however, the biodegradable cages may suffer from weaker mechanical properties. Further deterioration of the structural integrity due to degradation after implantation may lead to failure of fusion. The time dependent mechanical property changes were correlated with loading conditions, temperature and humidity (Smit et al. 2008). They also found that the biodegradable cages might undergo premature device failure in an *in vivo* condition (Jiya et al. 2009). It should be noted that these studies used conventional designs (Weiner and Fraser 1998), including hollowed cylinders with threads, open boxes, and vertical rings, for biodegradable cages. Also note that mere replacement of permanent materials with biodegradable polymers in conventional designs like hollow cylinders or open boxes may not provide sufficient strength for lumbar fusion.

1.3.3 Design of Porous Biodegradable Fusion Cages Using the Integrated Global-Local Topology Optimization

The integrated global and local topology optimization, in this respect, may overcome the complications related to the intrinsic weakness of the material. The global topology optimization is for optimal material density layout, whereas the local topology optimization is for the design of microstructures with maximized permeability and stiffness. The global density layout serves as a map for particular microstructures to be used. The porosity of microstructures is determined according to the global density, or porosity. The local microstructural topology optimization can then provide maximized permeability and maximized elasticity for given porosity. Globally optimized structure will provide maximum structural support while locally optimized microstructures provide maximal permeability for bony ingrowth and metabolic transport.

This multiscale optimization approach is such flexible as to be applied with various property microstructures and base biomaterial. Thus, the method can be readily applied to customize the fusion cage for preclinical large animal models as well as human clinical studies. The porous biodegradable fusion cages may enhance bony fusion with well-controlled interconnected pore architecture.

1.4 Hydrolytic Degradation of Biodegradable Polymers

Biodegradable polymers, particularly aliphatic polyesters such as poly glycolic acid (PGA), poly lactic acid (PLA), and poly(ε-caprolactone) (PCL), are mostly investigated

and utilized for biomedical and tissue engineering applications. These polymers have been used for degradable sutures, orthopaedic implants, drug delivery system, and tissue engineering scaffolds (Ueda and Tabata 2003; Vaccaro et al. 2003).

One of the degradation mechanisms of aliphatic polyesters is hydrolysis. Water molecules penetrate into the amorphous region in bulk polymer and attack the polymer backbone to be cleaved into smaller polymer chains with acid and alcohol end groups, since these polyesters have a carboxylic acid end group at one end and a hydroxyl group at the other end (Figure 1.6). The produced carboxylic acids are known to involve in the hydrolysis as catalysis, accelerating the hydrolysis by acid-catalysis. The produced acids, especially for PLA, can easily dissociate, resulting in an acidic environment, which lowers local pH environment and accelerates the hydrolysis reaction speed. Particularly in clinical applications, the acidic environments formed within biodegradable implants by hydrolysis may also cause inflammation of surrounding tissues. Biodegradation *in vivo* also involves enzymatic degradation, producing lactic acids, water and carbon dioxide.

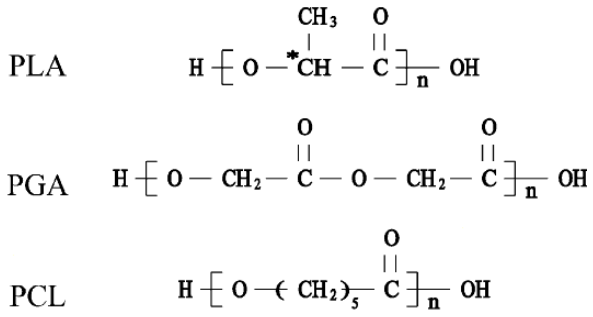

Figure 1.6 Structural formula of PLA, PGA, and PCL (Ueda and Tabata 2003)

There are two different degradation or erosion mechanisms: surface erosion and bulk erosion. In a surface eroded polymer, mass loss during degradation occurs at the polymer surface, changing the shape of the structure. In bulk eroded polymer, degradation rates over the polymer are uniform, and degradation and mass loss occur homogeneously throughout the polymer. In general, these two different mechanisms can be described with relative difference in the diffusion of water and hydrolysis rate. Von Burkesroda et al. presented a comprehensive model of these two different erosion behaviors (von Burkersroda et al. 2002). In their model, the relative speed of water diffusion and the hydrolysis reaction was introduced in a non-dimensional parameter. From this parameter, a measure for critical length can be derived. If the size of a bulk eroded specimen is greater than the critical length, the specimen undergoes surface erosion. It should be noted that, in many cases, the aliphatic polyesters undergoes bulk erosion, indicating that water diffusion into the polymer is much faster than hydrolysis reaction.

In bulk erosion, one of complex behaviors is heterogeneous degradation: the inner region degrades faster than outer periphery. The production of the hydrolysis is carboxylic acid, which again acts as a catalyst for the reaction and accelerates the reaction rate by acid autocatalysis. The product small chains with a carboxylic acid end group become water soluble and freely diffuse within the polymer matrix. The release of the small chains out of bulk polymer accounts for the mass loss during degradation. The diffusion of the acids at the periphery quickly occurs, whereas the acid end group inside takes longer time and accelerates the hydrolysis inner region before escape. Finally, the center of the polymer specimens is hollowed, the periphery remaining as a wall (Vert et

al. 1994). In addition, fast degradation is often observed in thick polymer specimens as opposed to thin polymer specimens, which has been explained by a the similar mechanism: the interplay between the acid end group diffusion and hydrolysis reaction (Grizzi et al. 1995). The acidic product with the water soluble small chains take more time to escape the thick polymer block, which allows more time to accelerate hydrolysis within the polymer matrix.

In order to determine the underlying mechanisms of polymer degradation, several computational and mathematical models have been proposed. Examples include empirical models based on hydrolysis kinetics, Monte Carlo simulation based models, models for chain cleavage, and a diffusion-reaction based model. Among these, the diffusion-reaction model has advantage over others in that it predicts spatial and temporal differences of polymer degradation based on autocatalytic hydrolysis. For the design of degrading hierarchical scaffolds, it is important to know the effect of pore architecture, i.e. the spatial distribution of material on degradation, i.e. temporal behavior. Moreover, the diffusion reaction model can be readily extended to multiscale model using the homogenization method, providing rigorous relation between pore architecture and degradation of the hierarchical scaffolds.

Multiscale modeling of the degradation of porous scaffolds may provide insights into the affects of pore architecture design on both initial mechanical properties and the *in vivo* change in properties due to degradation. We postulated that a hierarchical scaffold design approach based on topology optimization and multiscale homogenization would produce a biodegradable scaffold strong enough to support physiological loads before

implantation, but that with the introduction of the multiscale degradation model could assure the integrity of the design *in vivo*.

1.5 Outline of Thesis

The goal of this study is to provide a computational framework for the design of hierarchical scaffolds with tailored mechanical and mass transport properties. In order to address the degraded material properties after implantation, a diffusion-reaction based model was adapted to characterize the degradation of the scaffold. To this end, we derived the homogenization of mechanical and mass transport phenomenon in a porous scaffold in chapter 2. For the mechanical property characterization, linear elasticity was considered. The effective elasticity tensor is directly obtained from the homogenization of linear elasticity. For mass transport measures, diffusion and fluid permeability were considered. Then, homogenization of diffusion-reaction equations were derived for multiscale analysis of hydrolysis. The effective diffusivity and linear elasticity were utilized in the microstructural topology optimization in chapter 3. Assuming isotropic material design, the bulk modulus and diffusivity were optimized using homogenization based topology optimization. The theoretically designed properties were compared with mechanical compression test results. As a clinical application of the hierarchical scaffold, biodegradable fusion cages were designed using a global-local integrated topology optimization technique in chapter 4. Applying biodegradable material in a high load bearing site is one major challenge. The global topology optimization addresses the strength issues while the local topology optimization provides sufficient mass transport within the cage. Finally, a diffusion-reaction based model was adapted to characterize

degradation of porous scaffolds in chapter 5. Homogenization of the diffusion-reaction equation was applied to describe the diffusion and reaction of the produced acid end groups.

CHAPTER 2

HOMOGENIZATION OF SCAFFOLD MECHANICAL AND MASS TRANSPORT PROPERTIES

2.1 Overview

The asymptotic homogenization method is the theoretical basis for the hierarchical scaffold design scheme (Hollister 2005), where tissue engineering scaffolds are considered as composite or porous media with repeated unit microstructures. A porous medium, or a porous structure, is defined as a mixture of solid material with pores inside. The pore can be either empty or fluid saturated in this study. The characterization of such scaffolds is conducted by experiments on the fabricated specimen, which is always required before *in vitro* and *in vivo* studies. However, experimental measurements are in many cases limited so as to be correlated in an averaged sense without knowing detailed phenomena in the pores. On the other hand, numerical evaluation of the properties of scaffolds is challenging because of the complexity of pore geometry, which demands high computational costs. Multiscale modeling and analysis techniques such as the homogenization method are of great importance with rigorous connection between detailed microstructures and macroscopic properties..

The homogenization method is a well-established mathematical modeling technique when there is a separation of the length scales between the macrostructure and microstructure. Assuming the hierarchically designed scaffolds possess good separation between scaffold scale and microstructure scale, the homogenization method can be utilized to characterize mechanical function of the scaffold as well as mass transport properties through the pores.

In this chapter, we will derive the homogenization of elasticity, homogenization of diffusion, homogenization of reaction-diffusion, and homogenization of Stokes flow, to numerically characterize the scaffold properties as well as design microstructures with prescribed properties. The homogenized diffusivity and elasticity, along with multiobjective topology optimization, were utilized in the design of microstructures with tailored material properties in chapter 3. In tissue engineering, the permeability is mostly adopted as a mass transport property measure of biological tissues as well as scaffolds, owing to its relatively simple experimental setting. The homogenization of Stokes flow in porous media is known to produce Darcy's law in the macroscopic scale. From the homogenization of Stokes flow, the effective permeabilities of the scaffolds were evaluated. Last, the homogenization of reaction-diffusion was derived for the computational simulation of polymeric scaffold degradation in chapter 5. The acid-catalyzed hydrolysis reaction in solid matrix produces water soluble acidic monomers, which can diffuse through the porous scaffold, both solid and pores. With the aid of rigorous theoretical basis, the effects of pore architecture on the degradation of porous scaffolds can be further elucidated.

2.2 Preliminary

The homogenization process finds an equivalent macroscopic boundary value problem from differential equations with highly oscillating coefficients. The homogenization method can be also used to determine the effective macroscopic properties from an analysis of a representative microstructure of a porous media or composite material assuming periodicity (Bensoussan et al. 1978; Sanchez-Palencia et al. 1987). The analysis responses at a local level with periodic boundary conditions are averaged to give the effective properties at a global scale. While the macroscopic variable represents the scaffold level scale, the microscopic variable describes the pore domain, or unit microstructure. In general, the local microstructure domain is defined in a rectangular cuboid, Y, for 3D problems.

$$\mathrm{Y} =]0, \mathrm{Y}_1[\times]0, \mathrm{Y}_2[\times]0, \mathrm{Y}_3[\tag{2.1}$$

The periodicity means any quantity has the following relations

$$F(\mathbf{y} + \mathbf{NY}) = F(\mathbf{y}) \tag{2.2}$$

where N is a diagonal matrix, whose components $\mathrm{N_{ii}}$ are arbitrary integers. The pore geometry is also periodic.

A major assumption is the separation of the scales between the global and local structures. Based on this assumption, a small variable, ε, for the ratio between microscopic length scale and macroscopic length scale can be defined as

$$\varepsilon = \frac{x_i}{y_i} << 1 \tag{2.3}$$

where x_i is a the length or the macroscopic scale and y_i is the number of microscopic lengths that occur in one microscopic length, x_i.

The hierarchical gradient can be defined with respect to the macroscopic length scale by the chain rule.

$$\frac{\partial}{\partial x_i} \to \frac{\partial}{\partial x_i} + \frac{1}{\varepsilon}\frac{\partial}{\partial y_i} \tag{2.4}$$

Substitution of the expanded field variables and the hierarchical derivatives into the governing equilibrium equations leads to macroscopic and microscopic equilibrium equations. The microscopic equation can be solved by applying unit gradients of the macroscopic variables under the assumption of the periodicity of the microstructure and properties. The analysis is to investigate the asymptotic behavior of the system as ε approaches zero.

2.3 Homogenization of Linear Elasticity

Linear elastic problem is to find $u_i \in U = \{u_i \,|\, u_i = g_i \text{ on } \partial\Omega_u\}$ such that with

$$\begin{aligned} \frac{\partial \sigma_{ij}^{\varepsilon}}{\partial x_j} + f_i &= 0 \quad \text{in } \Omega \\ \sigma_{ij}^{\varepsilon} n_j &= t_i \quad \text{on } \partial\Omega_T \\ \sigma_{ij}^{\varepsilon} &= C_{ijkl} e_{kl}^{\varepsilon} \\ e_{kl}^{\varepsilon} &= \frac{1}{2}\left(\frac{\partial u_k^{\varepsilon}}{\partial x_l} + \frac{\partial u_l^{\varepsilon}}{\partial x_k} \right) \end{aligned} \tag{2.5}$$

where $\sigma_{ij}^{\varepsilon}$ is a stress tensor, f_i is body force, t_i is traction on traction boundary $\partial\Omega_T$, n_j is outward normal, e_{kl}^{ε} is the small strain tensor, C_{ijkl} is the linear elasticity tensor, u_k^{ε} is the displacement, and the superscript ε indicates the dependence on the microstructure.

With the asymptotic expansion of the displacement, u_i,

$$u_i^{\varepsilon} = u_i^{(0)}(x,y) + \varepsilon u_i^{(1)}(x,y) + \varepsilon^2 u_i^{(2)}(x,y) + \ldots \tag{2.6}$$

and hierarchical derivative,

$$\frac{\partial}{\partial x_i} \rightarrow \frac{\partial}{\partial x_i} + \frac{1}{\varepsilon}\frac{\partial}{\partial y_i} \tag{2.7}$$

the equation (2.5) becomes

$$\begin{aligned} \varepsilon^{-2}\left(A_1 u_i^{(0)}(x,y)\right) + \varepsilon^{-1}\left(A_2 u_i^{(0)} + A_1 u_i^{(1)}\right) \\ + \varepsilon^{0}\left(A_3 u_i^{(0)} + A_2 u_i^{(1)} + A_1 u_i^{(2)} + f_i\right) + \ldots = 0 \end{aligned} \tag{2.8}$$

where

$$\begin{aligned} A_1 &= \frac{\partial}{\partial y_i} C_{ijkl} \frac{\partial}{\partial y_l} \\ A_2 &= \frac{\partial}{\partial y_i} C_{ijkl} \frac{\partial}{\partial x_l} + \frac{\partial}{\partial x_i} C_{ijkl} \frac{\partial}{\partial y_l} \\ A_3 &= \frac{\partial}{\partial x_i} C_{ijkl} \frac{\partial}{\partial x_l} \end{aligned} \tag{2.9}$$

It is remarked that $A_1\phi = F$ in the microscopic domain, where ϕ is Y-periodic, admits unique solution up to an additive constant, if and only if $\int_Y F(y)dy = 0$ (Bensoussan et al. 1978).

From the leading order, ε^{-2}

$$\frac{\partial}{\partial y_i} C_{ijkl} \frac{\partial}{\partial y_l} u_k^{(0)}(x,y) = 0 \tag{2.10}$$

we notice that the only Y-periodic solution is $u_k^{(0)}(x,y) = u_k^{(0)}(x)$.

From the ε^{-1}, the microstructural governing equation is derived.

$$\frac{\partial}{\partial y_j} C_{ijkl} \frac{\partial}{\partial y_l} u_k^{(1)} = -\frac{\partial}{\partial y_j} C_{ijkl} \frac{\partial}{\partial x_l} u_k^{(0)} \tag{2.11}$$

Notice that the separation of variables in the right hand side of (2.11), the solution form of $u_i^{(1)}$ is

$$u_i^{(1)} = -\chi_i^{kl}(y) \frac{\partial u_k^{(0)}}{\partial x_l} + \overline{\chi}(x) \tag{2.12}$$

Substitution of (2.12) into (2.11) results in the microscopic equilibrium governing equation,

$$\frac{\partial}{\partial y_j} C_{ijkl} \frac{\partial}{\partial y_l} \chi_k^{pq} = \frac{\partial}{\partial y_j} C_{ijpq} \tag{2.13}$$

where C_{ijkl} is the localized elasticity and χ_k^{pq} is the characteristic displacement resulting from the unit strain in *pq*-direction (*pq*=11, 22, 33, 12, 23, and 31).

From ε^0, the condition of $u_i^{(2)}$ having Y-periodic solution is

$$\int_Y \left(A_3 u_i^{(0)} + A_2 u_i^{(1)} + f_i \right) dY = 0 \tag{2.14}$$

Substitution of (2.9) and (2.12) into (2.14) yields the following macroscopic equilibrium equation.

$$\frac{\partial}{\partial x_i} \left(\frac{1}{|Y|} \int_\Omega (C_{ijkl} - C_{ijpq} \frac{\partial \chi_p^{kl}}{\partial y_q}) dY \right) \frac{\partial u_k^{(0)}}{\partial x_l} + f_i = 0 \tag{2.15}$$

The homogenized elasticity properties are calculated as:

$$C_{ijkl}^{H} = \frac{1}{|Y|}\int_{\Omega}(C_{ijkl} - C_{ijpq}\frac{\partial \chi_{p}^{kl}}{\partial y_{q}})dY \tag{2.16}$$

where C_{ijkl}^{H} is the homogenized elasticity tensor, and C_{ijkl} is the localized elasticity.

2.4 Homogenization of Diffusion

Knowing the effective diffusivity is important for understanding diffusive transport in biological tissues. The governing equation of diffusion is

$$\frac{\partial u}{\partial t} = f + \frac{\partial}{\partial x_i}\left(D_{ij}\frac{\partial u}{\partial x_j}\right) \tag{2.17}$$

where u can be the concentration of chemical species or molecules, D_{ij} is the diffusivity tensor, and f is source term.

Assuming scale separation, the concentration of a solute can be expanded with the scale ratio, $\varepsilon = x_i / y_i << 1$.

$$u^{\varepsilon} = u_0(x,y) + \varepsilon \cdot u_1(x,y) + \varepsilon^2 \cdot u_2(x,y) + \cdots \tag{2.18}$$

and hierarchical derivative can then be expressed using the chain rule

$$\frac{\partial}{\partial x_i} \to \frac{\partial}{\partial x_i} + \frac{1}{\varepsilon}\frac{\partial}{\partial y_i} \tag{2.19}$$

By substituting (2.3) and (2.4) into the governing equation (2.2), the governing equation becomes

$$0 = \varepsilon^{-2}(A_1 u_0) + \varepsilon^{-1}(A_1 u_1 + A_2 u_0) + \varepsilon^{0}(A_1 u_2 + A_2 u_1 + A_3 u_0 - f + \frac{\partial u}{\partial t}) + \ldots \tag{2.20}$$

where A_1, A_2, and A_3 are operators defined as

$$A_1 = \frac{\partial}{\partial y_i} D_{ij} \frac{\partial}{\partial y_j},$$

$$A_2 = \frac{\partial}{\partial y_i} D_{ij} \frac{\partial}{\partial x_j} + \frac{\partial}{\partial x_i} D_{ij} \frac{\partial}{\partial y_j},$$

and $A_3 = \frac{\partial}{\partial x_i} D_{ij} \frac{\partial}{\partial x_j}$.

By equating ε^{-2} term to zero, we can notice that one can notice that the only Y-periodic solution is $u_0 = u_0(x)$.

From ε^{-1} term in equation (2.20), the following microscopic equation is derived based on the finding that u_0 is function of x only.

$$\frac{\partial}{\partial y_i} D_{ij} \frac{\partial u_1}{\partial y_j} + \frac{\partial}{\partial y_i} D_{ij} \frac{\partial u_0}{\partial x_j} = 0 \tag{2.21}$$

Because the variables are separated in the right hand side of equation (2.21), u_1 has the following form, based on the above-mentioned remark.

$$u_1 = -\chi^j(y) \frac{\partial u_0}{\partial x_i} + \bar{u}_0(x) \tag{2.22}$$

with $\int_Y \chi^j(y) dy = 0$.

Substitution of (2.21) into (2.22) yields the microscopic governing equation.

$$\frac{\partial}{\partial y_i} D_{ij} \frac{\partial \chi^p}{\partial y_j} - \frac{\partial}{\partial y_i} D_{ip} = 0 \tag{2.23}$$

where D_{ij} is the local diffusivity and χ^p is the characteristic concentration resulting from the p^{th} unit concentration gradient (p=1,2,and 3).

Finally, the ε^0 term can be expressed as

$$A_1 u_2 = -A_2 u_1 - A_3 u_0 + f - \frac{\partial u_0}{\partial t} \tag{2.24}$$

The condition that u_2 has a unique solution in Y is

$$\int_Y \left(- A_2 u_1 - A_3 u_0 + f - \frac{\partial u_0}{\partial t} \right) dY = 0 \tag{2.25}$$

Substitution of (2.22) into (2.25) yields the macroscopic governing equation.

$$\frac{\partial}{\partial x_i} \left\{ \frac{1}{|Y|} \int_Y \left(D_{ij} - D_{ip} \frac{\partial}{\partial y_p} \chi^j(y) \right) dY \right\} \frac{\partial u_0}{\partial x_j} = \frac{\partial u_0}{\partial t} - f \tag{2.26}$$

where $|Y| = \int_Y dY$.

From the observation of (2.26), the effective diffusivity can be defined as

$$D_{ij}^H = \frac{1}{|Y|} \int_Y \left(D_{ij} - D_{ip} \frac{\partial}{\partial y_p} \chi^j \right) dY \tag{2.27}$$

where D_{ij}^H is the homogenized diffusivity, D_{ij} is local diffusivity, and χ^j is the solution of the microscopic equation.

It should be noted that if the diffusion occurs only in the pore space, then the integration domain in equation (2.10) is confined within the pore. The macroscopic equation has the following form.

$$\frac{\partial}{\partial x_i} \left\{ \frac{1}{|Y|} \int_{Y_f} \left(D_{ij} - D_{ip} \frac{\partial}{\partial y_p} \chi^j \right) dY \right\} \frac{\partial u_0}{\partial x_j} = \phi \left(\frac{\partial u_0}{\partial t} - f \right) \tag{2.28}$$

where ϕ is the porosity of the medium.

2.5 Implementation of the Homogenization of Elasticity and Diffusivity

The effective elasticity and diffusivity were calculated using voxel based finite element codes. For elasticity, equation (2.13) is solved and used to calculate effective elasticity using (2.16), whereas the effective diffusivity is calculated from (2.27) by solving equation (2.23). The unit cell domain was discretized into voxel elements, or 8-node hexahedral elements. Periodic boundary conditions were implemented by assigning equivalent nodal constraints by assuming symmetries in the unit cell geometry and the local properties (Hassani 1996; Auriault and Lewandowska 2001). In this way, only one-eighth domain was considered if used in the microstructural topology optimization, which saved computational time and memory compared to the calculation on full unit cell domain. In addition, the element-by-element preconditioned conjugate method was used as a solver for the finite element analysis of the microscopic problems because of its efficiency when dealing with large degrees of freedom.

2.6 Cross-Property Bounds on Diffusivity and Bulk Modulus

There are upper and lower bounds on the effective properties for composite material for given material volume fractions. Hashin and Shtrikman derived well-known bounds for isotropic magnetic permeability and bulk/shear moduli using variational principles (Hashin and Shtrikman 1962; Hashin and Shtrikman 1963). The theoretical bounds for the effective magnetic permeability also hold for the effective diffusivity owing to the mathematical equivalency. For isotropic, three dimensional, solid-void phase composites, the upper bound on the effective bulk modulus and the effective diffusivity can be expressed in terms of the solid phase volume fraction and phase properties.

$$K_{\max}^{iso} = \frac{(3/4)\rho KG}{(1-\rho)K + (3/4)G} \tag{2.29}$$

$$D_{\max}^{iso} = \frac{2(1-\rho)D}{2+\rho} \tag{2.30}$$

where ρ is solid phase volume fraction, K and G are the bulk and shear moduli of solid phase and D is a free isotropic diffusion coefficient of a solute in the fluid phase. Figure 2.1 illustrates the bounds on the relative isotropic diffusivity and bulk modulus in terms of solid phase volume fraction. The competition between elasticity and mass transport is obvious from the plots.

When multiple, conflicting properties are considered simultaneously, there are cross-property bounds that connect those properties through the microstructure. Such cross-property bounds provide an achievable range of one property if the other is known. For cross-property bounds that link bulk modulus and isotropic conductivity (diffusivity), Gibiansky and Torquato derived the sharpest known cross-property bounds using translation methods (Gibiansky and Torquato 1996). The cross-property upper bounds for an ill ordered solid-void(fluid) phase ($K_2 / K_1 = \infty$ and $D_2 / D_1 = 0$) can be defined in diffusivity-bulk modulus phase plane with a hyperbola segment that passes through three points, $(D_{\max}^{iso}, 0)$, $(0, K_{\max}^{iso})$ and $((1-\rho)D_1, \rho K_2)$, where D_1 and K_2 are the diffusivity and bulk modulus of the void phase, $D_2 (= 0)$ and K_2 are the diffusivity and bulk modulus of the solid phase, and $D_{\max}^{iso}$ and $K_{\max}^{iso}$ are defined in equations (2.29) and (2.30), respectively. ρ is solid volume fraction.

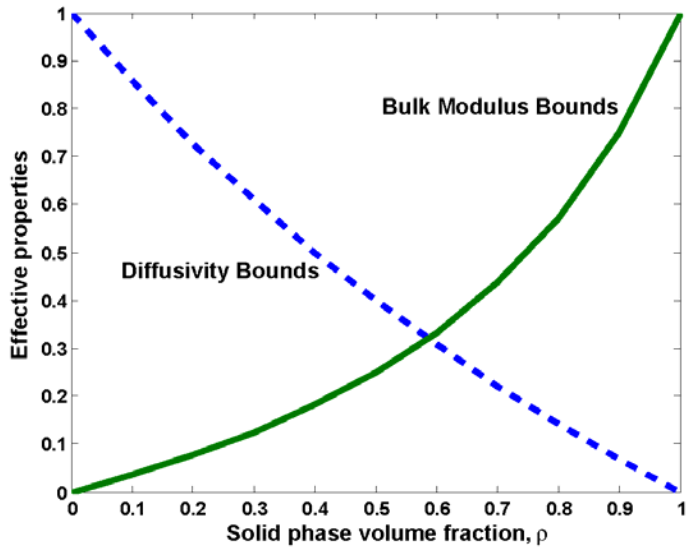

Figure 2.1 Normalized theoretical bounds on isotropic diffusivity and bulk modulus plotted as a function of solid phase volume fraction

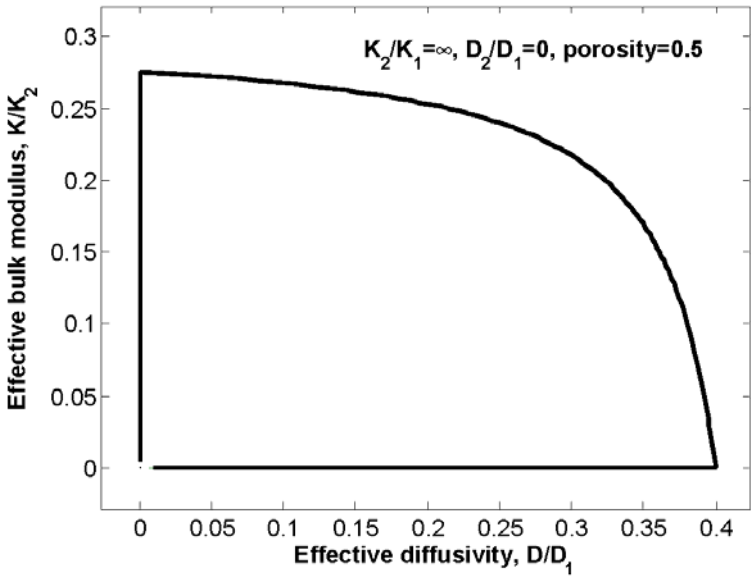

Figure 2.2 An example of cross-property bounds on the effective bulk modulus and diffusivity for ill-ordered composite, adapted from Gibiansky and Torquato (Gibiansky and Torquato 1996).

Figure 2.2 illustrates an example for the cross-property bounds in the diffusivity-bulk modulus phase for an ill ordered composite where $K_2 / K_1 = \infty$, $D_2 / D_1 = 0$ and 50% porosity. As can be seen, lower bounds are straight lines parallel to the axes. All feasible elasticity/diffusivity designs for a 50% porous material must lie within the lines in Figure 2.2. As noted by the authors, their cross-property bounds hold for both isotropic and cubic symmetric composites.

2.7 Homogenization of a Diffusion-Reaction Equation in Porous Media

The purpose of this section is the derivation of the homogenization of diffusion-reaction equations to be applied to the multiscale hydrolytic degradation modeling of the hierarchical scaffolds. The diffusion reaction based degradation model includes the ester bond concentration and diffusion of carboxylic acid end group. Especially, the diffusion of carboxylic acid end group in the pores is assumed much faster than that in the solid polymer matrix. The following derivation only considered such conditions, as a starting point.

2.7.1 Derivation

When a solute diffuses through a porous medium composed of two components with highly different diffusivities, anomalous diffusion behaviors occurs (Auriault and Lewandowska 1995). Consider the unit cell domain, $\Omega = \Omega_1 \bigcup \Omega_2$, where Ω_1 is the fluid saturated pore and Ω_2 is solid scaffold matrix. Ω_1 is continuous domain and Ω_2 is or is not continous (Figure 2.3).

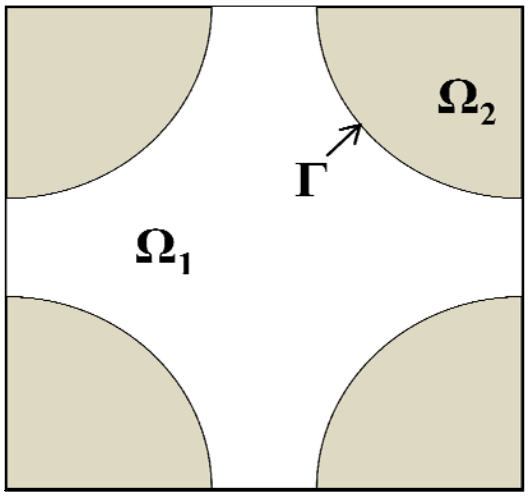

Figure 2.3 Schematic of a unit microstructure domain, showing two sub-regions with different diffusivities.

The diffusivity tensor is defined as

$$D_{ij} = \begin{cases} D_{ij}^{(1)} & \text{in } \Omega_1 \\ D_{ij}^{(2)} & \text{in } \Omega_2 \end{cases}$$

We assume $D_{ij}^{(1)} >> D_{ij}^{(2)}$.

The diffusion-reaction equation considered in this section is

$$\frac{\partial c^{\varepsilon}}{\partial t} - \frac{\partial}{\partial X_i} D_{ij} \frac{\partial c^{\varepsilon}}{\partial X_j} = f_i + g(c^{\varepsilon}) \qquad \text{in } \Omega \tag{2.31}$$

Each domain has its own variable: c_1 for solute concentration in Ω_1 and c_2 for solute concentration in Ω_2. The reaction is assumed to take place in Ω_2 only.

$$
\begin{aligned}
&\frac{\partial c_1^\varepsilon}{\partial t} - \frac{\partial}{\partial X_i} D_{ij}^{(1)} \frac{\partial c_2^\varepsilon}{\partial X_j} = 0 && \text{in } \Omega_1, \\
&\frac{\partial c_2^\varepsilon}{\partial t} - \frac{\partial}{\partial X_i} D_{ij}^{(2)} \frac{\partial c_2^\varepsilon}{\partial X_j} = f_i + g(c_2^\varepsilon) && \text{in } \Omega_2, \\
&- D_{ij}^{(2)} \frac{\partial c_2^\varepsilon}{\partial X_j} n_i = D_{ij}^{(1)} \frac{\partial c_1^\varepsilon}{\partial X_j} n_i && \text{on } \Gamma = \partial\Omega_2 \setminus \partial\Omega, \\
&c_2^\varepsilon = c_1^\varepsilon && \text{on } \Gamma = \partial\Omega_2 \setminus \partial\Omega,
\end{aligned}
\tag{2.32}
$$

where f_i is a source term, $g(c_2^\varepsilon)$ is a reaction term, and n_i is outward normal at pore surface.

This system in a porous medium provides four characteristic diffusion times according to the effective diffusivity in each phase (D_1 and D_2) and characteristic lengths of different scales (L for global scale and l for pore scale).

$$
\begin{aligned}
&T_{1L} = \frac{L^2}{D_1} \text{ and } T_{1l} = \frac{l^2}{D_1} \text{ in } \Omega_1, \\
&T_{2L} = \frac{L^2}{D_2} \text{ and } T_{2l} = \frac{l^2}{D_2} \text{ in } \Omega_2
\end{aligned}
\tag{2.33}
$$

The separation of scale can be represented by the effective diffusivity ratio between two phases, defined as in (Auriault and Lewandowska 1995).

$$
\frac{D_2}{D_1} = \varepsilon^q \tag{2.34}
$$

Then, different homogenized behaviors are derived according to the ratio of T_{1L}, characteristic diffusion time of a solute in Ω_1 at global scale and T_{2l}, characteristic diffusion time of a solute in Ω_2 at pore scale.

$$\frac{T_{2l}}{T_{1L}} = \varepsilon^{2-q} \tag{2.35}$$

If q < 2, or the diffusivities in solid and pore are of same order, the macroscopic equation was shown to have an effective property that is sum of the effective diffusivity in each phase (Auriault et al. 2009). It is also shown that the local diffusion becomes negligible if q=3. The following derivation of the homogenization is when q=2. A nondimensional version of the equations can be produced using the following representation of the dimensional variables, with the over bar denoting the dimensionless variables:

$$c_1 = c_{1c}\bar{c}_1;\ c_2 = c_{2c}\bar{c}_2;\ t = T\,\bar{t};\ X_i = Lx_i;\ D_1 = D_{1c}\overline{D}_1;\ D_2 = D_{2c}\overline{D}_2$$

$$\begin{aligned} &\frac{\partial \bar{c}_1^{\varepsilon}}{\partial \bar{t}} - T_{1L}\frac{D_c^1}{L^2}\frac{\partial}{\partial x_i}\overline{D}_{ij}^1\frac{\partial \bar{c}_1^{\varepsilon}}{\partial x_j} = 0 && \text{in } \Omega_1, \\ &\frac{\partial \bar{c}_2^{\varepsilon}}{\partial \bar{t}} - T_{1L}\frac{D_c^2}{L^2}\frac{\partial}{\partial x_i}\overline{D}_{ij}^2\frac{\partial \bar{c}_2^{\varepsilon}}{\partial x_j} = T_{1L}\left(\bar{f}_i + \bar{g}(c_2^{\varepsilon})\right) && \text{in } \Omega_2 \end{aligned} \tag{2.36}$$

If $T_{1L}\frac{D_c^1}{L^2} = O(1)$, indicating diffusion of a solute through Ω_1 is comparable to the diffusion by the boundary condition imposed at the global scale. Then

$$
\begin{aligned}
&\frac{\partial \bar{c}_1^{\varepsilon}}{\partial \bar{t}} - \frac{\partial}{\partial x_i}\overline{D}_{ij}^{1}\frac{\partial \bar{c}_1^{\varepsilon}}{\partial x_j} = 0 && \text{in } \Omega_1 \\
&\frac{\partial \bar{c}_2^{\varepsilon}}{\partial \bar{t}} - \varepsilon^2\frac{\partial}{\partial x_i}\overline{D}_{ij}^{2}\frac{\partial \bar{c}_2^{\varepsilon}}{\partial x_j} = T_{1L}\left(\bar{f}_i + \bar{g}(\bar{c}_2^{\varepsilon})\right) && \text{in } \Omega_2, \\
&-\varepsilon^2 D_c^2\frac{\partial \bar{c}_2^{\varepsilon}}{\partial x_i}n_i = D_c^1\frac{\partial \bar{c}_1^{\varepsilon}}{\partial x_i}n_i && \text{on } \Gamma \\
&\bar{c}_2^{\varepsilon} = \bar{c}_1^{\varepsilon} && \text{on } \Gamma
\end{aligned}
\tag{2.37}
$$

Using asymptotic expansions of $\bar{c}_1$ and $\bar{c}_2$, and the hierarchical derivative, we have the following equations from the orders of ε:

$$
\begin{aligned}
&\varepsilon^0\left(A_3\bar{c}_1^{(0)}(x,y) + A_2\bar{c}_1^{(1)}(x,y) + A_1\bar{c}_1^{(2)}(x,y) - \frac{\partial \bar{c}_1^{(0)}}{\partial \bar{t}}\right) \\
&\quad + \varepsilon^{-1}\left(A_2\bar{c}_1^{(0)}(x,y) + A_1\bar{c}_1^{(1)}(x,y)\right) + \varepsilon^{-2}\left(A_1\bar{c}_1^{(0)}(x,y)\right) = 0
\end{aligned}
\tag{2.38}
$$

$$
\frac{\partial \bar{c}_2^{(0)}}{\partial \bar{t}} - T_{1L}\left(\bar{f}_i + \bar{g}(\bar{c}_2^{(0)})\right) = A_1\bar{c}_2^{(0)}(x,y) \tag{2.39}
$$

where

$$
\begin{aligned}
A_1 &= \frac{\partial}{\partial y_i}\overline{D}_{ij}^{p}\frac{\partial}{\partial y_j} \\
A_2 &= \frac{\partial}{\partial x_i}\overline{D}_{ij}^{p}\frac{\partial}{\partial y_j} + \frac{\partial}{\partial y_i}\overline{D}_{ij}^{p}\frac{\partial}{\partial x_j} \qquad \text{(p=1, or 2)} \\
A_3 &= \frac{\partial}{\partial x_i}\overline{D}_{ij}^{p}\frac{\partial}{\partial x_j}
\end{aligned}
$$

The compatibility condition becomes

$$\varepsilon^{-1} D_c^1 \frac{\partial}{\partial y_i} \bar{c}_1^{(0)}(x,y) n_i + \varepsilon^0 \left(D_c^1 \frac{\partial}{\partial x_i} \bar{c}_1^{(0)}(x,y) + D_c^1 \frac{\partial}{\partial y_i} \bar{c}_1^{(1)}(x,y) \right) n_i$$
$$+ \varepsilon^1 \left(D_c^2 \frac{\partial}{\partial y_i} \bar{c}_2^{(0)}(x,y) + D_c^1 \frac{\partial}{\partial x_i} \bar{c}_1^{(1)}(x,y) + D_c^1 \frac{\partial}{\partial y_i} \bar{c}_1^{(2)}(x,y) \right) n_i + \ldots = 0 \tag{2.40}$$

First, from ε^{-2} of (2.38) and ε^{-1} of (2.40), the boundary value problem for $\bar{c}_1^{(0)}$ can be derived.

$$\begin{aligned} &\frac{\partial}{\partial y_i} \overline{D}_{ij}^1 \frac{\partial}{\partial y_j} \bar{c}_1^{(0)}(x,y) = 0 && \text{in } \Omega_1 \\ &D_c^1 \frac{\partial}{\partial y_i} \bar{c}_1^{(0)}(x,y) n_i = 0 && \text{on } \Gamma \end{aligned} \tag{2.41}$$

where it is clear that $\bar{c}_1^{(0)}(x,y) = \bar{c}_1^{(0)}(x)$.

From (2.39), the problem for $\bar{c}_2^{(0)}$ is defined.

$$\begin{aligned} &\frac{\partial \bar{c}_2^{(0)}}{\partial \bar{t}} - \frac{\partial}{\partial y_i} \overline{D}_{ij}^2 \frac{\partial}{\partial y_j} \bar{c}_2^{(0)}(x,y) = T_{1L}\left(\bar{f}_i + \bar{g}(\bar{c}_2^{(0)}) \right) && \text{in } \Omega_2 \\ &\bar{c}_2^{(0)} = \bar{c}_1^{(0)} && \text{on } \Gamma \end{aligned} \tag{2.42}$$

Assuming that $\bar{c}_1^{(0)}(x)$ is known on Γ by solving macroscopic equation which will be derived below, we can set $\bar{c}_2^{(0)}(x,y) = \bar{c}_1^{(0)}(x) + \bar{c}_2^{*}(x,y)$, where $\bar{c}_2^{*}$ is zero in Ω_1. Then the problem becomes

$$\frac{\partial(\bar{c}_2^* + \bar{c}_1^{(0)})}{\partial \bar{t}} - \frac{\partial}{\partial y_i} \overline{D}_{ij}^2 \frac{\partial}{\partial y_j} \bar{c}_2^* = T_{1L}\left(\bar{f}_i + \bar{g}(\bar{c}_2^* + \bar{c}_1^{(0)})\right) \text{ in } \Omega_2$$

$$\bar{c}_2^* = 0 \qquad \text{on } \Gamma \text{ and in } \Omega_1 \tag{2.43}$$

The equation for $\bar{c}_1^{(1)}$ is derived from ε^{-1} of (2.38) and ε^0 of (2.40).

$$\frac{\partial}{\partial y_i} \overline{D}_{ij}^1 \frac{\partial}{\partial y_j} \bar{c}_1^{(1)}(x, y) + \frac{\partial}{\partial y_i} \overline{D}_{ij}^1 \frac{\partial}{\partial x_j} \bar{c}_1^{(0)}(x) = 0 \qquad \text{in } \Omega_1$$

$$\overline{D}_{ij}^1 \frac{\partial}{\partial y_j} \bar{c}_1^{(1)}(x, y) n_i + \overline{D}_{ij}^1 \frac{\partial}{\partial x_j} \bar{c}_1^{(0)}(x) n_i = 0 \qquad \text{on } \Gamma \tag{2.44}$$

where $\frac{\partial}{\partial y_i} \overline{D}_{ij}^1 \frac{\partial}{\partial x_j} \bar{c}_1^{(0)}(x)$ appears as a forcing term. The solution can be the following form, using the separation of variable and linearity.

$$\bar{c}_1^{(1)}(x, y) = -\chi^j(y) \frac{\partial}{\partial x_j} \bar{c}_1^{(0)}(x) + \hat{c}^{(1)}(x) \tag{2.45}$$

Substitution of (2.45) into (2.44) yields a local problem for characteristic concentration in Ω_1 by global unit gradient.

$$-\frac{\partial}{\partial y_i} \overline{D}_{ij}^1 \frac{\partial}{\partial y_j} \chi^p(y) + \frac{\partial}{\partial y_i} \overline{D}_{ip}^1 = 0 \qquad \text{in } \Omega_1$$

$$\left(-\overline{D}_{ij}^1 \frac{\partial}{\partial y_j} \chi^p(y) + \overline{D}_{ip}^1\right) n_i = 0 \quad \text{on } \Gamma \tag{2.46}$$

The macroscopic problem for $\bar{c}_1^{(2)}$ is obtained from ε^0 of (2.38) and ε^1 of (2.40).

$$\frac{\partial}{\partial y_i}\overline{D}_{ij}^{1}\frac{\partial}{\partial y_j}\overline{c}_1^{(2)}(x,y)=\frac{\partial \overline{c}_1^{(0)}}{\partial \bar{t}}-\frac{\partial}{\partial y_i}\overline{D}_{ij}^{1}\frac{\partial}{\partial x_j}\overline{c}_1^{(1)}(x,y)$$
$$-\frac{\partial}{\partial x_i}\overline{D}_{ij}^{1}\frac{\partial}{\partial y_j}\overline{c}_1^{(1)}(x,y)-\frac{\partial}{\partial x_i}\overline{D}_{ij}^{1}\frac{\partial}{\partial x_j}\overline{c}_1^{(0)}(x) \quad \text{in } \Omega_1 \tag{2.47}$$

$$\left(D_c^2\frac{\partial}{\partial y_i}\overline{c}_2^{(0)}(x,y)+D_c^1\frac{\partial}{\partial x_i}\overline{c}_1^{(1)}(x,y)+D_c^1\frac{\partial}{\partial y_i}\overline{c}_1^{(2)}(x,y)\right)n_i=0 \text{ on } \Gamma$$

The condition for the existence of $\overline{c}_1^{(2)}$ is that the integration of the right hand side of the partial differential equation over Ω_1 should be zero. Taking integration over local domain, using divergence theorem and substitution of (2.45) into (2.47) yields

$$\begin{aligned}
&\phi_1\frac{\partial \overline{c}_1^{(0)}}{\partial \bar{t}}-\frac{\partial}{\partial x_i}\left\{\frac{1}{|Y|}\int_{\Omega_1}\left(\overline{D}_{ij}^{1}-\overline{D}_{ip}^{1}\frac{\partial \chi^j}{\partial y_p}\right)d\Omega\right\}\frac{\partial \overline{c}_1^{(0)}}{\partial x_j}\\
&=\frac{1}{|Y|}\int_{\Omega_1}\left(\frac{\partial}{\partial y_i}\overline{D}_{ij}^{1}\frac{\partial}{\partial y_j}\overline{c}_1^{(2)}+\frac{\partial}{\partial y_i}\overline{D}_{ij}^{1}\frac{\partial}{\partial x_j}\overline{c}_1^{(1)}\right)d\Omega\\
&=\frac{1}{|Y|}\int_{\Gamma}\left(\overline{D}_{ij}^{1}\frac{\partial}{\partial y_j}\overline{c}_1^{(2)}+\overline{D}_{ij}^{1}\frac{\partial}{\partial x_j}\overline{c}_1^{(1)}\right)n_i d\Gamma\\
&=-\frac{1}{|Y|}\int_{\Gamma}\overline{D}_{ij}^{2}\frac{\partial}{\partial y_j}\overline{c}_2^{(0)}n_i d\Gamma\\
&=-\frac{1}{|Y|}\int_{\Gamma}\overline{D}_{ij}^{2}\frac{\partial}{\partial y_j}\overline{c}_2^{*}n_i d\Gamma
\end{aligned} \tag{2.48}$$

where $|Y|=\int_{\Omega}d\Omega$ and ϕ_1 is volume fraction of Ω_1. Note that n_i is outward normal vector at the boundary of Ω_1 (into solid region).

In sum, the homogenization of reaction-diffusion equation in (2.37) is derived in this section. The solution converges in two-scale sense to $\bar{c}_1(x,t)+\bar{c}_2^*(x,x/\varepsilon,t)$, where $\bar{c}_2^*(x,x/\varepsilon,t)=0$ in Ω_1.

$$\phi_1 \frac{\partial \bar{c}_1^{(0)}}{\partial \bar{t}} - \frac{\partial}{\partial x_i}\overline{D}_{ij}^{H}\frac{\partial \bar{c}_1^{(0)}}{\partial x_j} = -\frac{1}{|\Omega|}\int_\Gamma \overline{D}_{ij}^{2}\frac{\partial}{\partial y_j}\bar{c}_2^* n_i d\Gamma \tag{2.49}$$

$$\frac{\partial \bar{c}_2^*}{\partial \bar{t}} - \frac{\partial}{\partial y_i}\overline{D}_{ij}^{2}\frac{\partial}{\partial y_j}\bar{c}_2^* = T_{1L}\left(\bar{f}_i + \bar{g}(\bar{c}_2^* + \bar{c}_1^{(0)})\right) - \frac{\partial \bar{c}_1^{(0)}}{\partial \bar{t}} \tag{2.50}$$

where

$$\overline{D}_{ij}^{H} = \frac{1}{|\Omega|}\int_{\Omega_1}\left(\overline{D}_{ij}^{1} - \overline{D}_{ip}^{1}\frac{\partial \chi^j}{\partial y_p}\right)d\Omega \text{ and}$$
$$-\frac{\partial}{\partial y_i}\overline{D}_{ij}^{1}\frac{\partial}{\partial y_j}\chi^p + \frac{\partial}{\partial y_i}\overline{D}_{ip}^{1} = 0 \tag{2.51}$$

This homogenized diffusion-reaction system was shown to have unique solution (Pankratov et al. 2003).

2.7.2 Solution Process

In the equation (2.49), microscopic equation and macroscopic equation are coupled. Diffusive flux from the solid (Ω_1) is averaged over the solid-void boundary to serve as source term in the macroscopic equation, while the microscopic equation involves the macroscopic variable ($\bar{c}_1^{(0)}$) and its time derivative ($\partial \bar{c}_1^{(0)}/\partial \bar{t}$). In order to solve this system, the right hand side of the macroscopic equation should be evaluated at every x_i in the macroscopic domain, at which position the microscopic equation should be solved

using $\bar{c}_1^{(0)}(x_i)$ and $\left.\frac{\partial \bar{c}_1^{(0)}}{\partial \bar{t}}\right|_{x_i}$. Then, the macroscopic equation can be solved with the source term. Furthermore, this calculation is repeated every time step.

Solution step is as follows:

1. At $t = t_k$, the time dependent diffusion-reaction equation (2.50) is solved using $\bar{c}_1^{(0)}(x_i, t_k)$ and $\frac{\partial \bar{c}_1^{(0)}(x_i, t_k)}{\partial \bar{t}}$ at every nodal point of the global domain. This gives $\bar{c}_2^{*}(x_i, t_{k+1})$.
2. The right hand side of equation (2.49) is also evaluated from the solution of (2.50) at every nodal points of the global domain.
3. Then, equation (2.49) is solved to calculate $\bar{c}_1^{(0)}(x_i, t_{k+1})$ and $\frac{\partial \bar{c}_1^{(0)}(x_i, t_{k+1})}{\partial \bar{t}}$.
4. Repeat steps 1 through 3 until the system reaches steady state.

2.8 Homogenization of Stokes Flow

2.8.1 Derivation

Stoke equation governs the flow of Newtonian, incompressible, viscous fluid in porous media. Here the homogenization of Stokes flow in porous media is derived from the microscopic scale, following Auriault et al. (Auriault et al. 2005).

Let L be the characteristic length for macroscopic scale and l be the characteristic length for microscopic scale. L can be the scaffold size whereas l can be pore size. The separation of scale can then be described by

$$\varepsilon = \frac{l}{L} << 1 \tag{2.52}$$

The momentum balance equation is derived from Navier-Stokes equation by neglecting inertial term.

$$\frac{\partial}{\partial X_j}\mu\frac{\partial v_i}{\partial X_j} - \frac{\partial p}{\partial X_i} = 0 \quad \text{in } \Omega_p \tag{2.53}$$

where μ is fluid viscosity, v_i is velocity, and p is pressure. The incompressibility condition is described by the continuity equation.

$$\frac{\partial v_i}{\partial X_j} = 0 \quad \text{in } \Omega_p \tag{2.54}$$

The adherence (no slip) condition is

$$v_i = 0 \quad \text{on } \Gamma \tag{2.55}$$

The nondimensionalized momentum balance equation becomes

$$\overline{\mu}\frac{\partial^2 \overline{v}_i}{\partial y_j \partial y_j} - Q\frac{\partial \overline{p}}{\partial y_i} = 0 \tag{2.56}$$

where $y_i = X_i / l$, $\overline{\mu} = \mu/\mu_c$, $\overline{v}_i = v_i / v_c$, $\overline{p} = p/p_c$, and $Q = \frac{p_c l}{\mu_c v_c}$, which is the ratio of pressure to viscous force. The quantities with subscription c imply their characteristic values.

The local viscous flow is driven by a macroscopic pressure gradient.

$$\frac{\mu_c v_c}{l^2} = O\left(\frac{p_c}{L}\right) \tag{2.57}$$

Thus

$$Q = \frac{p_c}{L}\frac{l^2}{\mu_c v_c}\frac{L}{l} = \frac{1}{\varepsilon}\frac{p_c}{L}\frac{l^2}{\mu_c v_c} = O\left(\frac{1}{\varepsilon}\right) \tag{2.58}$$

The nondimensionalized Stokes equations become

$$\overline{\mu}\frac{\partial^2 \overline{v}_i}{\partial y_j \partial y_j} - \frac{1}{\varepsilon}\frac{\partial \overline{p}}{\partial y_i} = 0 \text{ in } \Omega_p \tag{2.59}$$

$$\frac{\partial \overline{v}_i}{\partial y_j} = 0 \text{ in } \Omega_p \tag{2.60}$$

$$\overline{v}_i = 0 \text{ on } \Gamma \tag{2.61}$$

The homogenization of the Stokes equations can be derived by the perturbation of the velocity and pressure with ε.

$$\overline{v}_i = \overline{v}_i^{(0)}(x,y) + \varepsilon \overline{v}_i^{(1)}(x,y) + \varepsilon^2 \overline{v}_i^{(2)}(x,y) + \ldots \tag{2.62}$$

$$\overline{p}^{\varepsilon} = \overline{p}^{(0)}(x,y) + \varepsilon \overline{p}^{(1)}(x,y) + \varepsilon^2 \overline{p}^{(2)}(x,y) + \ldots \tag{2.63}$$

and the hierarchical derivative from local scale

$$\frac{\partial}{\partial y_j} \to \frac{\partial}{\partial y_j} + \varepsilon \frac{\partial}{\partial x_j} \tag{2.64}$$

$$\frac{\partial^2}{\partial y_j \partial y_j} \to \frac{\partial^2}{\partial y_j \partial y_j} + \varepsilon\left(\frac{\partial^2}{\partial x_j \partial y_j} + \frac{\partial^2}{\partial y_j \partial x_j}\right) + \varepsilon^2 \frac{\partial^2}{\partial x_j \partial x_j} \tag{2.65}$$

we can get series of equations from each term collected by equal powers of ε.

$$0 = \varepsilon^{-1}\left(-\frac{1}{\varepsilon}\frac{\partial \overline{p}^{(0)}}{\partial y_i}\right) + \varepsilon^{0}\left(\overline{\mu}\frac{\partial^2 \overline{v}_i^{(0)}}{\partial y_j \partial y_j} - \frac{\partial \overline{p}^{(1)}}{\partial y_i} - \frac{\partial \overline{p}^{(0)}}{\partial x_j}\right) + \varepsilon^{1}\left(\overline{\mu}\frac{\partial^2 \overline{v}_i^{(1)}}{\partial y_j \partial y_j} - \frac{\partial \overline{p}^{(1)}}{\partial x_j} + \left(\frac{\partial^2 \overline{v}_i^{(0)}}{\partial x_j \partial y_j} + \frac{\partial^2 \overline{v}_i^{(0)}}{\partial y_j \partial x_j}\right) - \frac{\partial \overline{p}^{(2)}}{\partial y_j}\right) + \ldots \quad \text{in } \Omega_p \tag{2.66}$$

$$\frac{\partial \overline{v}_i^{(0)}}{\partial y_j} + \varepsilon\left(\frac{\partial \overline{v}_i^{(0)}}{\partial x_j} + \frac{\partial \overline{v}_i^{(1)}}{\partial y_j}\right) + \varepsilon^2\left(\frac{\partial \overline{v}_i^{(1)}}{\partial x_j} + \frac{\partial \overline{v}_i^{(2)}}{\partial y_j}\right) = 0 \quad \text{in } \Omega_p \tag{2.67}$$

From the lowest order of ε,

$$\frac{\partial \overline{p}^{(0)}}{\partial y_i} = 0 \tag{2.68}$$

we notice that $\overline{p}^{(0)} = \overline{p}^{(0)}(x)$.

From the zero order of ε, together with compatibility and adherence condition, the local flow equation is derived.

$$\overline{\mu}\frac{\partial^2 \overline{v}_i^{(0)}}{\partial y_j \partial y_j} - \frac{\partial \overline{p}^{(1)}}{\partial y_i} - \frac{\partial \overline{p}^{(0)}}{\partial x_j} = 0 \text{ in } \Omega_p^* \tag{2.69}$$

$$\frac{\partial \overline{v}_i^{(0)}}{\partial y_j} = 0 \quad \text{in } \Omega_p^* \tag{2.70}$$

$$\overline{v}_i^{(0)} = 0 \quad \text{on } \Gamma^* \tag{2.71}$$

where $\overline{v}_i^{(0)}$ and $\overline{p}^{(1)}$ are Ω-periodic. This system is known to have a unique solution of characteristic velocity in the following form

$$\overline{v}_i^{(0)} = -\frac{\overline{k}_{ij}}{\overline{\mu}}\frac{\partial \overline{p}^{(0)}}{\partial x_j} \tag{2.72}$$

and the pressure solution is in the form

$$\overline{p}^{(1)} = -a_j^* \frac{\partial \overline{p}^{(0)}}{\partial x_j} + p^{*(1)}(x_i) \tag{2.73}$$

where $\frac{1}{|\Omega_p|}\int_{\Omega_p} a_j^* d\Omega = 0$.

Substituting (2.72) and (2.73) into the equation (2.69) yields the local problem.

$$\frac{\partial^2 \overline{k}_{ij}}{\partial y_j \partial y_j} - \frac{\partial a_j^*}{\partial y_i} + \delta_{ij} = 0$$

$$\frac{\partial \overline{k}_{ij}^{(0)}}{\partial y_j} = 0 \quad \text{in } \Omega_p^* \tag{2.74}$$

$$\overline{k}_{ij}^{(0)} = 0 \quad \text{on } \Gamma^*$$

By averaging the second term of the compatibility condition in (2.67), the effective permeability can be calculated.

$$\overline{K}_{ij} = \frac{1}{\overline{\mu}} \left\langle \overline{k}_{ij} \right\rangle \tag{2.75}$$

where $\overline{K}_{ij}$ is the effective permeability in nondimensional form and $\langle \cdot \rangle = \frac{1}{|\Omega|}\int_{\Omega_p} \cdot \, d\Omega$.

Darcy's law in the macroscopic scale is described as

$$\left\langle \overline{v}_i^{(0)} \right\rangle = -\overline{K}_{ij} \frac{\partial \overline{p}^{(0)}}{\partial x_j} \tag{2.76}$$

$$\frac{\partial \left\langle \overline{v}_i^{(0)} \right\rangle}{\partial x_j} = 0 \tag{2.77}$$

where (2.77) is derived from volume averaging of the second term of (2.67).

In dimensional form, the effective permeability

$$K_{ij} = -l^2 \overline{K}_{ij} \tag{2.78}$$

2.8.2 Implementation and Validation

Voxel based finite element codes were implemented for the evaluation of the effective permeability. The microstructural geometry is represented using binary variables assigned on each voxel element: 0 for pore space and 1 for solid. The finite element modeling and analysis is confined within pore space. In order to calculate the effective permeability, the local Stokes problem (2.74) was solved using a stabilized mixed finite element formulation following (Hughes et al. 1986). The advantage of this formulation is that equal order elements can be used for both velocity and pressure. However, the assembled matrix in the finite element formulation is asymmetric. Thus, taking advantage of regular voxel elements, an element-by-element preconditioned bi-conjugate gradient (EBE-PBCG) method was adapted as non-symmetric matrix solver. Although it is generally known that the PBCG method does not always converge to a solution, it works for most of our permeability analysis on the scaffold microstructures.

The permeability code were validated in comparison with the results by (Lee et al. 1996), where the effective permeability values were calculated on Wigner-Seitz grain (Figure 2.4) and compared to empirical formulation for permeability through media with general types of inclusions such as spheres, cubes and hexagonal prism. As the authors commented, the homogenized permeability values are comparable and in trend with the empirical formula, with slightly lower estimates. Our permeability code also repeated the same results (Figure 2.5). More deviation from the empirical permeability values may be attributed to the voxel modeling of the Wigner-Seitz grain unit microstructure.

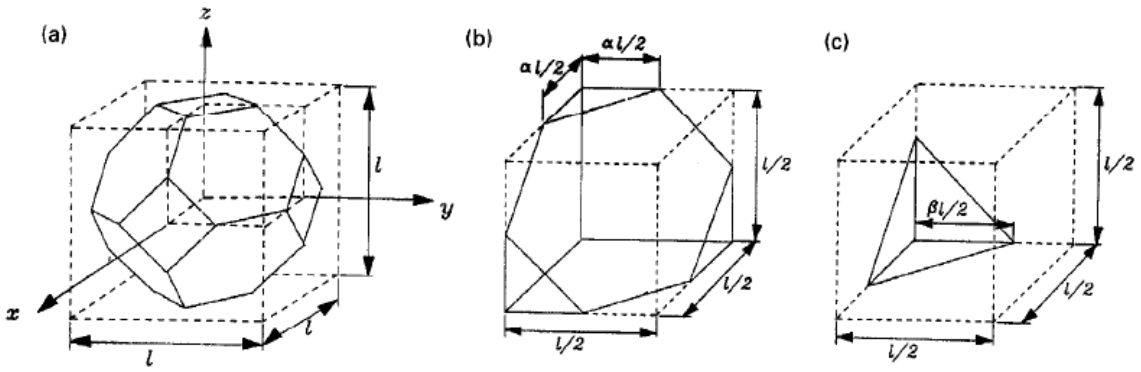

Figure 2.4 Unit microstructure of Wigner-Seitz grain, from (Lee et al. 1996).

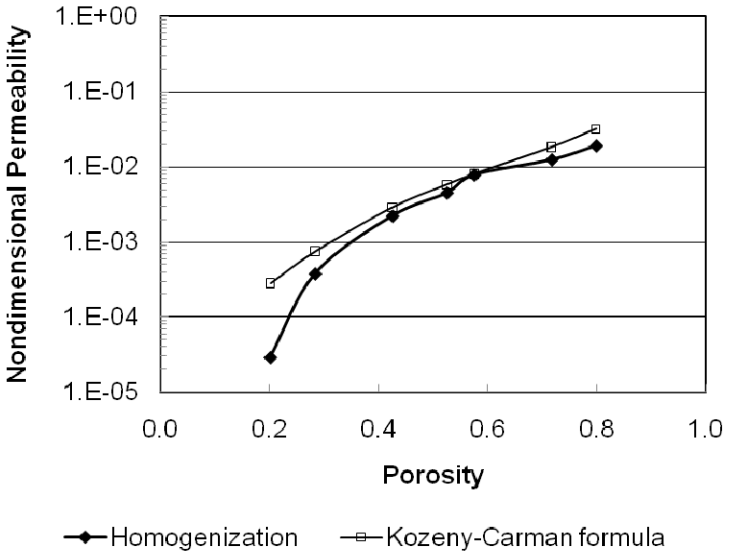

Figure 2.5 The effective permeability by the homogenization code was compared to an empirical formulation used in (Lee et al. 1996).

2.9 Conclusion

In this chapter, the homogenization linear elasticity, diffusion, diffusion-reaction, and Stokes flow were derived. Using the asymptotic expansion of the variables, the homogenization method can provide rigorous theoretical background in the analysis of elastic and transport problems in the hierarchical porous scaffolds. This homogenization process allows us to characterize the functional properties of the designed scaffolds, as well as to tailor the properties when designing scaffolds with tissue-specific properties.

CHAPTER 3

SCAFFOLD MICROSTRUCTURE DESIGN USING THE MICROSCTRUCTURAL OPTIMIZATION

3.1 Introduction

Scaffold pore architectures such as pore size, pore shape, and interconnectivity are known to affect the regenerate tissue inside. These microstructural parameters are also correlated with mechanical and mass transport properties of the scaffolds. Thus, the goal of the design of tissue engineering scaffolds is to find optimal microstructures that achieve prescribed mechanical and mass transport properties.

One way to achieve these diverse design goals is adapting optimization schemes in hierarchical scaffold design (Hollister 2005). In the hierarchical scaffold design scheme, unit microstructures, or unit cells (structural unit, not biological cells) are chosen from unit cell libraries and assembled to form a scaffold global shape that fits into anatomical defects. The mechanical and mass transport properties of the scaffold are computed using the homogenization method based on double-scale asymptotic expansion (Bensoussan et al. 1978; Sanchez-Palencia et al. 1987). Pore architectures can be designed with predefined geometries such as three orthogonal cylindrical pores or spherical pores. Hollister et al. optimized pore diameters of scaffolds with three orthogonal cylindrical

pores using the homogenization method and empirically fitted polynomials that relate pore diameters and the effective stiffness tensor (Hollister et al. 2002). Transport requirements were considered by imposing a lower bound constraint on porosity.

In more general cases, however, new microstructures with target properties can be sought using topology optimization (Bendsoe and Kikuchi 1988; Sigmund 1994; Sigmund 1995). Topology optimization distributes material within a unit microstructure such that the final structure meets specified design targets. Lin et al. adapted the topology optimization to find scaffold microstructures that achieved target anisotropic elastic constants (Lin et al. 2004). Hollister and Lin further extended the method by introducing effective permeability to the optimization scheme to design scaffolds with maximized permeability (Hollister and Lin 2007). However, the permeability was not coupled with the mechanical property in the optimization procedure, so that maximizing permeability could affect the mechanically optimized microstructure.

Recently, several multifunctional material design schemes based on the topology optimization have been proposed. Guest and Prevost proposed a general 3D microstructure design scheme using the topology optimization method to achieve maximized bulk modulus and isotropic permeability (Guest and Prevost 2006). They optimized microstructures by differentially weighting mechanical and transport terms in the objective, allowing designers to tailor the material properties. de Kruijf et al found optimal structures with maximized bulk modulus and thermal conductivity by minimizing both mechanical and thermal compliance in 2D (de Kruijf et al. 2007). The authors explored Pareto optimality by varying weights for mechanical and transport properties. Challis et al., by a level set method, presented the design of isotropic unit structures with

maximized bulk modulus and isotropic conductivity (Challis et al. 2008). The authors also explored design changes with the different combinations of weighting factors.

The design of multifunctional material structures with maximized properties is gaining interest in many engineering fields. Tissue engineering scaffolds, however, must be tailored to a wide range of mechanical and mass transport properties, including cross property relationships that fall well within the interior of cross-property bounds, not just on the boundaries of the cross-property bounds. For example, cartilage needs low mass transport and mechanical properties (Kemppainen and Hollister 2010), which lay well within the interior of the mass transport and mechanical cross-property bounds.

Thus, the goal of this study was to explore possible microstructure designs with various combinations of effective bulk moduli and diffusivities. In order to design microstructures with ranges of mechanical and mass transport properties, we adapted a local microstructure topology optimization scheme based on the SIMP method for target optimization. The target properties were chosen within known cross-property bounds connecting effective bulk modulus and isotropic diffusivity. Various microstructures were designed and utilized within actual tissue engineering scaffolds. A porous biodegradable interbody fusion cage was designed as a biomedical application of multifunctional microstructures by integrating the result from global topology optimization and the local microstructure optimization. The resulting integrated local and globally designed structures were then built using solid free-form fabrication techniques.

3.2 Tailoring Scaffold Properties

3.2.1 Material Interpolations

Microstructure topology optimization computes the optimal topology of scaffold microstructure by distributing material density within the unit cell domain under design objectives and constraints. The design domain is discretized with the finite elements assigned with density values, ranging from 0 through 1. In this relaxed problem, material laws should be defined to relate element densities and local material properties. In addition, the intermediate density values are penalized to have a final discrete design. The most common local material law is the Solid Isotropic Microstructure with Penalization (SIMP) (Bendsoe and Sigmund 1999). We utilized the SIMP method for elasticity:

$$C_{ijkl} = \rho^p C_{ijkl}^{base}, \quad (p > 1) \tag{3.1}$$

where C_{ijkl} is the element stiffness tensor, ρ is the element density, p is a penalization factor, and C_{ijkl}^{base} is the stiffness tensor for the base material. For the diffusivity, a SIMP-like material law can be applied to the interpretation of the intermediate densities with penalization,

$$D_{ij} = (1-\rho)^p D_{ij}^{base}, \quad (p > 1) \tag{3.2}$$

where D_{ij} is the element diffusivity tensor, ρ is the element density, p is a penalization factor, and D_{ij}^{base} is the free diffusivity tensor for the fluid phase. With the local material laws defined for both stiffness and diffusivity, the objective function and sensitivity derivatives are derived with respect to material density ρ, and the optimization problem can be solved by updating ρ at each iteration.

For the phase base material, we used unit isotropic diffusivity, D=1 for the void phase. For the base material solid phase, we chose Poisson's ratio equal to 1/3 with a Young's modulus of 1, which yields a bulk modulus of 1. In this case, the designed properties could be easily compared within the cross-property bounds normalized to base material properties.

3.2.2 Problem Statement for Target Optimization

In order to tailor the material properties directly, the optimization problem was defined to minimize the error between the target and the effective bulk moduli and diffusivities, with constraints on porosity:

$$\begin{aligned} &\text{minimize} \quad f = w_1\left(\frac{K^H}{K^*}-1\right)^2 + w_2\left(\frac{D^H}{D^*}-1\right)^2 + w_3 f_{cubic} \\ &\text{subject to} \quad \phi_{\text{lb}} \le \sum_{i=1}^{N}\frac{1-\rho_i}{N} \le \phi_{\text{ub}}, \\ &\qquad\qquad 0 < \rho_i \le 1 \end{aligned} \tag{3.3}$$

where K^H is the homogenized bulk modulus, K^* is the target bulk modulus, D^H is the homogenized isotropic diffusivity, D^* is the target isotropic diffusivity, f_{cubic} is the cubic error function and w_i ($i = 1,\ldots,3$) are weighting factors, ϕ_{lb} and ϕ_{ub} are the upper and lower bounds of porosity, ρ_i is i-th element density, and N is the total number of elements.

Pursuing isotropic or cubic symmetric material microstructures, the effective bulk modulus was converted from elastic stiffness tensor components assuming isotropic/cubic symmetry in the final result.

$$K^H = \frac{1}{3}\left(\frac{C^H_{1111} + C^H_{2222} + C^H_{3333}}{3} + \frac{2\left(C^H_{1122} + C^H_{2233} + C^H_{1133}\right)}{3} \right) \tag{3.4}$$

In the same way, the effective diffusivities were evaluated as average of the diagonal terms in diffusivity tensor.

$$D^H = \frac{D^H_{11} + D^H_{22} + D^H_{33}}{3} \tag{3.5}$$

The cubic error function is defined to minimize the differences among three normal components, three off-diagonal terms, and thee shear terms in the stiffness tensor components, respectively.

$$\begin{aligned} f_{cubic} = & \left(\frac{C^H_{2222}}{C^H_{1111}} - 1 \right)^2 + \left(\frac{C^H_{3333}}{C^H_{2222}} - 1 \right)^2 + \left(\frac{C^H_{1111}}{C^H_{3333}} - 1 \right)^2 \\ & + \left(\frac{C^H_{2233}}{C^H_{1122}} - 1 \right)^2 + \left(\frac{C^H_{1133}}{C^H_{2233}} - 1 \right)^2 + + \left(\frac{C^H_{1122}}{C^H_{1133}} - 1 \right)^2 \\ & + \left(\frac{C^H_{1313}}{C^H_{2323}} - 1 \right)^2 + \left(\frac{C^H_{1212}}{C^H_{1313}} - 1 \right)^2 + \left(\frac{C^H_{2323}}{C^H_{1212}} - 1 \right)^2 \end{aligned} \tag{3.6}$$

where C^H_{ijkl} are the components of the homogenized stiffness tensor. This multiobjective formulation can be easily converted to a formulation in which one of the target properties is optimized while the other is constrained.

3.2.3 Implementation

Topology optimization, in its relaxed formulation, still requires additional treatments to avoid known numerical instabilities such as checkerboard patterns and mesh dependencies (Sigmund and Petersson 1998). We applied a nonlinear filtering scheme to the sensitivity derivatives to prevent checkerboard patterns and mesh dependency as proposed by Sigmund (Sigmund 1994). Assuming unit cell size of 1 mm

in each direction, a filter radius of 3 elements was chosen to maintain a minimum physical feature size (0.15mm) for the 40×40×40 element unit cells. When the mesh resolution was increased to 60×60×60, the filter radius was increased to 4 elements to maintain the minimum physical feature size (0.13mm). Finally, to solve the optimization problem, the Method of Moving Asymptotes (MMA) was adopted to provide greater efficiency in solving problems with a large number of variables and a small number of constraints (Svanberg 1987).

3.3 Results

Our results demonstrate that the properties of the microstructures can be tailored to meet various scaffold requirements such as stiffness and mass transport using topology optimization with SIMP interpolation and sensitivity filtering. Target design points were chosen close to the cross-property upper bounds. Figure 3.1 illustrates various microstructural architectures obtained in this study and the achieved properties are presented in Table 3.1. The mesh resolution for microstructures (A), (C), (E), (G), and (F) was 60×60×60, and the mesh resolution for the other microstructures was 40×40×40. The designed microstructures were identified within the cross-property bounds in Figure 3.2.

Bear in mind that the porosities of the designed microstructures satisfied the constraints despite the lack of an exact match in the corresponding cross-property bounds. This is because the porosity constraints were set at a small range around the target porosity. For example, the porosity constraints were set less than 52% and greater than 48% for the design of 50% porosity microstructures. Nonetheless, there was excellent agreement between the target and designed bulk moduli and diffusivities Figure 3.3.

Because of the theoretical cross-property bounds for 50~60% porosities, the maximum normalized diffusivities are 0.4 and 0.5, respectively. Thus, we may consider diffusivity over 0.3 as high diffusivity for 50~60 % porosity materials.

3.3.1 Microstructures with High Diffusivity

Microstructures with relatively high diffusivity designed for either 50% or 60% porosity approached the cross-property upper bound, as depicted in Figure 3.1-D through Figure 3.1-H. The properties of the microstructures illustrated in these figures were isotropic. It should be noted that the designed microstructures have different topologies while the achieved properties were close to each other. Interestingly, the property pair of the microstructure in Figure 3.1-F is the closest to the cross-property upper bound, implying that the structure is optimal. Furthermore those microstructures designed to have 60% porosity showed lower bulk modulus of approximately 0.1 of that of the solid phase. When the structures were specified within cross-property bounds, both structures again have near optimal properties because the properties are close to the upper bounds (Figure 3.2).

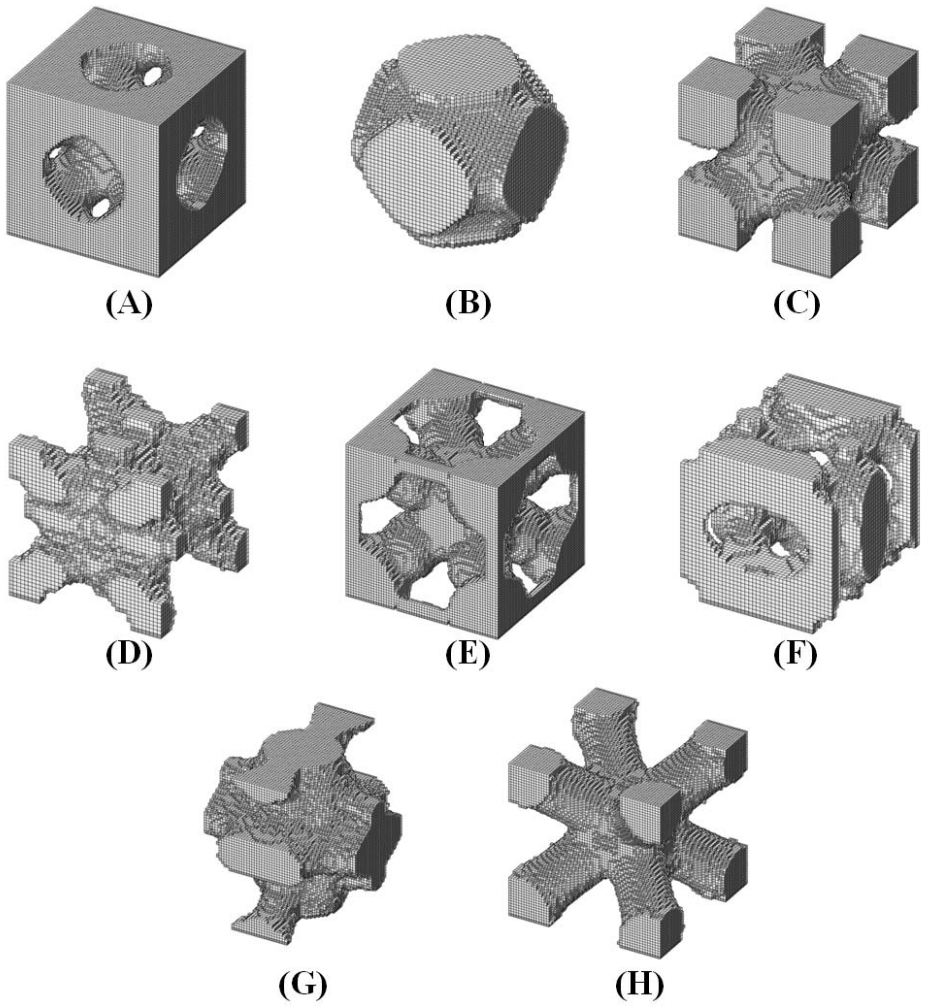

Figure 3.1 Microstructures obtained by targeting bulk modulus and diffusivity close to the upper cross-property bounds, for 30% porosity (a, b and c), 50% porosity (d, e and f) and 60% porosity (g and h)

Table 3.1 Properties of microstructures tailored with target bulk moduli and diffusivities.

Microstructures	Porosity	Diffusivity*	Bulk Modulus*	Young's Modulus*	Poisson's ratio
A	0.2825	0.1276	0.3734	0.4875	0.2824
B	0.3030	0.1340	0.3565	0.5273	0.2535
C	0.2935	0.1616	0.3317	0.4277	0.2851
D	0.4831	0.3016	0.1512	0.2258	0.2511
E	0.4828	0.3156	0.1624	0.1955	0.2994
F	0.5037	0.3330	0.1522	0.2251	0.2535
G	0.5802	0.3556	0.1246	0.2442	0.1734
H	0.5882	0.4164	0.1114	0.0973	0.3544

***** The values are normalized to the base material properties.

3.3.2 Microstructures with Low Diffusivity

Microstructures designed to achieve low diffusivity for 30% porosity were also close to the corresponding cross-property upper bounds (Figure 3.1-A through C). The optimized structures have thick members across the diagonal of the unit cell domain to achieve high bulk modulus, and small pore diameters to decrease diffusivity. The normalized diffusivities of these microstructures were between 0.12 and 0.17 (Table 3.1). These low diffusivity structures are also close to the upper cross-property bounds due to high bulk modulus (Figure 3.2).

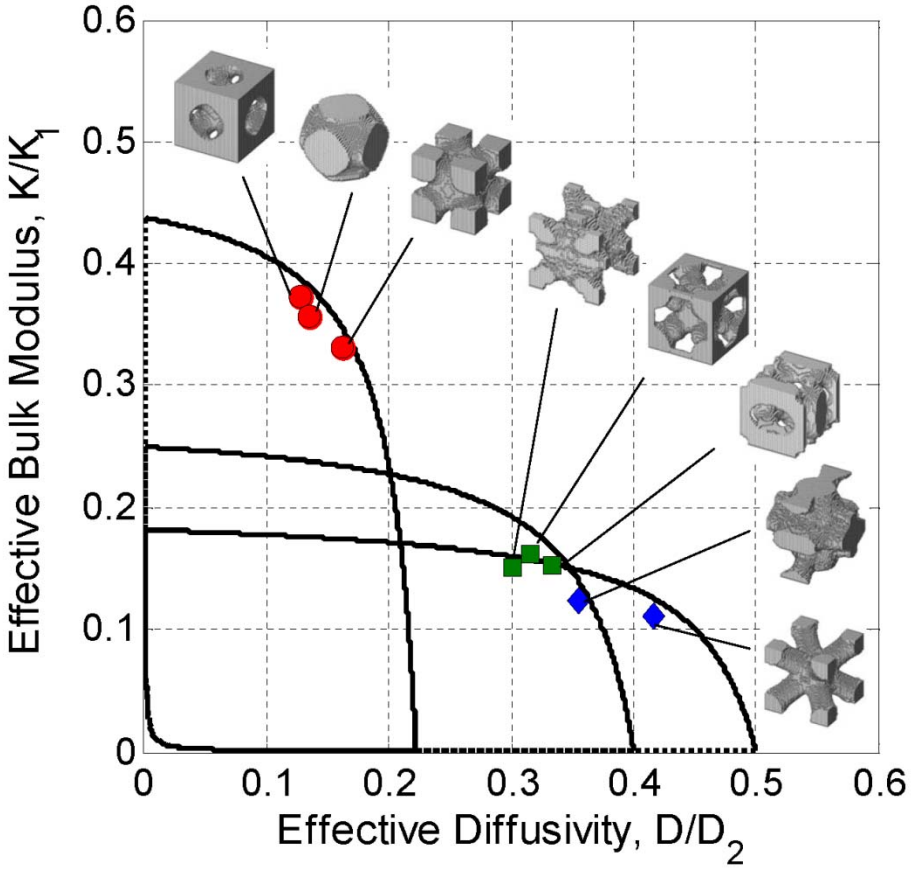

Figure 3.2 Microstructures designed to achieve properties close to the upper cross-property bounds are specified within the cross-property bounds

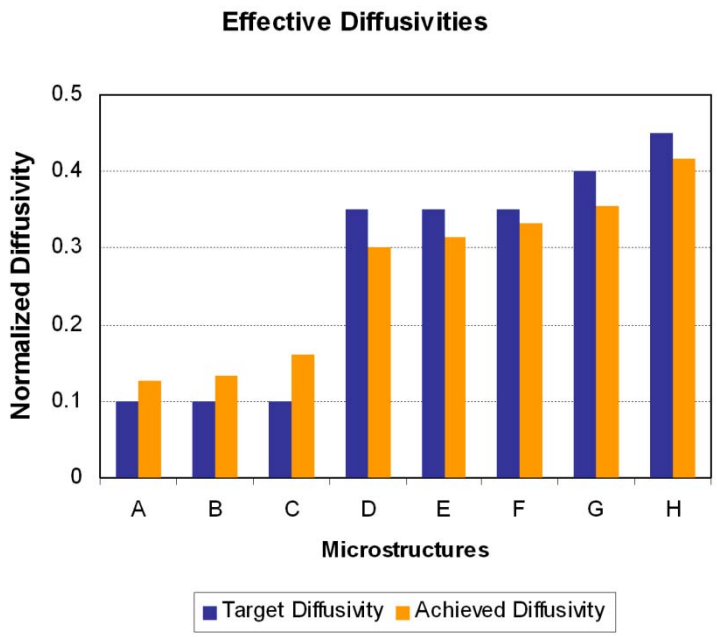

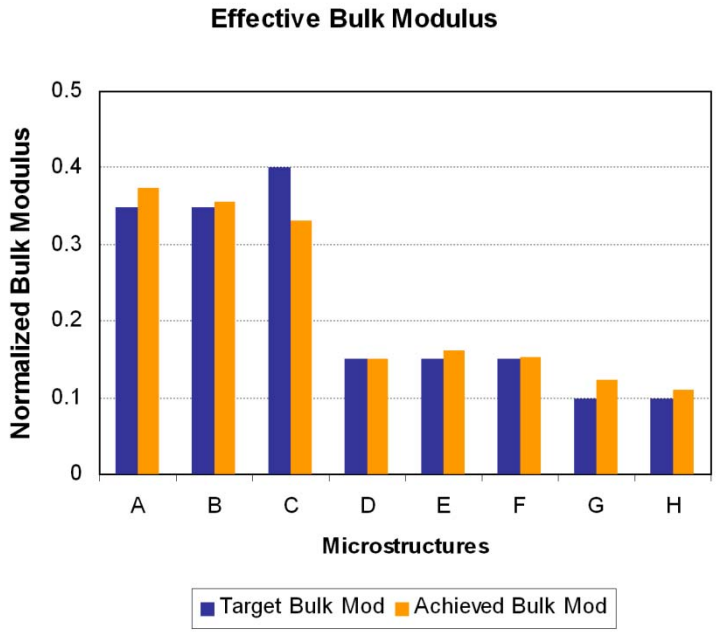

Figure 3.3 The achieved diffusivities (upper) and bulk moduli (lower) were compared with target properties for the microstructures presented in Figure 3.1

3.3.3 Microstructure targeting Low Diffusivity and Low Bulk Modulus

A microstructure designed with low diffusivity and low bulk modulus achieved the target properties although it contains significant intermediate densities. For cartilage tissue engineering applications, microstructures with low modulus and low diffusivity are desired. Such microstructures lie within the interior of the cross property bounds, well away from the upper limits that have been the target of most multiphysics microstructural topology optimization applications. These targets present significant challenges as the increase of material will increase bulk modulus (although decreasing diffusivity) and vice versa, the opposite of the design goal.

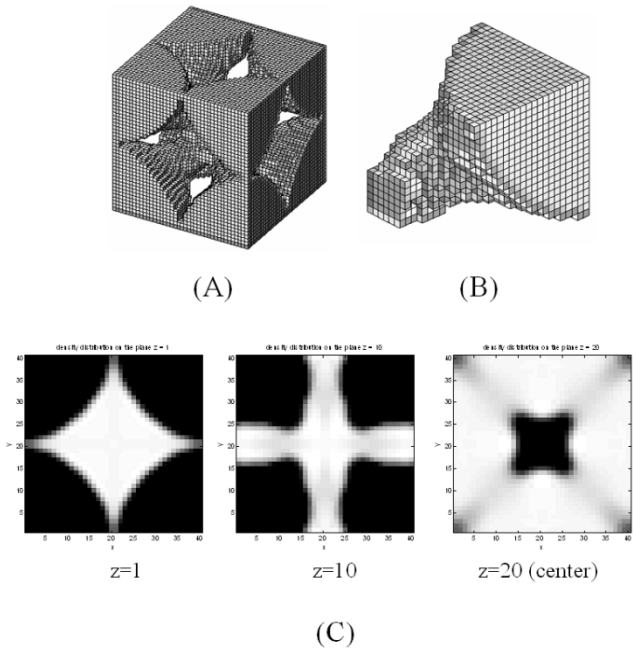

Figure 3.4 (A) Microstructures with low diffusivity and low bulk modulus, (B) 1/8 of the designed microstructure and (C) representative cross-sectional view of the structure.

To eliminate the intermediate densities, we used post processing. We designed a low diffusivity and low bulk modulus microstructure, by targeting a diffusivity of 0.1 and a bulk modulus of 0.1. However, the result of the post processing changed the very properties we were trying to target. The intermediate density values were interpolated using SIMP model. After applying a threshold, the properties shifted towards cross-property upper bounds.

One interpretation as to why we got intermediate densities is that the algorithm converged to local minimum before all densities were penalized. We employed the convention of Sigmund's continuation method to avoid convergence to a local minimum (Sigmund 1995). However as expected, this essentially heuristic approach could not sufficiently penalize the intermediate densities: the final mechanical and transport properties are a diffusivity of 0.12 and a bulk modulus of 0.1, which is not a totally satisfactory solution to the problem. The full structure and $1/8^{th}$ of the structure are shown in Figure 3.4-A and Figure 3.4-B, respectively. In addition, representative cross-sectional view of the density distribution were illustrated in Figure 3.4-C. There are significant amounts of grey elements at convergence, which may indicate local minima. There are very weak connections between large spheres at the corners.

3.3.4 Microstructures with the same porosity but different bulk modulus and diffusivity

A particular strength of the target optimization is the capability to create microstructures of the same porosity, but with a range of bulk modulus and diffusivity. We successfully designed microstructures with 45~50% porositiy (Figure 3.5) that had diffusivities ranging from 16% to 33% and effective bulk moduli ranging from 12% to 24%

of base diffusivity and bulk moduli, respectively. This reflects the algorithms ability to distribute the same amount of material in different layouts to attain dramatically different effective mechanical and mass transport properties. The microstructures in Figure 3.5 can be used to experimentally investigate the sole effect of material distribution on load bearing and mass transport without the confounding variation of changing porosity.

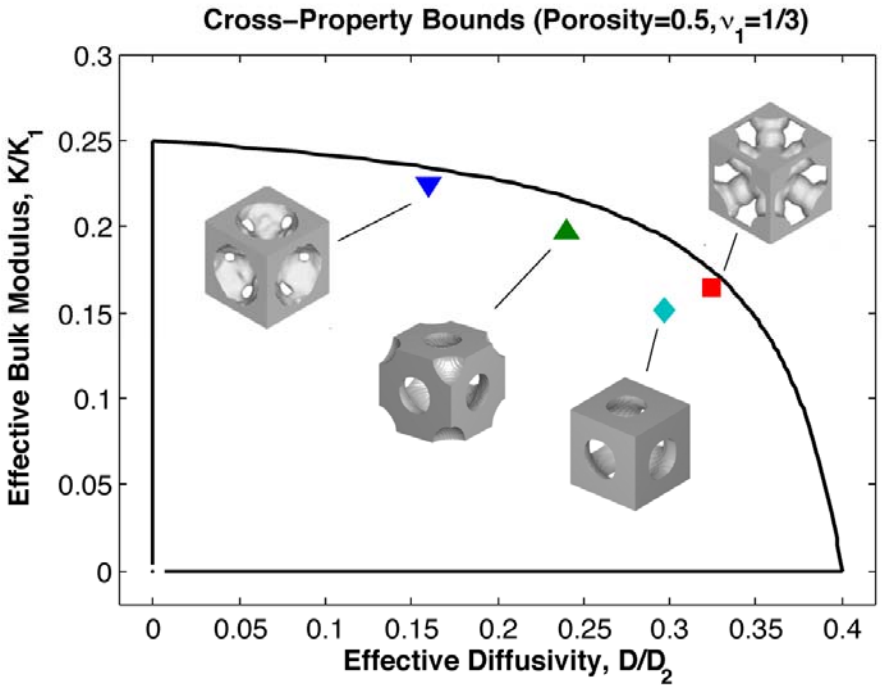

Figure 3.5 Microstructure designs with ranges of diffusivities for 50% porosity

3.3.5 Comparison of Designed Properties with Experimental Measurements

Using SFF technique, the scaffolds were fabricated from PCL and HA mixture for compression tests. Because the scaffold microstructures were represented using voxel elements, a three-dimensional version of pixels, optimal scaffolds could be generated by simply repeated in 3D voxel space using an image based modeling technique. Test specimen dimensions were 8 mm × 8 mm × 16 mm, and unit microstructures were scaled to have a dimension of 2.67mm × 2.67mm × 2.67 mm. This corresponds to 3×3×6 of unit microstructures. The voxel representation of the specimens was converted to STL model for fabrication by SFF technique.

A selective laser sintering technique was utilized to fabricate the specimens by sintering PCL and HA in a powder bed. In Figure 3.6, the specimens (A)~(H) corresponds to microstructures (A)~(H) in Figure 3.1. Compression tests were conducted on these scaffold specimens to be compared with designed mechanical properties. MTS Alliance RT30 electromechanical test frame (MTS Systems Corp., MN) was used with strain rate of 1 mm/min with preload of 1 lb. TestWorks4 software (MTS Systems Corp., MN) was used to collect load-displacement responses. Average stress was obtained from the recorded load divided by the undeformed cross-sectional area of the specimen (~ 64 mm^2). In the similar manner, average strain was calculated from the displacement divided by the undeformed height (~16 mm).

The stress-strain curve is presented in Figure 3.7. The experimental modulus was obtained by the slope of a line that connects the origin and 1% strain point. The moduli obtained by the average stress and strain were compared with designed Young's modulus,

which was calculated from bulk modulus and Poisson's ratio because the optimized microstructures were all cubic symmetric (Table 3.2).

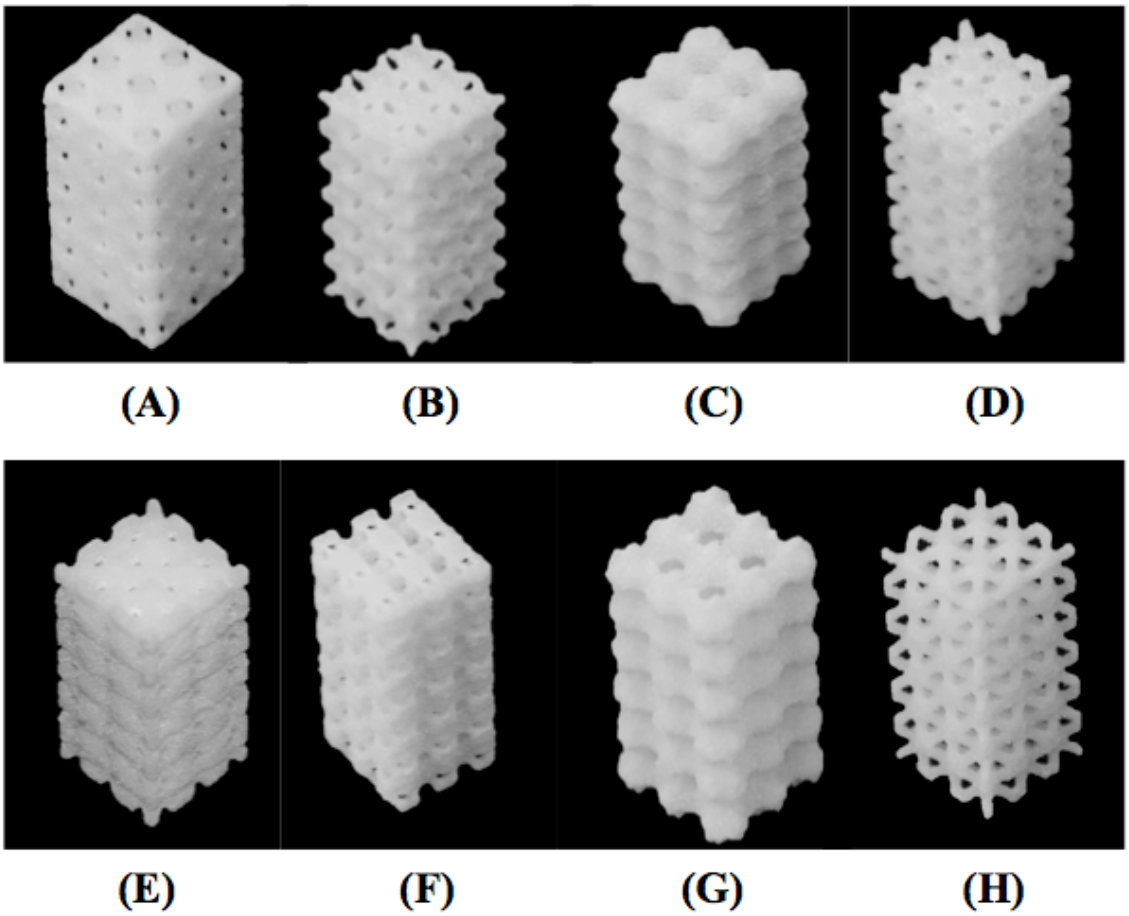

Figure 3.6 Scaffolds with optimal microstructures were designed and fabricated using SFF.

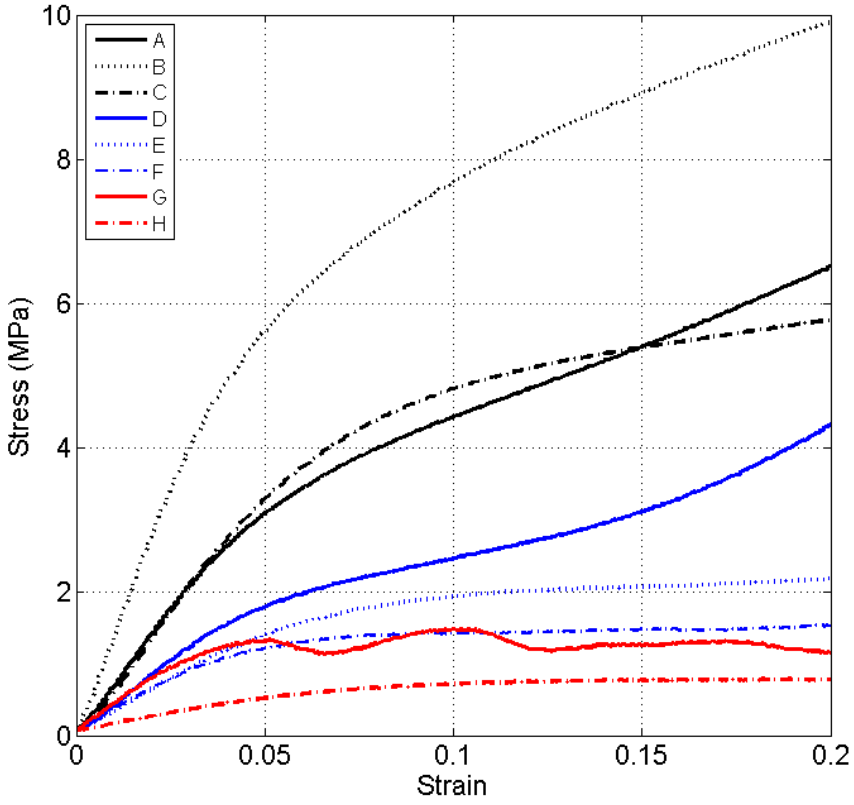

Figure 3.7 Stress-strain curves obtained from compression tests of the fabricated scaffolds designed with the optimal microstructures.

Table 3.2 Comparison of theoretical Young's modulus calculated from the homogenization method, and experimental Young's modulus measured compression tests.

Microstructures	Theoretical Young's Modulus*	Experimental Young's Modulus**
A	0.4875	0.2167
B	0.5273	0.4424
C	0.4277	0.2479
D	0.2258	0.1284
E	0.1955	0.2186
F	0.2251	0.1373
G	0.2442	0.1509
H	0.0973	0.0571

* Values are normalized to the base material Young's modulus.
** Experimental Young's moduli are normalized to experimental Young's moduli of bulk specimen (295MPa).

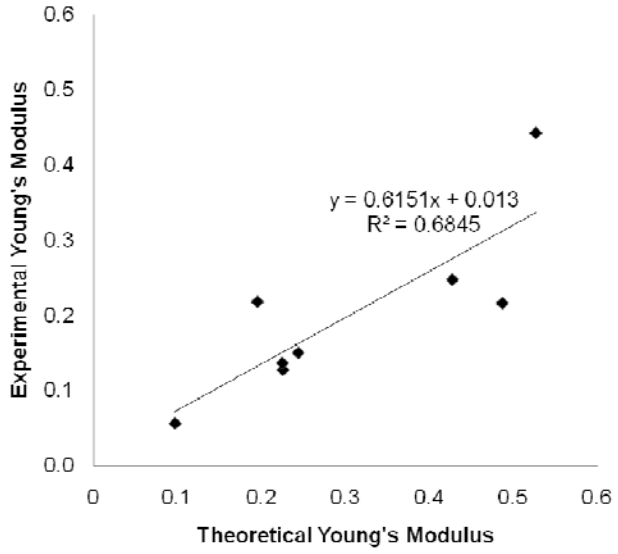

Figure 3.8 Theoretical Young's modulus was correlated to experiments.

As presented in Figure 3.8, the theoretical Young's moduli were correlated to experimental Young's moduli, although the latter being lower than the former. It should be noted that small geometric features such as struts and holes in the microstructures were not accurately fabricated in some cases. For example, disconnected struts were identified between unit microstructures in Figure 3.6-B. In the selective laser sintering process, the laser beam scanning speed and power affect the exposed energy at a spot, which determines the minimum curing path size. Geometric features, smaller than the minimum path size, were skipped based on preset fabrication accuracy of the machine. Considering manufacturing defects, the theoretically designed properties seemed to provide upper bound for the experimentally measured properties.

3.4 Discussion

It is hypothesized that scaffolds should provide mechanical and mass transport properties as close as possible to native tissues to enhance tissue regeneration (Hollister et al. 2009). As an active component, scaffolds should be able to provide a proper mechanical environment so as to maintain structural integrity at the defect site as well as transmit appropriate mechanical stimuli to newly generated tissues (Thomson et al. 1995; Hutmacher 2001; Simmons et al. 2001). In addition, scaffolds should provide appropriate mass transport conditions that can influence cell phenotype, tissue ingrowth, and nutrient conditions (Malda et al. 2004; Hollister et al. 2009). However, it is still unclear what optimal properties the scaffold should provide for the best tissue regeneration. For example, there have been inconsistent suggestions on the optimal pore size or porosities for tissue regeneration. Moreover, different levels of mass transport environment have

been shown to result in differentiation to different cell types and degrees of tissue regeneration (Malda et al. 2003).

In order to rigorously investigate correlations between functional environments and tissue regeneration, the ability to design scaffolds with controlled mechanical and mass transport properties is necessary. In this study, we were able to design microstructures for scaffolds with tailored mechanical and transport properties using topology optimization. Cross-property bounds provide the feasible design space in the bulk modulus and diffusivity plane. Thus, topology optimization combined with cross-property bound can be a very useful design tool for creating microstructures with significant, controlled variations in mechanical and mass transport properties.

To avoid numerical instabilities inherent to the topology optimization, we applied the nonlinear sensitivity filter proposed by Sigmund (Sigmund 1994). Filtering techniques are known to work well to avoid known instabilities such as checkerboard patterns and mesh dependence. The drawback of the filtering technique is that final structure often contains intermediate density values along solid-void boundaries due to the blurring effect of the filter. However, we found in many cases that 0-1 designs were achieved with the nonlinear sensitivity filter. We measured the convergence of the intermediate densities toward 0 or 1 by (3.7).

$$R_{conv} = \frac{1}{N}\sum_{i=1}^{N}\frac{\left|\rho_i - 0.5\right|}{0.5} \tag{3.7}$$

R_{conv} approaches 1 as the intermediate densities are penalized toward either 0 or 1. With the SIMP topology optimization and sensitivity filter, we were able to obtain microstructures with an R_{conv} index over 0.95, which can be considered converged.

If R_{conv} is less than 0.95, the designed properties may shift towards upper cross-property bounds after post processing. From a practical view point, this may be beneficial because the premature solution still serves as a design choice. However, achieving a discrete solution is more desirable in terms of tailoring the material properties and creating a manufacturable design. In this regard, other techniques can be applied such as density filtering with a Heaviside step function (Guest et al. 2004) or addition of a nonlinear diffusion term to the objective function (Wang et al. 2004).

Many microstructure design studies have presented the composite or porous structures that are near or on the cross-property upper bounds (Guest and Prevost 2006; de Kruijf et al. 2007; Challis et al. 2008). In these previous works, two competing properties were maximized simultaneously. However, one of our main interests in this study was to design microstructures whose properties are far from the upper bounds.

Of particular interest in our study was the design of microstructures with low diffusivity and low bulk modulus. As presented in the result section, our design converges to a minimum. More often than not the R_{conv} index was less than 0.8. If we targeted a design point far from the upper cross-property bounds, the R_{conv} index was even smaller. To evaluate the difficulty of achieving this inner design point, we tested three design points: (1) K=0.2 and D=0.3, (2) K=0.15 and D=0.2, and (3) K=0.1 and D=0.15. We used the same problem statement and control parameters for filtering until convergence at a (local) minimum was achieved.

The outer point or the point on the upper bounds was easily achieved with an R_{conv} index of almost 0.99. For the middle design point, the R_{conv} index was 0.93, which means the final design contained a blurry solid-void boundary. However, for the innermost

design point case, the R_{conv} index was 0.71 and the structure exhibited a clear grey layer in addition to the black solid structure. This can be clearly noticed in the histogram plots (Figure 3.9) in which the number of elements having a given density are plotted in bins. The inner design point case had a large amount of elements containing density values of around 0.3~0.4. One explanation is that the presence of grey regions represents sub-microstructures that give more degrees of freedom in reaching the interior targets than can be reached using pure 0-1 designs. This is actually seen in the hierarchical structure of biologic tissues, which have feature sizes ranging from the nanometer to centimeter scale.

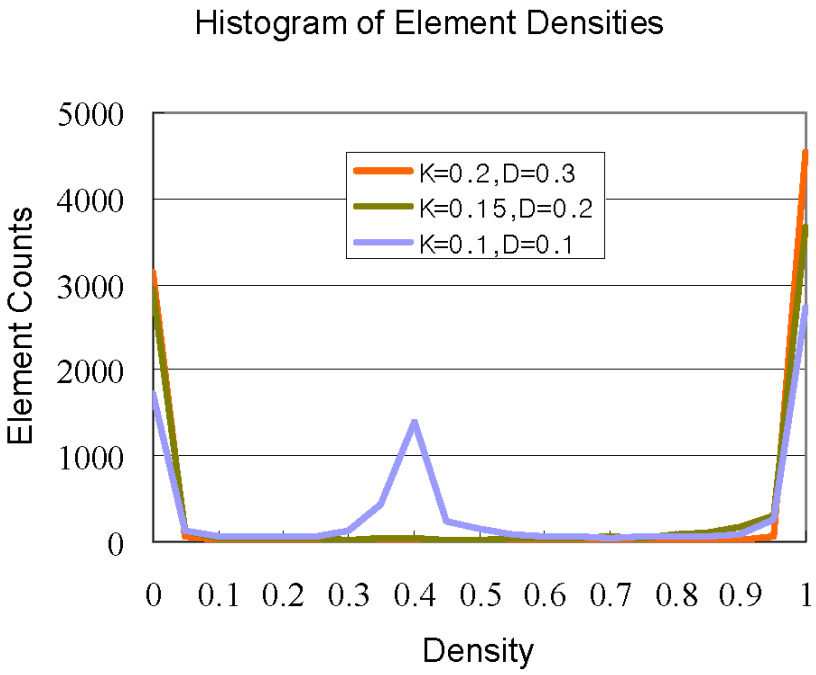

Figure 3.9 Histograms of densities of three microstructure designs targeting K = 0.2 and D = 0.3, K = 0.15 and D = 0.2, and K = 0.1 and D = 0.1

Another important factor is the consideration of the manufacturability. Particularly for the low diffusivity designs, small holes develop to limit diffusivity. Considering the size of unit cells (typically around 1 mm) in the skeletal tissue scaffolds, the small holes may not be manufactured due to the limited fabrication resolutions. As for the optimization problem, it would be interesting to control the member size as well as hole size as manufacturing control factors.

In our study, diffusivity was considered in this scaffold design because diffusion characteristics of the scaffold can govern overall cell migration and tissue regeneration as well as oxygen and nutrient delivery and metabolic waste removal. Thus, mathematical models of cell migration and tissue regeneration have adapted diffusion like equations (Anderson and Chaplain 1998; Adachi et al. 2006). In addition, diffusivity and permeability of scaffolds are well correlated (Hollister et al. 2008). Moreover, there are known cross-property bounds on the effective diffusivity and bulk modulus, which can suggest feasible design characteristics.

As a temporary substitute for extracellular matrix, the scaffolds should provide tissue specific functional environments during new tissue formation. However, there is still little experimental data available regarding optimal effective scaffold properties for tissue regeneration. Moreover, conflicting findings have been reported regarding the effect of oxygen diffusion on cartilage regeneration, demonstrating the need for testing scaffolds with a range of designed properties (Malda et al. 2004). In this regard, the microstructural topology optimization method, which is able to produce scaffolds with a range of designed properties, will provide more opportunities to investigate relevant scaffold properties.

CHAPTER 4

POROUS BIODEGRADABLE INTERBODY FUSION CAGE DESIGN USING THE INTEGRATED GLOBAL-LOCAL TOPOLOGY OPTIMIZATION

4.1 Overview

Spinal fusion is a treatment option for degenerative spinal conditions when conservative treatments fail. In 2001, 357,000 patients underwent lumbar spinal surgery in the US alone, of which over 122,000 were lumbar spinal fusions for degenerative disc conditions (Deyo et al. 2005). Interbody cages provide stability and limit motion at the bone graft site as well as allow immediate restoration of disc height and neuroforaminal volume, thus enhancing fusion rate and effectively relieving pressure and pain (McAfee 1999; Chen et al. 2010). Conventional metallic cages, packed with bone graft or bone morphogenetic protein, result in good radiographic fusion rates (> 90%) and improved clinical outcomes (Kuslich et al. 1998; Whitecloud et al. 1998).

The current metallic cages, however, are associated with excessive rigidity that may increase postoperative complications such as stress shielding, device related osteopenia, and subsidence (Smith et al. 1991; Kanayama et al. 2000). Although having superior mechanical stiffness and strength, metallic cages often fail to effectively transfer loads to stimulate bony tissue remodeling (Kanayama et al. 2000; van Dijk et al. 2002).

Radiopaque metallic cages also interfere with visualization of bony fusion at the graft site during postoperative follow up (Cizek and Boyd 2000; Robertson et al. 2009), making it difficult to determine the progress of bony healing. Furthermore, it has been reported that titanium particulate debris can cause an inflammatory reaction in surrounding soft tissues (Cunningham et al. 2003).

Biodegradable/bioabsorbable fusion cages made of polylactide copolymers have gained increasing attention because of their primary advantage over nondegradable material, namely that the material disappears over time, being replaced with newly grown tissue (van Dijk et al. 2002; van Dijk et al. 2005). The material properties of bioresorbable materials are closer to vertebrae trabecular bone, thereby distributing the load more evenly to the ingrown bone and the device (van Dijk et al. 2002).

In spite of these beneficial aspects, the use of biodegradable cages for lumbar interbody fusion is rare due to significantly lower stiffness compared to metallic or non-degradable polymeric cages. Although the degradability is a desirable feature of orthopedic implants for bone healing, it is critical that reduction in material properties due to degradation be timed to coincide with increase in mechanical stability resulting from bone growth. The time dependent change (decrease) of mechanical properties has been correlated to higher load frequency, higher temperature, and higher humidity, possibly explaining early device failure of biodegradable cages in a clinical study (Smit et al. 2008).

In an effort to address the intrinsic disadvantages of bioresorbable materials, several biodegradable cages were investigated in pre-clinical animal models, demonstrating good outcomes (van Dijk et al. 2002; Kandziora et al. 2004; Smit et al.

2006). However, concerns of early device failure were again raised with too rapid *in vivo* degradation being the suspected reason. In these studies, conventional designs (Weiner and Fraser 1998) including hollowed cylinders with threads, open boxes, and vertical rings, were used for biodegradable cages. Mere exchange of permanent materials for biodegradable polymers in conventional designs like hollow cylinders or open boxes may not provide sufficient strength for lumbar fusion.

A hierarchical scaffold tissue engineering strategy(Hollister 2005) with topology optimization may overcome these hurdles in the design of biodegradable fusion cages, with the capability of controlling the functional properties by designed microstructures. Based on this concept Lin et al. applied integrated global-local topology optimization to design porous titanium fusion cages that provide sufficient but not excessive strength and effectively transmit strain energy to the regenerate bone.(Lin et al. 2004) Topology optimization distributes a limited amount of material within a predefined design domain under specific loading conditions to achieve desired mechanical stiffness. Lin et al. further tested the efficacy of the optimized cages made of titanium.(Lin et al. 2007) It should be noted that the goal of these previous studies were reducing stiffness to avoid complications associated with excessive rigidity. However, biodegradable cages, with less stiffness, already satisfy the previous design goal. The design target should address the problem related to weaker material properties.

Thus, the goal of our study was to design, fabricate, and test biodegradable PCL cages which are mechanically strong enough to support loads, have sufficient pore space for delivery of biologics and bone ingrowth, and can transfer loads seamlessly from the designed cage to newly grown bone tissue. We assumed that a globally optimum

structure maximizes the overall stiffness of the fusion cage and locally optimized microstructures maximize the transport characteristics of the fusion cage.

4.2 Fusion Cage Design by Integrated Global-Local Topology Optimization

Integrated global-local topology optimization was utilized in order to balance the mechanical stability and mass transport properties of the porous biodegradable fusion cage. The global topology optimization was used to obtain an optimal material density distribution that maximizes the stiffness of the fusion cage, while the microstructural topology optimization allowed maximal fluid permeability (correlated with high pore interconnectivity) of the porous fusion case for a given material density map. For design validation, the porous fusion cage was built using a solid freeform fabrication technique of laser-sintering PCL powders mixed with HA. Then, compression tests and finite element analyses were conducted to determine yield loads of the fabricated cage relative to in vivo lumbar spine loads

4.2.1 Finite Element Modeling for the Global Topology Optimization

The global topology optimization determines optimal material density distribution, or material density map, which maximizes the stiffness of the fusion cage with constrained volume fraction to preserve sufficient porosity for bony fusion. Topology optimization, in general, is executed within finite elements which are assigned with a density value representing the structural topology. The density values can have 0 or 1: 0 indicates no material or void and 1 indicates a solid. It is well known that this discrete 0 or 1 optimization problem is ill-posed and lacks solution.(Sigmund and Petersson 1998) Relaxation of the original 0-1 problem by introducing a continuous variable ranging from

0 to 1 enables the problem to be solved using conventional mathematical programming methods. However, this often allows the intermediate density values in the optimization result so that post processing techniques are required to determine the final structural topology. In our study, the density distribution was segmented into several regions, which served as a map (Hollister et al. 2000; Hollister et al. 2002) to place specific microstructures within the lumbar fusion design space.

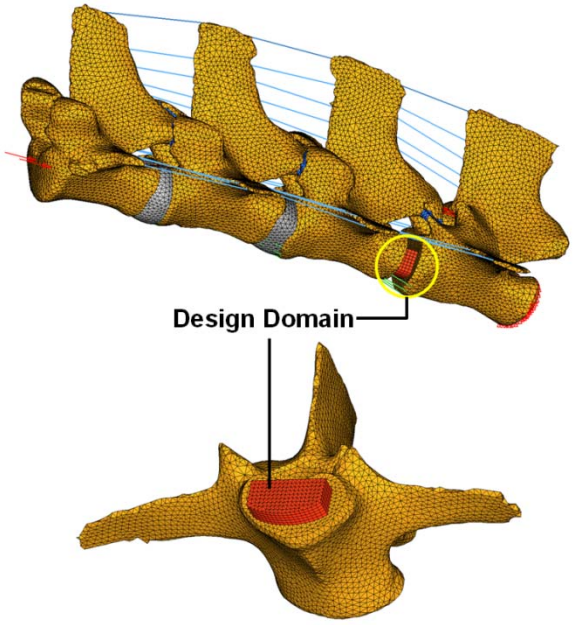

Figure 4.1 Ligamentous finite element models of minipig lumbar spine segments (L2~L5) and the design domain for the global topology optimization at L4-L5 level.

Table 4.1 Mechanical Properties of Components of the Finite Element Models

Components	Young's Modulus (MPa)	Poisson's Ratio	Cross-sectional Area (mm^2)
Cortical bone	12,000	0.3	-
Cancellous bone	100	0.2	-
Equivalent Disc	5	0.4	-
Facet joints	5	0.4	-
Ligaments (rod elements)			
ALL	20		63.7
PLL	20		20
ITL	58.7		4
ISL	11.6		40
SSL	15		30
Poly(ε-caprolactone)	300	0.3	-

For the global topology optimization, the finite elements were modeled based on the CT images from a Yucatan minipig (Figure 4.1). CT images for lumbar spine motion units from L2 through L5 were segmented into a 3D geometric representation (STL format) using Simpleware ScanIP software (Simpleware Ltd., Exeter, UK). The STL files were smoothed and converted to a geometric representation (IGES format) (RapidForm, Inus Technology, Inc., Seoul, Korea), which allowed easy modeling of additional soft tissues such as intervertebral discs and facet joints using a commercial solid modeling software, Unigraphics NX (Siemens PLM Software, Plano, Texas). The finite elements of vertebral bodies were modeled as cortical shells (shell elements) and cancellous bones (tetrahedral elements). Then, tetrahedral meshes for facet joints were added to fill the gap between the superior and inferior articular facets. Rod elements were used to model

spinal ligaments, such as anterior longitudinal ligaments, posterior longitudinal ligaments, intertransverse ligaments, interspinous ligaments and supraspinous ligaments. The design domain for global material density map was defined at L4-L5 level intervertebral disc space (Figure 4.1).

Material properties for the minipig lumbar spine motion segments were adapted from previous FE studies found in literature (Shiraziadl et al. 1986; Lin et al. 2004; Zhong et al. 2006) and assumed to be those of humans (Table 4.1). For PCL, the modulus was obtained from the compression test of fabricated solid cylinders and Poisson's ratio was assumed to be 0.3. We applied 5 Nm of flexion, extension, lateral bending and torsion with 115N of pre-compression to simulate the physiological loading condition. Especially, the pre-compression load was determined such that the resultant stress level in the intervertebral disc model matches the experimentally measured pressure.(Ekstrom et al. 2004)

To achieve the global density map in physiological loading conditions, the objective function to be minimized was evaluated as a weighted sum of the compliances at different loading modes: flexion, extension, lateral bending and torsion. Because biodegradable scaffolds with 50% porosity were successfully demonstrated for bone regeneration in our group (Lin et al. 2005; Schek et al. 2005), the volume fraction of the final fusion cage was constrained less than 50%, which also ensures the minimum 50% porosity for sufficient bone ingrowth. As a manufacturing constraint, structural member size was constrained between 1.6 mm and 3.5 mm. Symmetric constraints were also applied to the sagittal plane for non-symmetric loading (lateral bending). The

optimization was performed using OptiStruct, a commercial topology optimization solver (HyperWorks OptiStruct, Altair Engineering, Troy, MI).

4.2.2 Microstructure Design using Local Topology Optimization

Local topology optimization produces optimal microstructures that achieve prescribed effective mechanical and mass transport properties of the global structure (Kang et al. 2010). Assuming that a global structure consists of repeated porous microstructures and the size of the microstructure is small enough compared to the size of the global structure, the averaged property can be evaluated by the method of homogenization (Sanchez-Palencia et al. 1987). The homogenization method determines the averaged properties of the global structure from an analysis of a representative microstructure of a porous media or composite material assuming periodicity. The analysis responses at the local length scale are averaged to give the effective properties at global scale. Based on homogenization theory, the local topology optimization can find microstructural topology that has average properties the global structure matched with prescribed properties. In each optimization step, the algorithm evaluates current average properties by the homogenization method and updates element density in the microstructural domain to minimize the difference between the obtained and prescribed properties.

A microstructure can be considered optimal if it's the resulting effective property it generates is close to a theoretical bound. There are known theoretical bounds on the effective properties of porous material. The bounds limit the maximally achievable property for given material volume fraction, or equivalent porosity. In the case of two

properties which are competing, cross-property bounds limit the maximally achievable property pairs (Gibiansky and Torquato 1996).

Based on the optimality within the cross-property bounds, two different methods were utilized in designing microstructures: the first one with primitive geometries and the second one with the local topology optimization. The first approach has an advantage over the second one in that it can easily integrate geometries of local and global structures including fixation geometry and a bullet-shaped tip. On the other hand, the advantage of local topology optimization is that based on the desired properties, it can automatically generate optimal microstructures.

For the microstructures with primitive geometries, three orthogonal cylindrical holes were modeled, and the geometric features were adjusted to match a prescribed porosity. The mechanical and mass transport properties were then evaluated with the homogenization method and the optimality was checked within the cross-property bounds. For the microstructures with the local topology optimization, the target properties were identified on the upper cross-property bounds and the algorithm then designed the optimal microstructures.

4.2.3 Fusion Cage Design for an in situ large animal model

The global density map obtained from the global topology optimization gives a material volume fraction distribution between 0 and 1, not a prescribed architecture. We then replace the global density map with several representative microstructures with different porosities according to regional density levels. The global density map was segmented into high density and low density regions. Low bulk modulus microstructure was used to replace the low density region and high bulk modulus microstructure was

used for the high density region. The threshold density value was determined such that the overall porosity of the global design domain matched 50%. Finally, the outer wall was designed to add more stability to the fusion cage. Detailed geometric features were added such as a bullet-shaped tip for easy insertion of the fusion cage and fixation geometries such as teeth for increasing pull out friction.

For the integration of the geometry-based approach, Boolean operations were conducted among different microstructures using Unigraphcs NX. On the other hand, for the integration of the optimal microstructures, an image based modeling technique was utilized. The optimal microstructures were obtained by local topology optimization performed on voxel meshes. The resultant microstructures were also represented in voxels. The outer wall with detailed features was voxelized using Voxelcon (Quint, Tokyo, Japan). The integration of global and local structures can then be done by replacing corresponding voxel element values. The final integrated fusion cage design in voxel representation can be easily converted to STL format to be built using solid freeform fabrication techniques.

4.2.4 Fabrication and Testing:

To validate the mechanical stiffness and strength of our optimal fusion cages, compression tests were conducted on manufactured fusion cages. The final designs were fabricated using a Formiga P100, a selective laser sintering (SLS) solid freeform fabrication (SFF) machine (EOS GmbH - Electro Optical Systems, Germany). Poly(ε-caprolactone) (PCL) powders mixed with a small volume of hydroxyapatite (HA) were used for the layer by layer laser sintering of our designs. For comparison, a conventional TLIF cage was reverse-engineered using micro-CT scan. Then, the conventional design

was also fabricated with the same material, PCL/HA mixture. The two optimized cages and the conventional TLIF cage were mechanically tested using an MTS test machine (MTS Systems Corp., MN) (1 mm/min with preload of 1 lb). The load-displacement responses were compared among the optimal and conventional designs. It should be noted that the optimal designs were scaled to match the height of the conventional TLIF design. Solid cylindrical specimens (8mm in diameter and 16mm in height) were also fabricated and mechanically tested to measure Young's modulus and yield stress of the sintered bulk PCL/HA mixture. The Young's modulus was defined as the slope of the linear region of stress-strain curve and the yield stress was measured from the intersection of the 0.2% offset of the linear slope and the original stress-strain curve.

To further validate the load supporting capacities of the optimal fusion cages and predict yield of the cages, image based finite element analyses were conducted. The optimal designs without detailed geometric features were converted to voxel elements in Voxelcon. Compression loads of 1500N, which is generally accepted as load level at human low back with moderate activity (Nachemson 1966), were applied on the top of the cages and the bottom was constrained. To investigate how the stress levels changed after initial bony fusion inside the optimal cages, additional models were prepared by filling pore space with cancellous bone.

In order to estimate the yield of the porous fusion cages, we applied the Weibull function fitting method to the cumulative histogram of von Mises stress distribution. Saitou et al. have developed a systemic method to estimate the yield of porous scaffolds by interpolating the fitted Weibull function to cumulative histogram of von Mises stresses

based on experimentally measured yield stress of bulk specimen (Saito et al. 2010). The modified cumulative Weibull function was defined as

$$f(\sigma) = 1 - \left(p \exp(-(\sigma/\lambda)^{k_1}) + (1-p)\exp(-(\sigma/r\lambda)^{k_2}) \right) \quad (4.1)$$

where σ is von Mises stress, p is weighting factor, k_1 and k_2 are shape parameters, λ and r are scale parameters. In general, p, r, k_1 and k_2 are constants for the same case, thus leaving λ proportional to the applied load level. The assumption in this method is that, at yield stress (σ_y), the modified Weibull function has $1-\varepsilon$, with small ε. Then, λ_y can be calculated from the equation

$$1 - \left(p \exp(-(\sigma_y/\lambda_y)^{k_1}) + (1-p)\exp(-(\sigma_y/r\lambda_y)^{k_2}) \right) = 1-\varepsilon \quad (4.2)$$

Once at least two cumulative functions under two loading cases are obtained, we know λ_1, λ_2 and λ_y and the applied loads, say F_1 and F_2. The load level at yield, F_y can then be interpolated. The small parameter, ε, represents the portion of number of voxels that is allowed to be over experimental yield stress, and can be determined by the compression tests. In order to use the Weibull fitting method, the image based finite element analyses were conducted on the optimal cage models under 1000N, 2000N, and 3000N. Then, the loads at yield were estimated for our optimal fusion cages.

4.3 Results

Our results demonstrated that the integrated global-local topology optimization scheme was successfully applied to the design of porous fusion cages. SFF technique demonstrated the feasibility of manufacturing porous fusion cages, whereas the mechanical tests and validation simulations confirmed that the optimized fusion cages had yield loads 3x typical human lumbar spinal loads.

4.3.1 Global Density Map and Local Microstructures

To design a mechanically stable porous fusion cage, we obtained an optimal material density distribution with maximum stiffness at 50% porosity (Figure 4.2). High density regions were properly located to support the applied loadings, i.e. flexion (Figure 4.2-A), extension (Figure 4.2-B), lateral bending (Figure 4.2-C) and torsion (Figure 4.2-D). In addition, the combination of all the loadings resulted in the summation of all high density regions (Figure 4.2-E). For the combination of all the loading modes, equal weighting factors were assigned to all the loading cases in this study. It should be noted that the different weighting factors for each loading mode will produce different global density distributions. For instance, if one loading mode, say flexion, is dominant over the other modes, a global density map similar to one in Figure 4.2-A will be obtained. The global density map was segmented into high density and low density regions with a threshold density value of 0.5. Figure 4.3 illustrates segmentations of the global density map under flexion (Figure 4.3-A), extension (Figure 4.3-B), lateral bending (Figure 4.3-C), torsion (Figure 4.3-D), the combination of all the loadings (Figure 4.3-E) was chosen in this study to implement optimal pore architectures.

The diffusivity or permeability of the porous fusion cage was maximized by designing porous architectures using local topology optimization using the global volume fraction as a constraint. The optimally designed microstructures were then substituted into appropriate locations within the global density map. The close proximity of the microstructure properties to the cross-property upper bounds indicates that the mechanical and mass transport properties of the microstructures are optimal (Figure 4.4).

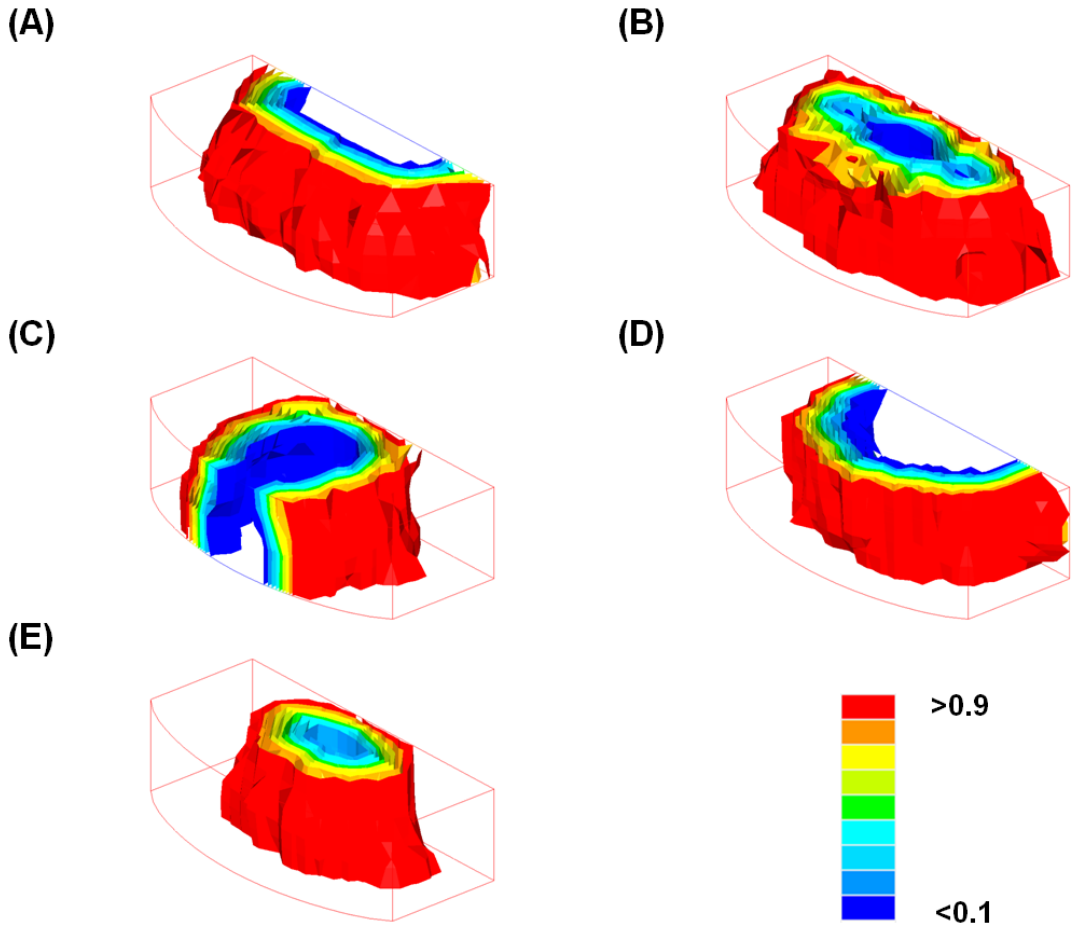

Figure 4.2. Global density maps obtained using the global topology optimization, under (A) flexion, (B) extension, (C) lateral bending and (D) torsion. (E) represents the combination of all loading modes used for the final integrated design.

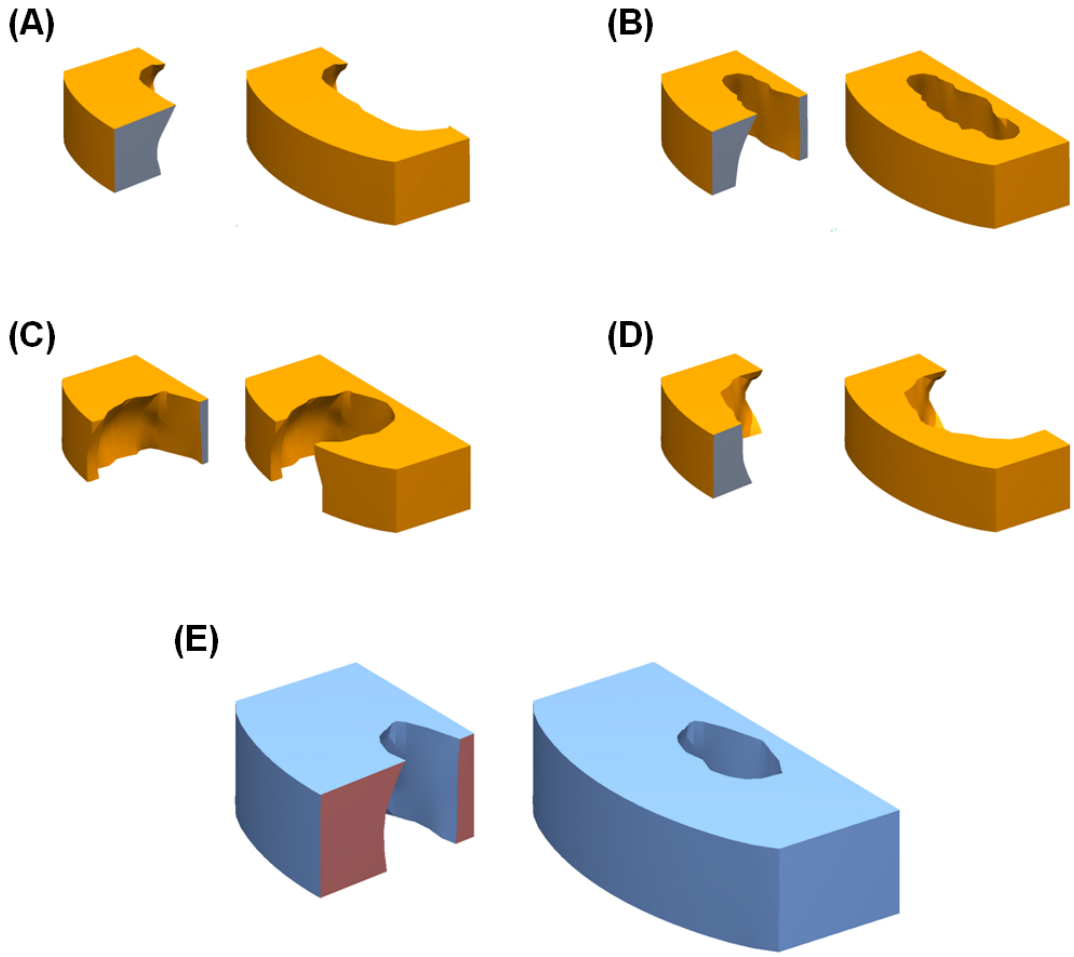

Figure 4.3 Segmented global density maps, under (A) flexion, (B) extension, (C) lateral bending and (D) torsion. (E) represents the combination of all loading modes used for the final integrated design.

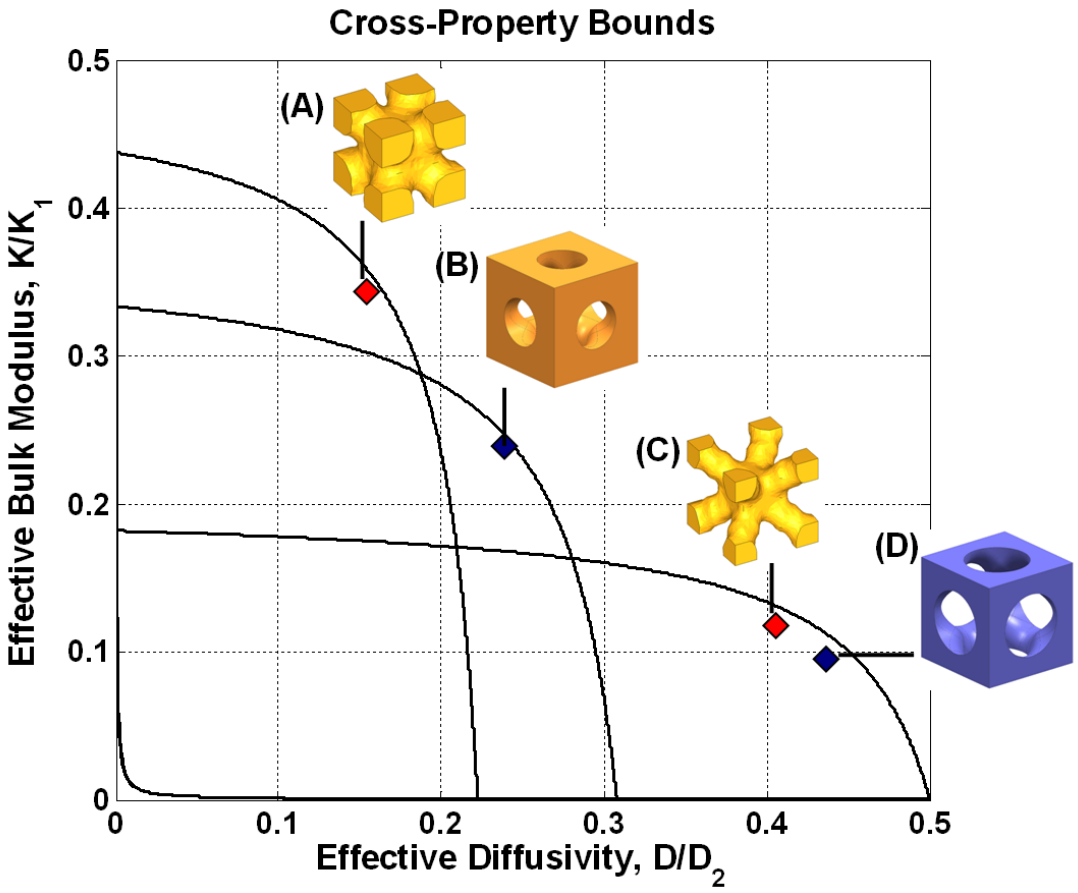

Figure 4.4. All the property pairs of the microstructures are on the cross-property upper bounds, which indicates the microstructures are optimal. (A) and (C) were designed using the microstructural topology optimization and (B) and (D) were designed using primitive pore geometry (cylindrical holes).

Table 4.2 Mechanical and mass transport properties of the microstructures used in the design of porous fusion cages.

Microstructures in Figure 4	Normalized Effective Bulk Modulus (%)	Normalized Effective Young's Modulus (%)	Normalized Effective Diffusivity (%)
(A)	33.2	42.8	16.2
(B)	22.4	38.9	24.5
(C)	11.1	9.7	41.6
(D)	9.3	20.2	44.8

For the microstructures with cylindrical pores, the high bulk modulus microstructure (Figure 4.4-B) showed 22.4% of the base material bulk modulus whereas the low bulk modulus microstructure (Figure 4.4-D) showed 9.3% of the base material bulk modulus. Likewise, for the optimized microstructures, the high bulk modulus microstructure (Figure 4.4-A) showed 33.2% of the base material bulk modulus whereas the low bulk modulus microstructure (Figure 4.4-C) showed 11.1% of the base material bulk modulus. The optimized microstructures exhibited more mechanical stiffness but less diffusivity than the cylindrical pores. (Table 4.2)

Table 4.3 Stiffness and yield loads of two designed cages with and without microstructures were compared with those of conventional TLIF cage and PLLA cages in reference (van Dijk et al. 2003).

	Stiffness (N/mm)	0.2% Yield Load (N)
Cylindrical Pore Cage	7117.9	3376.2
Optimal Pore Cage	7548.6	2923.5
Cage Wall Only	5228.1	1947.4
Conventional TLIF	2455.4	1248.5
PLLA Cage	4000*	3500*

* These are average values of stiffness and yield load taken from (van Dijk et al. 2003).

4.3.2 Integrated Design

By integrating the global density map and local microstructures, we successfully designed optimal porous fusion cages with maximum stiffness and permeability. The segmentation of the global density map for the combination of flexion, extension, lateral bending and torsion (Figure 4.3-E) was chosen for the integrated fusion cage design as a representative example. To guaranty overall stability of the fusion cage, we surrounded the porous structure with a 'solid wall'. To do this, we defined the periphery of the design domain as pure solid, inside of which was replaced with microstructures. The high density region (rendered region in Figure 4.3-E) was replaced with high bulk modulus microstructures and the low density region (empty region in Figure 4.3-E) was replaced with load bulk modulus microstructures. For fixation, a saw tooth geometry was added to the top and bottom of the outer wall. For easy insertion of the fusion cage, a bullet-shaped tip was modeled to one lateral solid region whereas the other lateral solid region was

reserved for the surgical tool connection. The integrated porous structure and final fusion cage design are illustrated in Figure 4.5.

4.3.3 Fabrication and Mechanical Test

Using a SFF technique with a PCL/HA mixture, we successfully fabricated prototypes of the optimal porous fusion cages with all the complex pore geometries and detailed features outlined above (Figure 4.6-A). It should be noted that the current design and fabrication methods are flexible such that the cage designs were easily customized to different species. For example, the smaller cage in Figure 4.6-B was scaled to fit in the intervertebral disc space of a domestic pig lumbar spine (Figure 4.6-C). In addition, we scaled the optimal cages by 1.5 to meet the human scale, for which the conventional TLIF cage was designed (the larger cage in Figure 4.6-B). In this way, a fair comparison of the mechanical strengths could be possible between optimized porous designs and conventional TLIF design.

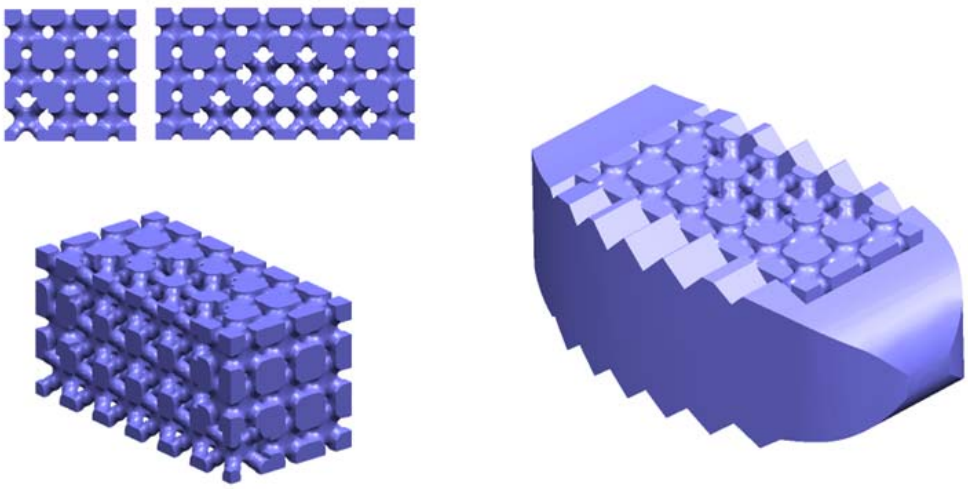

Figure 4.5 Final integrated design of the porous fusion cage. (A) Top, side, and isometric views of the optimized pore architecture, and (B) final integrated design with detailed geometric features.

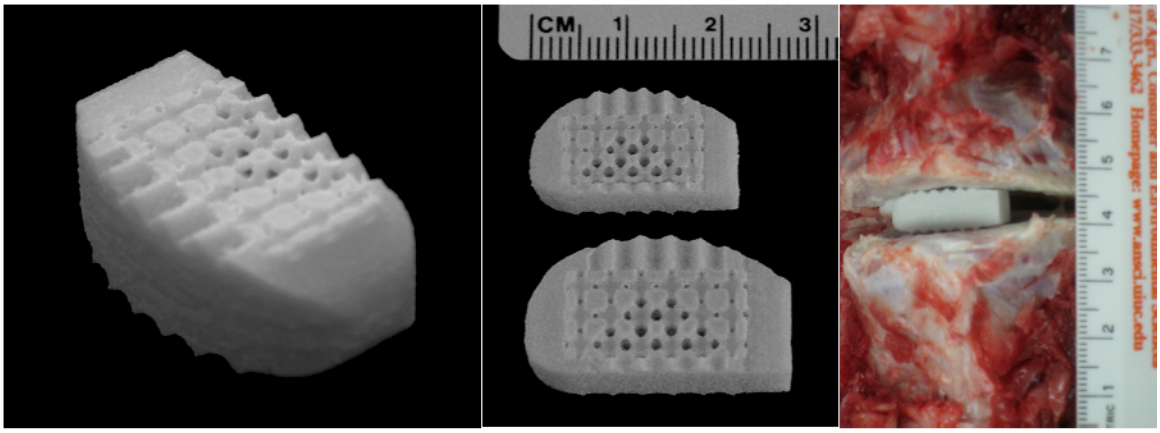

Figure 4.6 (A) A prototype fabricated using SFF and (B) prototypes scaled to fit the minipig (upper) and human(lower) intervetebral disc spaces. (C) The customized cage was checked in the domestic pig lumbar intervertebral disc space.

The compression tests, conducted on the prototypes without detailed saw tooth geometry (Figure 4.7), clearly showed that our optimal fusion cages are stronger than the biodegradable TLIF design (Figure 4.8). The stiffness of the porous fusion cage with optimized microstructures was 7548.6 N/mm and that of the porous fusion cage with cylindrical microstructures was 7117.9 N/mm, while the stiffness of the biodegradable TLIF design was 2455.4 N/mm. Based on 0.2% offset yield stress, the yield was 3376 N (0.667 mm compression displacement) for cylindrical pore fusion cage and 2923 N (0.588 mm compression displacement) for optimal pore fusion cage. The yield of the biodegradable TLIF cage was 1248 N (0.618 mm compression displacement), which was less than that of our cage without pore structures (1947 N at 0.584 mm compression displacement).

Solid cylinders (8 mm diameter and 16 mm height) were fabricated to determine the bulk compressive modulus and yield stress of the sintered PCL/HA mixture (Figure 4.9). The Young's modulus was 295.3±13.6 MPa and yield stress was 10.4±0.2 MPa (n=10).

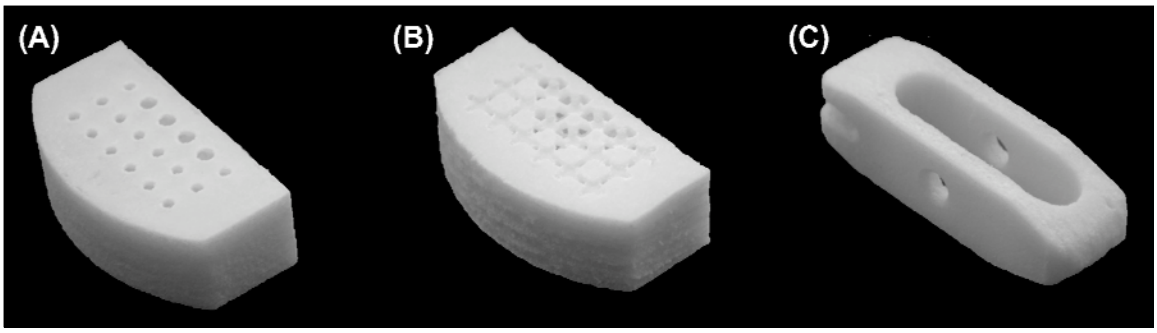

Figure 4.7. For compression tests, the the fusion cages (A) with cylindrical pore microstructures and (B) with optimized microstructures, and the conventional TLIF cage were fabricated without detailed features to eliminate the initial yield caused by the teeth-like geometric features.

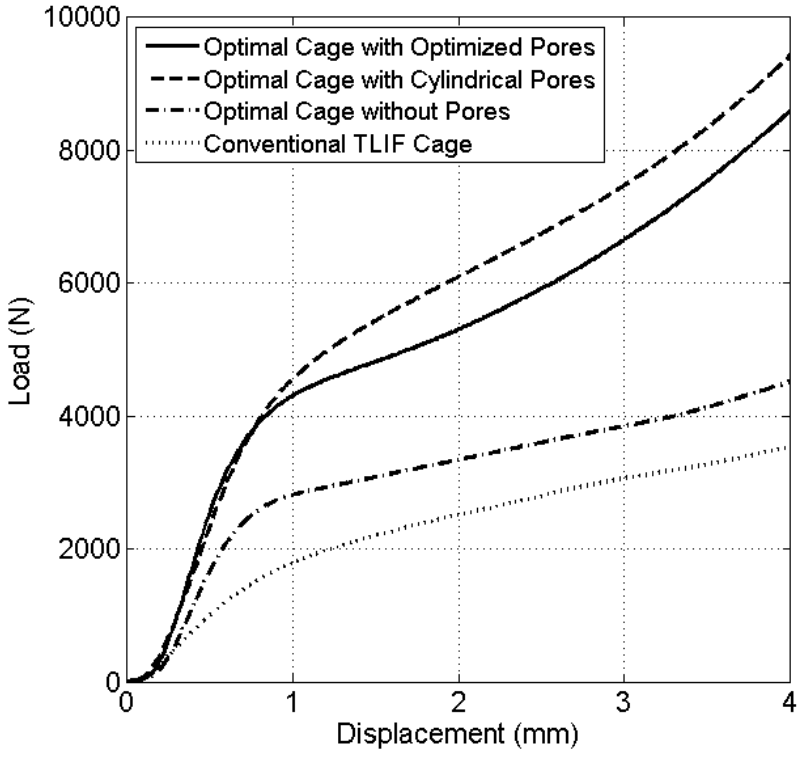

Figure 4.8 Compression test results confirmed that the superior stiffness and strength of the optimized designs over the conventional TLIF design.

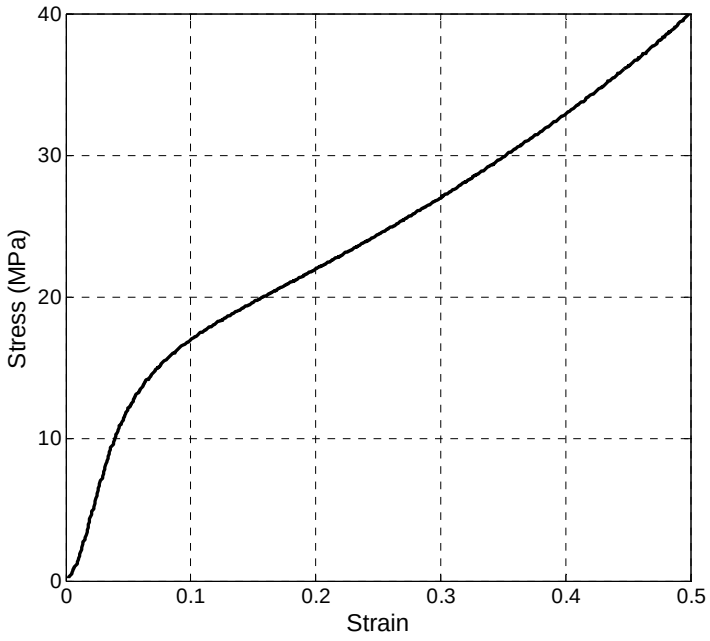

Figure 4.9 Stress-strain curve obtained from the compression test of a bulk cylindrical specimen to determine the Young's modulus and yield stress for the finite element analysis.

4.3.4 Estimation of Yield from the Stress Analysis

Finite element analyses confirmed that porous PCL cages can support physiological loading. We designed our porous cage with thick wall structure surrounding inner pore architecture. To check the load carrying capacity, we first conducted the FE analysis on the wall structure. The maximum von Mises stress was 8.23 MPa under 1500N of compressive force (Figure 4.10-(A)), which is below the experimentally measured yield stress (10.4 MPa) for sintered bulk PCL/HA specimen. However, introduction of microstructures raised the local stress levels over the yield at the thin structural features (Figure 4.10-(B) and (C)). Based on the observation of compression tests (Table 4.3), however, the yield of the global structure was over 3000N, indicating surrounding wall supported the load over local yield load. When assuming initial bony fusion, the local stresses at the pores reduced to 9.34 and 8.6 MPa, which is below yield again (Figure 4.10-(D) and (E)). This demonstrated load transfer from the fusion cage to new generate bone.

Predicted yield load of our optimal fusion cages was 1403 N for cylindrical pore fusion cage and 1723 N for optimized pore fusion cage, from the interpolation of fitted Weibull functions of two loading cages. The cumulative histogram of the von Mises stresses and corresponding Weibull functions were presented in Figure 4.11. The allowed portion of voxels that undergo local yield (10.4MPa) was 1% in this case. In other words, the global porous structure is assumed to withstand the maximum load while 1% of voxels showing von Mises stress over the experimentally measured yield stress. Although there were significant differences in the theoretical prediction and experimental

measurements, the computational yield predictions provided a lower, conservative bound on the actual experimental yield load.

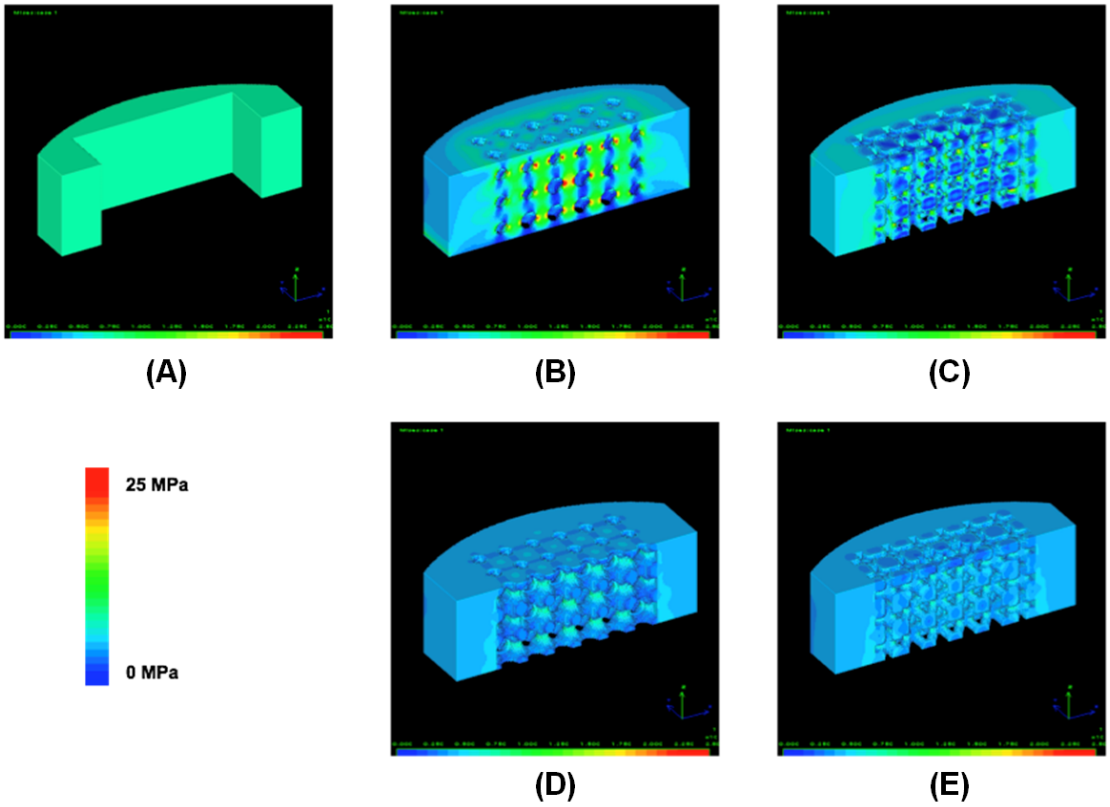

Figure 4.10 (A) Von Mises stress level for optimal fusion cage without pore structures is below the yield stress (8.5 MPa). With initial pore structures (B) and (C), the stress level increased over the yield compared to (A). However, after initial bony fusion inside the pores (D) and (E), the stress level decreased below the yield (9 MPa). These results indicate that major loading support is provided by outer wall. Although local yield at the microstructures increases initially, ingrown bone will take over the loads from the fusion cage, alleviating the load burden at the microstructures.

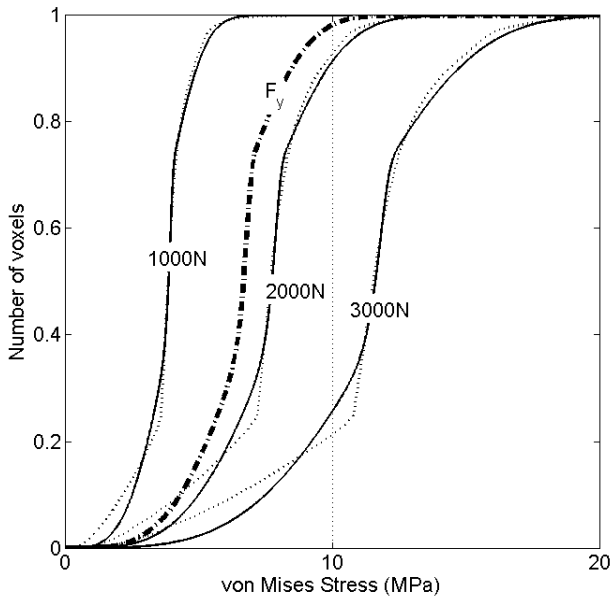

(A)

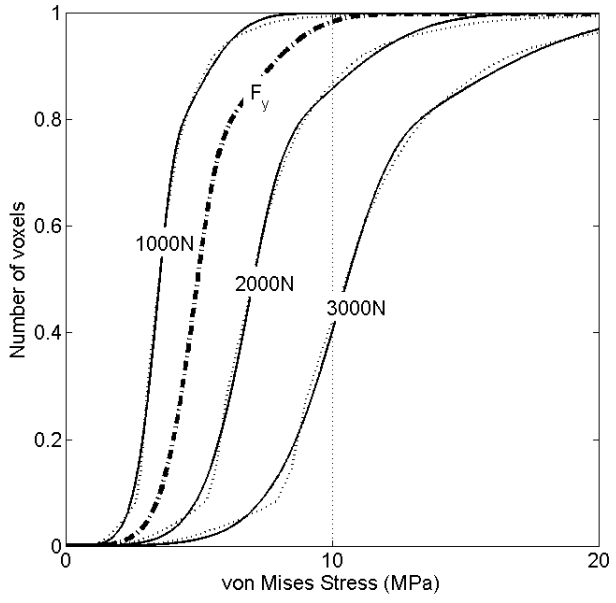

(B)

Figure 4.11 Cummulative histogram of von Mises stress distribution (dotted curves) and Weibull fittings (solid curves) over the entire voxels under different compressive loads. Computationally predicted maximum load was (A) Fy=1403 N for fusion cage with cylindrical pores and (B) Fy=1724 N for fusion cage with optimal pores.

4.4 Discussion

Biodegradable cages have received considerable attention as an interbody fusion system. The underlying rationale is that reduced stiffness adjacent to bone may eliminate stress shielding and that complete resorption of the cage can avoid adverse foreign body reactions. Conventional hollowed cylindrical cages or vertical ring types, however, may not be adequate as a candidate design for biodegradable cages. The thin wall geometry originally designed for metallic cages may collapse under physiological loading condition when simply replacing permanent materials like titanium or PEEK with significantly less stiff biodegradable polymers. A global-local topology optimization approach combined with SFF fabrication technique may overcome this intrinsic difficulty in the design of the biodegradable load bearing implants.

In this regard, the integrated global and local topology optimization was demonstrated in the design of PCL cages that achieve these generally desired stiffness and strength characteristics needed for better fusion outcomes. Furthermore, this design approach is highly flexible so as to be readily applied to either pre-clinical animal models or human clinical studies. The global topology optimization can incorporate anatomically accurate shape, which makes *in situ* fusion cage design possible. Various physiologically relevant loading modes at the lumbar spine were concurrently considered in the optimization procedure to ensure the *in vivo* structural integrity. Measured compressive strength revealed that our optimally designed PCL cages could support physiological load magnitudes at the lumbar spine. Furthermore, this design technique facilitates the design of fusion cages with specific physiological demands by introducing local microstructures with various stiffness, permeability and diffusivity properties.

With the solid freeform fabrication technique, our optimal PCL cages could be accurately constructed with controlled pore architectures and sufficient mechanical properties. The effectiveness of a laser sintered PCL as bone scaffold was previously attested by its stiffness close to that of trabecular bone and anatomically specific global shape with controlled porous architecture to allow bony ingrowth .(Williams et al. 2005) While the modulus of bulk PCL specimen was 120MPa in their study, the experimental and computationally estimated compressive modulus of porous scaffolds ranged from 46 to 68 MPa, falling within the lower range of human trabecular bone (Goulet et al. 1994). In our study, compressive modulus of bulk cylindrical specimen was 295 MPa, which is in the mid range of reported values (120~450 MPa).(Engelberg and Kohn 1991; Williams et al. 2005; Ang et al. 2007; Eshraghi and Das 2010) The improved strength may be due to optimally determined SLS processing parameters, including laser power, beam path speed, and PCL powder particle size.

Our porous fusion cages were demonstrated to support physiological loadings. To estimate *in vivo* load level in different postures, intradiscal pressure was measured in flexion up to 30º using pressure needle, and converted to load by multiplying disc area which was measured from an MRI scan.(Takahashi et al. 2006) In their study, the load levels at L4~L5 lumbar spine have been estimated around 500N to 3000N, varying according to posture. In another study, theoretical estimation of axial loads at L3 were reported to range from 340N ~ 2350N. (Schultz et al. 1982) Our compression tests revealed that the optimal fusion cages scaled for human vertebral geometry could withstand over 3kN of loads, which is above the physiological level of the human lumbar spine. The comparison of compressive mechanical responses with conventional TLIF

cages also demonstrated that inadequacy of adapting a design previously used for metallic cages.

Poly L-lactic acid (PLLA) has been utilized for biodegradable fusion cages with demonstrated feasibility for lumbar interbody.(van Dijk et al. 2002; van Dijk et al. 2002; van Dijk et al. 2003) In these studies, the PLLA cages were designed to have modulus of 4.2GPa, compressive stiffness of 4kN/mm, and average compressive yield load 3500 N. The optimal PCL cages in this study exhibited yield load equivalent to PLLA cages and had compressive stiffness that was higher than the PLLA cages (Table 4.3). It should be noted that thick solid wall around porous architecture contributed to the relatively high yield strength as well as stiffness compared to low modulus. Although the PLLA cages were designed for a large animal study and our optimal cages tested were scaled to human scale, the height of our specimen (9 mm) was comparable to the PLLA cages. In addition, the authors reported successful fusion with a flexible PLLA cage, which has 2kN compressive stiffness. Based on these comparisons, our PCL fusion cages may be feasible for lumbar interbody fusion.

The stiffness of our fabricated fusion cage can be improved by increasing HA contents in PCL powder, owing to HA's high stiffness. Shor et al. demonstrated 40% increase in the compressive modulus by adding 25% HA.(Shor et al. 2008) It was also reported that the stiffness of the PCL and HA mixture was proportional to the content of HA.(Ang et al. 2007) The reason we chose 7% of HA was due to a limitation of our SLS laser beam controllability. With further optimization of the laser beam parameter, our sintered PCL-HA composite fusion cages may have improved mechanical strength.

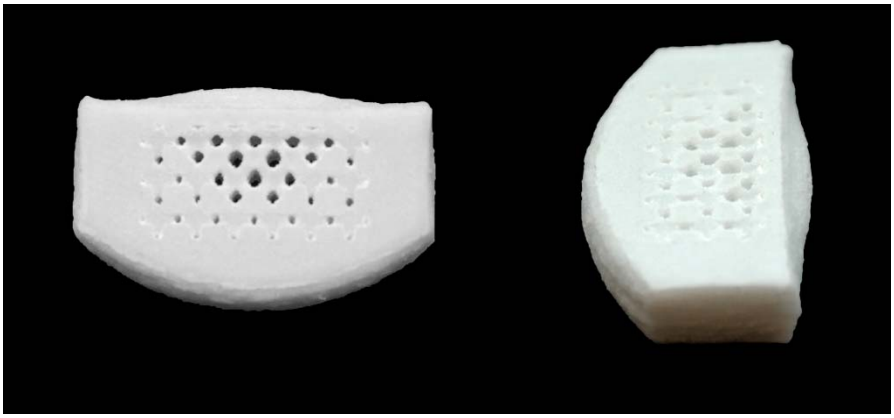

Figure 4.12 The deformation of the optimal fusion cage under compression up to 50% strain showed typical behavior of ductile material.

In addition to sufficient compressive modulus for load bearing, the ductility of the PCL may play a favorable role in preventing fracture of the cage into small pieces and maintaining the structural connectivity even under excessive loading condition. PCL has a very low glass transition temperature of -62°C and melting point of 57°C. At room temperature or in a body, PCL is in a rubbery state thus exhibiting high ductility.(Engelberg and Kohn 1991) Figure 4.12 shows the deformation of the optimal PCL cage after compression up to 50% strain. Although there was buckling of the thinner posterior wall, the overall structural topology was maintained without breaking apart

The long degradation profile compared to other degradable polymers may make PCL more suitable to the interbody fusion, which requires a long healing time of more than one year. Fast degradation and loss of structural integrity may cause poor fusion performance. Jiya et al. raised concern of using PLDLLA cages in their prospective randomized clinical study of comparing fusion performance between PEEK and PLDLLA cages.(Jiya et al. 2009) Their PLDLLA showed significantly higher subsidence

and lower fusion rate compared to PEEK due to early device failure. The authors explained that the rapid decrease of mechanical strength during degradation could be related to the device failure, which in turn resulted in the low rate of fusion. In vitro measurements of mechanical properties of PCL, such as modulus and yield stress, were shown to remain unchanged during the entire degradation time course.(Karjalainen et al. 1996) PCL was also shown to maintain initial elastic modulus and 95% of polymer mass up to 12 month *in vivo* (Pitt et al. 1981).

In an effort of elucidating optimal scaffold design parameters for better tissue regeneration, pore architectures, such as pore size and porosity, have been extensively investigated. Although there were large variations among researchers regarding optimal pore size, a minimum 300 um pore size has been suggested to enhance bone growth and capillary formation.(Karageorgiou and Kaplan 2005) The minimum pore size of our optimal cages was approximately 800 um, which is limited by current SLS processing parameters. In a previous study in our group, no significant differences were found in bone growth into PCL scaffolds at longer time point between pore sizes of 350 um and 800 um .(Roosa et al. 2010) Thus, it is expected that our porous PCL cages may enhance bone ingrowth with large enough pores, along with the maximized permeability design by local topology optimization.

The validity of using quadrupeds in the spine biomechanics studies has been questioned due to the differences in the anatomy and posture of quadrupeds.(Goel and Gilbertson 1997) However, spinal trabecular arrangements were found to be similar between human and porcine vertebrae, indicating axial compression along the spinal axis is dominant in porcine spine based on Wolf's law.(Lin et al. 1997) In addition, facet

joints are interlocking, rather than sliding with each other, which indicates that the load perpendicular to spinal column can be converted to longitudinal stress along the spinal column. Smit also supported the large quadraped pig animal model because of these similar loading modes.(Smit 2002) The author, however, noted that the considerably higher density of trabecular bone in quadruped vertebral bodies is an indication of higher load levels in the animal lumbar spine. The global topology optimization in this study was conducted with porcine lumbar spine geometry but the material properties were human. For application in a pre-clinical study, it will be important to consider the effect of these differences by developing the optimal topology designs for both sets of material properties.

Table 4.4 Surface to volume ratio of the microstructures used in this study

Microstructures	Porosity (%)	Pore surface area (mm^2)	specific surface area (mm^{-1})
(A)	29.4	12.54	1.568
(B)	40.0	9.61	1.201
(C)	58.8	14.16	1.770
(D)	60.	9.36	1.170

One of the possible applications of optimal microstructures in the interbody fusion would be controlled release of biologics such as BMP2. Although the microstructures were optimized in terms of functional properties such as permeability and diffusivity, it should be noted that the optimally designed microstructures were found to have larger

pore surface area than in the cylindrical or spherical pore microstructures (Table 4.4). Increased surface area with maximized permeability may increase the efficacy of osteobiologic release, especially if the BMP2 can be tightly bound to the cage with local retention. It is possible to modify the surfaces of these optimized cages using either biomineralization methods (Murphy et al. 2000) or by chemical conjugation techniques (Zhang et al. 2010). Integration of designed cages with osteobiologic delivery could address current limitations of current cage delivery systems that used a collagen sponge for osteobiologic delivery that is separate from the load bearing cage.

In conclusion, integrated global-local topology optimization combined with SFF technique in PCL and HA is promising method for the design of biodegradable fusion cages. Based on experimental and computational verification, optimally designed PCL cages have sufficient mechanical properties to support lumbar interbody loads. This combined with the longer degradation period of PCL may make bioresorbable cages again a viable solution for spine fusion applications. Of course, it will be necessary to rigorously test this postulate in a large pre-clinical animal model.

CHAPTER 5

MULTISCALE MODELING OF HYDROLYTIC DEGRADATION OF HIERARCHICAL SCAFFOLDS

5.1 Introduction

Degradation is one of the key features of the tissue engineering scaffolds. The scaffold provides initial functions, which new tissues take over as the scaffold degrades. This transition of functions should occur seamlessly so that the scaffolds maintain the initially designed functions throughout tissue healing (Figure 1.2). Although a scaffold is optimally designed, it may fail to heal defected tissues due to loss of tissue-scaffold functions, which can be caused by its early degradation. In this aspect, the design of the hierarchical scaffold should consider the changes of the properties and functions. To this end, the understanding of the degradation of polymeric scaffolds is key to successful design of the hierarchical scaffolds.

Aliphatic polyesters such as poly glycolic acid (PGA), poly lactic acid (PLA), and poly(ε-caprolactone) (PCL) are most commonly used biodegradable polymers in the tissue engineering. They are known to degrade by autocatalytic hydrolysis (Pitt et al. 1981; Li et al. 1990; Siparsky et al. 1998). These polymers have hydroxyl end groups on one end and carboxylic acid end group on the other of the polymer chain. Water

molecules penetrate into polymer matrix and randomly attack ester bonds at polymer backbone, producing smaller chains with carboxylic acid end group. As degradation proceeds, the polymer chains become smaller to be dissolved into aqueous medium. These water soluble small chains can diffuse out of polymer matrix, resulting in loss of mass. The chain cleavage of the aliphatic polyesters is accelerated by carboxylic acid end groups that are initially present or produced by the hydrolysis reaction (Li et al. 1990). The observations that thick polymer specimen degrades faster than thin one or faster degradation at the center of the specimen have been explained by the relative speed of the diffusion of the water soluble acidic products and auto-catalytic hydrolysis.

The complexity and difficulty in the design of biodegradable implant devices are attributed to this heterogeneous degradation of bulk eroded polymers. The design of the hierarchical scaffolds may be even more challenging due to the presence of complex pore architectures. The pore architecture of the hierarchical scaffold determines scaffold effective property, which will influence the transport of water and acidic products from hydrolysis reaction.

Of the mathematical or computational models formulated to address hydrolytic degradation of biodegradable polymers, empirical models based on the kinetic equations of hydrolysis and auto-catalytic hydrolysis are the simplest and easiest approaches, as presented in (Pitt and Gu 1987; Siparsky et al. 1998). Though these models can provide relatively accurate predictions, they only simulate the temporal changes of degradation and cannot reflect the spatial differences.

Some models capable of predicting temporal and spatial changes of molecular weights are based on Monte Carlo simulation (Gopferich and Langer 1993; Gopferich

1997), with the assigned life expectancy of a pixel based on Poisson's process. However, these models are not based on the actual degradation mechanism and, hence, cannot adequately relate to degradation with controlling parameters.

Wang et al. proposed a phenomenological degradation model, based on a diffusion-reaction continuum model (Wang et al. 2008), which addresses not only the spatial distribution of the ester bond concentration (equivalently molecular weight), but also the diffusion of carboxylic acids. Thus, they could demonstrate the heterogeneous bulk erosion and provided a degradation map according to the non-dimensional parameters for relative autocatalytic effects and the relative speed of diffusion of acidic products.

In this chapter, a diffusion-reaction model is adapted to the simulation of the hydrolytic degradation of solid polymer as well as porous scaffolds. Furthermore, the homogenization method is applied to provide a multiscale hydrolytic degradation model for hierarchical scaffolds. Unlike classical diffusion reaction equations based on phenomenological observations, the homogenization technique can rigorously simulate the effect of pore architecture on the effective properties of the scaffolds. The operating hypothesis is that the degradation of a porous scaffold is affected by the diffusion of water soluble chains with a carboxylic acid end group, which is in turn controlled by pore architecture. The goal of multi-scale modeling is to find design parameters of pore architecture that dominate the degradation of the porous scaffold and are key to the systematic design of hierarchical scaffolds with controlled degradability.

In order to investigate the effect of pore architecture on the degradation behavior in a more rigorous manner, currently available reaction-diffusion models were utilized to qualitatively simulate the different erosion mechanisms (surface/bulk erosion) by

accounting for water diffusion and hydrolysis. In addition, the aforementioned heterogeneous erosion was demonstrated by the interplay between the diffusion of acidic products and autocatalytic hydrolysis. The current model was then adapted to simulate the degradation of porous scaffolds in relation to scaffold geometric parameters. Finally, the multi-scale homogenization for diffusion reaction based degradation was used to rigorously investigate the effect of microstructures on the degradation.

5.1.1 Hydrolysis Kinetics: Autocatalysis

The degradation of linear aliphatic polyesters begins with the attack of water molecule at an ester bond. With the presence of carboxylic acid, one reaction produces another carboxylic acid, consuming water molecule and ester bond (Figure 5.1). This already presented carboxylic acid and produced one during the degradation are known to accelerate the hydrolysis by acid catalysis (Pitt et al. 1981; Siparsky et al. 1998).

For acid-catalyzed hydrolysis, the following kinetic relation has been proposed (Pitt et al. 1981).

$$-\frac{d[\mathrm{E}]}{dt} = \frac{d[\mathrm{COOH}]}{dt} = k[\mathrm{H_2O}][\mathrm{E}][\mathrm{COOH}] \tag{5.1}$$

where $[\mathrm{COOH}]$ is the concentration of carboxylic acid end group, $[\mathrm{E}]$ is the concentration of ester bonds, [H2O] is the concentration of water molecule, and k is reaction rate constant.

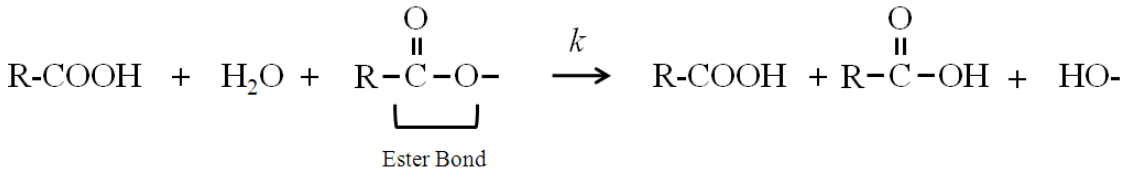

Figure 5.1 Acid-catalyzed hydrolysis reaction

The concentration of the acid end group, [COOH], can be related to the molecular weight of the polyester or to the concentration of ester bonds, [E], ((Lyu and Untereker 2009))

$$[\mathrm{COOH}] = \frac{\rho}{\overline{\mathrm{Mn}}} \approx \frac{[\mathrm{E}]}{\overline{\mathrm{DPn}}} \tag{5.2}$$

where ρ is the density of the polyester, which is typically 1.2 g/cm^3. $\overline{\mathrm{Mn}}$ is the number average molecular weight and $\overline{\mathrm{DPn}}$ is the number average of the degree of polymerization.

Substitution of (5.2) into (5.1) results in

$$\frac{d}{dt}\left(\frac{\rho}{\overline{\mathrm{Mn}}}\right) = k[\mathrm{H_2O}]\overline{\mathrm{DPn}}\left(\frac{\rho}{\overline{\mathrm{Mn}}}\right)^2 \tag{5.3}$$

Assuming constant polymer density throughout degradation,

$$\frac{d}{dt}\left(\frac{1}{\overline{\mathrm{Mn}}}\right) = k'\left(\frac{1}{\overline{\mathrm{Mn}}}\right) \tag{5.4}$$

where $k' = k[\mathrm{H_2O}](\rho/m)$ with m number of repeating monomer unit in a polymer chain. Thus, the molecular weight change by autocatalytic degradation of polyesters can be modeled as simple exponential decay with initial molecular weight, $\overline{\mathrm{Mn}}_0$.

$$\frac{\overline{\mathrm{Mn}}}{\overline{\mathrm{Mn}}_0} = \exp(-k't) \tag{5.5}$$

This simple relationship works well in describing the change of molecular weight of many types of polyester. As discussed by Pitt et al. (Pitt et al. 1981), however, the carboxylic acid group in aliphatic polyesters may participate in the transition state of the reaction in its undissociated form. Thus, the reaction rate may be dependent on the half order of the acid end group concentration, rather than the first order concentration. Siparsky (Siparsky et al. 1998) showed in a solution hydrolysis study that the autocatalytic degradation of PLA was best fitted with half order of carboxylic end group concentration as catalyst acid concentration, while first order of acid concentration is used in the product.

$$\frac{d[\mathrm{E}]}{dt} = -k[\mathrm{H_2O}][\mathrm{E}]([\mathrm{COOH}]K_a)^{1/2} \tag{5.6}$$

where K_a is acid dissociation constant.

PCL appeared to following first order kinetics than half order of carboxylic acid in the same study (Siparsky et al. 1998). As a starting point, second order kinetics are used with the pseudo first order reaction rate, $k' = k[\mathrm{H_2O}]$, assuming water concentration is constant. Some measured values of the pseudo first order reaction rates are presented in Table 5.1.

Table 5.1 Autocatalytic hydrolysis reaction rates of linear aliphatic polymers (Pitt et al. 1981; Antheunis et al. 2009).

Polymer	Reaction Kinetics	Reaction rate	Reference
PCL	$k[H_2O][E]$	3.07×10^{-3} (/day)	Pitt 1998
PCL	$k[H_2O]$	0.421×10^{-3} (/mol/day)	Antheunis 2009
PLA	$k[H_2O]$	6.44×10^{-3} (/mol/day)	Antheunis 2009
PLGA75:25	$k[H_2O]$	10.3×10^{-3} (/mol/day)	Antheunis 2009
PLGA53:47	$k[H_2O]$	12.9×10^{-3} (/mol/day)	Antheunis 2009

$[H_2O]$ is concentration of water molecules, and [E] is concentration of ester bonds.

5.2 Computational Modeling of Hydrolytic Degradation

In this section, the polymer degradation process was modeled using a set of diffusion-reaction equations which account for ester bonds (C_E), small polymer chain dissolved in aqueous media (C_M), and water molecules (C_W). Characteristic phenomenon of aliphatic polyesters such as the transition between bulk erosion and surface erosion, and heterogeneous bulk erosion are demonstrated in the diffusion reaction equations.

5.2.1 Diffusion-Reaction Based Model for Erosion Mechanisms

Hydrolysis depends on ester bond and water molecule concentration (Siparsky et al. 1998). The interplay between water diffusion velocity and the hydrolysis reaction rate determines the erosion mechanism: either surface erosion or bulk erosion. This has been supported by several theoretical studies that modeled the erosion mechanism based on the relative speed of water diffusion compared to hydrolysis (von Burkersroda et al. 2002; Lyu et al. 2005; Rothstein et al. 2009).

In this section, a diffusion-reaction system was used to qualitatively characterize the erosion mechanism based on water diffusion and the hydrolysis reaction.

$$\frac{\partial C_W}{\partial t} = \nabla\left(D_W \nabla C_W\right) - kC_W C_E \tag{5.7}$$

$$\frac{\partial C_E}{\partial t} = -kC_W C_E \tag{5.8}$$

where C_E, and C_W are the concentration of ester bonds and water molecule, repectively. D_W is the water diffusion tensor and k is the second order reaction rate. Typical values of the diffusion coefficient of water in an amorphous polymer are about 10^{-8} to 10^{-9} cm^2/s (Milroy et al. 2003; Lyu and Untereker 2009).

Nondimensionalized equations are derived as

$$\frac{\partial \overline{C}_W}{\partial T} = \frac{t_E^*}{t_W^*}\nabla^2 \overline{C}_W - \overline{C}_W \overline{C}_E \tag{5.9}$$

$$\frac{\partial \overline{C}_E}{\partial T} = -\overline{C}_W \overline{C}_E \tag{5.10}$$

where $t_E^* = 1/k'C_E^*$, $t_W^* = L^2/D_W$, $\overline{C}_W = C_W/C_E^*$, $\overline{C}_E = C_E/C_E^*$, $\mathbf{X} = \mathbf{x}/L$ C_E^* is initial ester bond concentration, L is half the plate thickness.

We can then introduce a non-dimensional parameter, ε_W, which is the ratio of the characteristic time of the hydrolysis reaction to the characteristic time for water diffusion.

$$\varepsilon_W = \frac{t_E^*}{t_W^*} = \frac{D_W}{L^2 k C_E^*} \tag{5.11}$$

According to this variable, a different erosion mechanism is simulated.

- $\varepsilon_W >> 1$: The time of water diffusion is much smaller than the hydrolysis reaction. Thus, polymer undergoes bulk erosion.
- $\varepsilon_W << 1$: The time of water diffusion is much greater than the hydrolysis reaction. Thus, the polymer undergoes surface erosion.
- $\varepsilon_W \sim 1$: The time of water diffusion is comparable to the hydrolysis reaction. Thus, polymer undergoes in between bulk and surface erosion.

For a large plate of PLA with 2 cm thickness, $\varepsilon_W = 27.7$ using the following values, implies that it will undergo bulk erosion.

- $D_W = 10^{-8}$ cm^2/s = 8.64×10^{-3} (cm^2/day)
- $k = 6.5 \times 10^{-3}$ (/day/mol)
- $C_E^* = \overline{\mathrm{DPn}} \cdot \rho / \overline{\mathrm{Mn}}$ = 500*1.2 (g/cm^3) / 50,000 (g/mol) = 0.012 mol/ cm^3
- L=2cm

It is expected that at a thickness greater than 10 cm, PLA is expected to start the transition from bulk erosion to surface erosion.

The transition of erosion mechanisms according to ε_W, can be more clearly visualized by the analysis in the large plate model. The large plate domain can be approximated with 1 dimensional diffusion reaction problem assuming no diffusion in the tangent directions to the plate surface (Figure 5.2). The symmetric boundary condition was assigned at x=0 (center of the plate) and homogeneous boundary condition was set at x=1 (outer surface of the plate).

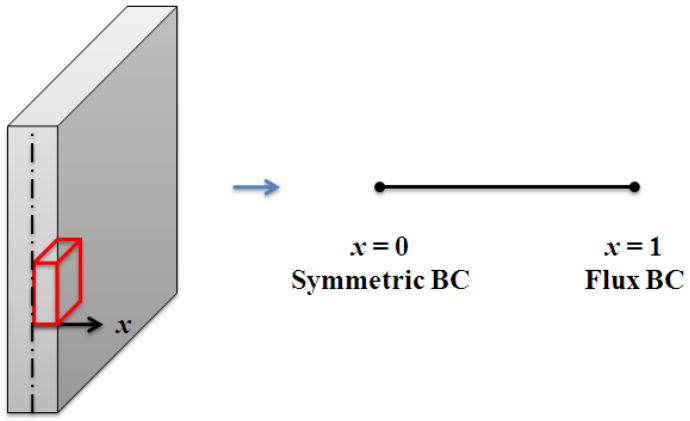

Figure 5.2 The diffusion reaction problem in a large plate of PLA is approximated as one dimensional problem.

Figure 5.3 clearly illustrates the transition of bulk erosion to surface erosion according to the nondimensional parameter, ε_W. Note that x = 0 indicates the center of the plate and x = 1 indicates surface of the plate, in the plots. With ε_W=100, homogeneous degradation was simulated throughout the polymer dimension, while complete degradation occurred from the right side when ε_W=0.01. If ε_W is around 1, transition between the erosion mechanisms is observed. The ester bond concentration has been correlated to molecular weight, so the spatial distribution of the local ester bond concentration can be regarded as the molecular weight distribution. It should be noted that this is rather a qualitative estimation for the degradation mechanism. Considering our typical scaffold size ranges from 5 mm to 50 mm, bulk erosion is assumed for all the following sections.

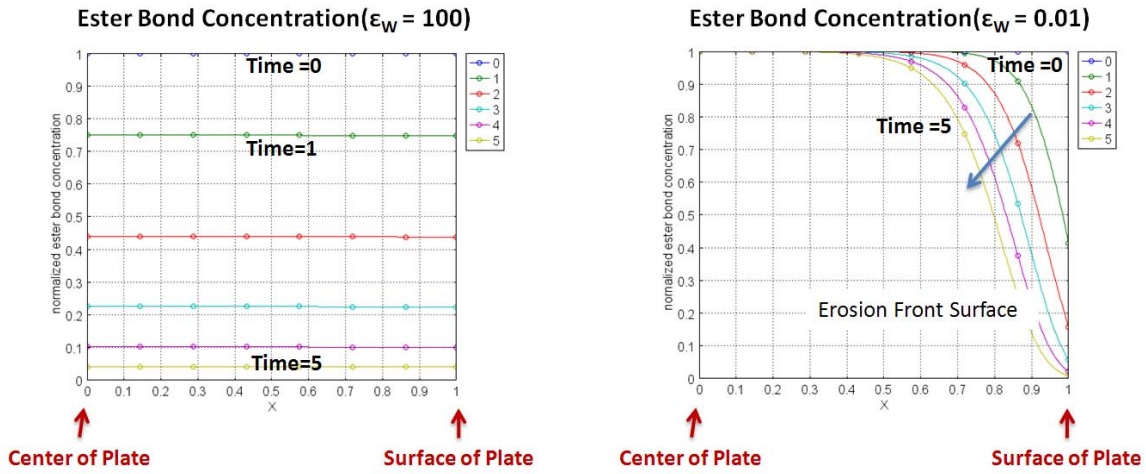

Figure 5.3 Bulk erosion occurs if water diffusion is much faster than the hydrolysis reaction(ε_W=100), and surface erosion occurs when water diffusion is much slower than hydrolysis(ε_W=0.01). The X axis is perpendicular to polymer plate with its origin at the center of the thickness. The local ester bond concentration along the x axis was assumed to be proportional to the local molecular weight.

5.2.2 Heterogeneous Degradation in Bulk Erosion

A similar reaction-diffusion equation can be applied to simulate the heterogeneous degradation in bulk eroded polymers. In this case, the concentration of water soluble small chains with a carboxylic acid end group (C_A) and the ester bond concentration (C_E) are included in the system of diffusion-reaction equations. We assumed that water diffusion is much faster than hydrolysis and that water is abundant throughout the simulation, indicating bulk erosion. It is also assumed that if the molecular weight of a polymer chain is below a threshold value, the small polymer chain becomes soluble in water. Then, the water soluble small polymer chains can diffuse out of the polymer matrix, resulting in a mass loss of the polymer. The interplay between the autocatalytic

hydrolysis reaction and the water soluble monomer may determine the degradation behavior of the bulk eroding polymers.

It is hence assumed in this section that:

- Water is already diffused throughout the polymer matrix and abundant. Thus, the hydrolysis kinetics can be considered as pseudo first order kinetics, assuming constant water concentration.
- the presence of second order kinetics of acid-catalyzed hydrolysis per (5.1).
- an uncatalyzed hydrolysis reaction is included, which ensures the initial production of carboxylic acid end groups in this model.

From the acid catalyzed reaction kinetics of (5.1), two rate equations can be derived for carboxylic acid production and ester bond consumption. Considering the production and diffusion of small carboxylic acid (C_A), and ester bond consumption (C_E), the nondimensionalized form of the coupled diffusion-reaction equation is

$$\frac{\partial \overline{C}_A}{\partial T} = \frac{t_E^*}{t_A^*}\nabla^2 \overline{C}_W + \bar{k}_{12}\overline{C}_E + \overline{C}_A\overline{C}_E \tag{5.12}$$

$$\frac{\partial \overline{C}_E}{\partial T} = -\bar{k}_{12}\overline{C}_E - \overline{C}_A\overline{C}_E \tag{5.13}$$

where $t_E^* = 1/k_2 C_E^*$, $\bar{k}_{12} = k_1/k_2 C_E^*$, $t_A^* = L^2/D_A$, $\overline{C}_A = C_A/C_E^*$, $\overline{C}_E = C_E/C_E^*$, $\mathbf{X} = \mathbf{x}/L$.

k_1 and k_2 are pseudo first order uncatalyzed hydrolysis reaction rate and pseudo first order acid catalyzed hydrolysis reaction rate, respectively. D_A is the diffusion coefficient of small chains with carboxylic acid end group. C_E^* is the initial ester bond concentration, L is half the plate thickness.

As presented in Wang et al (Wang et al. 2008), the ratio of both uncatalyzed and acid-catalyzed hydrolysis reaction rates, and the ratio of acid-catalyzed hydrolysis reaction to diffusion of small chains control system behavior.

Let us set $\varepsilon_A = \frac{t_E^*}{t_A^*}$. The large value of ε_A indicates a fast acid group diffusion (or a slow hydrolysis reaction), and a small value of ε_A indicates a fast hydrolysis reaction (or slow acid group diffusion). For the ratio of the uncatalyzed reaction rate and acid catalyzed reaction, a large $\bar{k}_{12}$ implies the reduced effect of autocatalysis, whereas small $\bar{k}_{12}$ implies relative dominance of autocatalysis.

Figure 5.4 illustrates the differential effects of ε_A and $\bar{k}_{12}$ on the spatial variations of degradation along the polymer matrix. In Figure 5.4 , the upper three plots are for $\bar{k}_{12}$ =0.1 and lower three are for $\bar{k}_{12}$=1. In addition, plots in the left column are for ε_A=0.1, plots in the center column are for ε_A=1, and plots in the right column are for ε_A=10. For ε_A=0.1 (slow acid diffusion) and $\bar{k}_{12}$=0.1 (dominant autocatalysis over uncatalyzed hydrolysis), the heterogeneity was maximized, with faster degradation at the center (x=0) than at the surface (x=1). On the other hand, it appears that larger ε_A results in homogeneous degradation. The effect of $\bar{k}_{12}$ can be observed by comparing plots in the upper and lower row in Figure 5.4. Large $\bar{k}_{12}$ tends to accelerate overall degradation speed. We may conclude that heterogeneous bulk erosion can be observed with greater autocatalytic hydrolysis and reduced diffusivity of the acidic product.

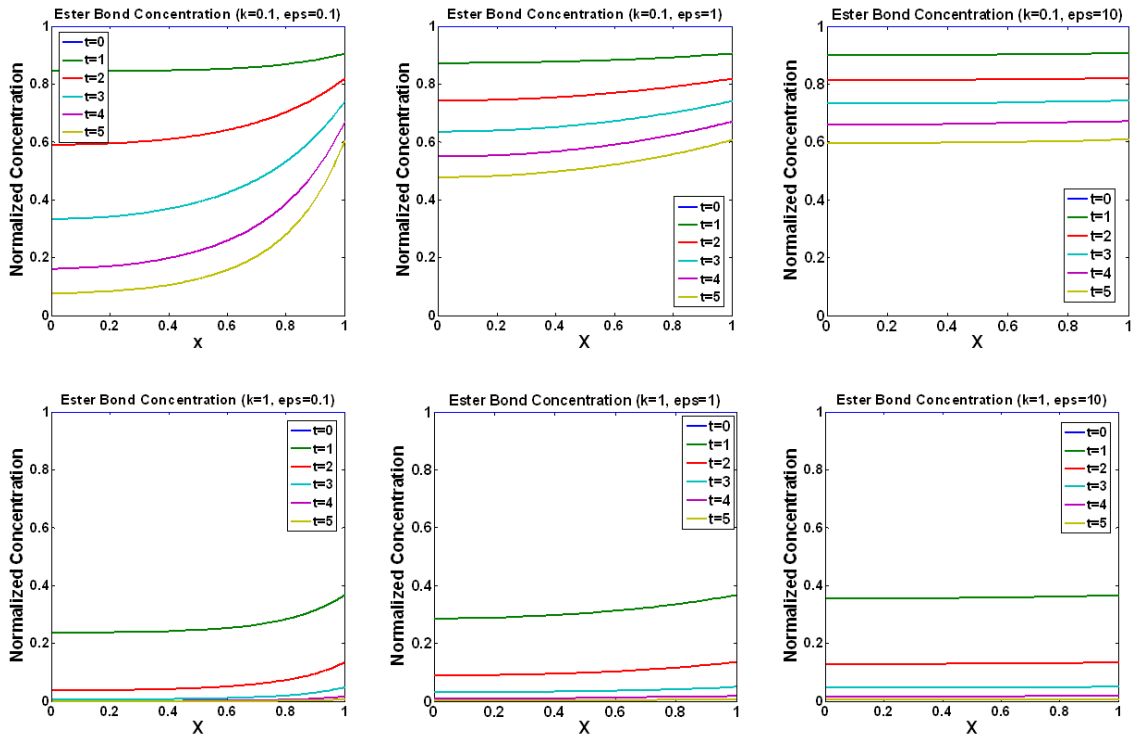

Figure 5.4 Heterogeneous erosion was simulated with different ε_A and $\bar{k}_{12}$ values. Larger ε_A tends to increase heterogeneity in the ester bond concentration while larger $\bar{k}_{12}$ accelerates the overall degradation speed.

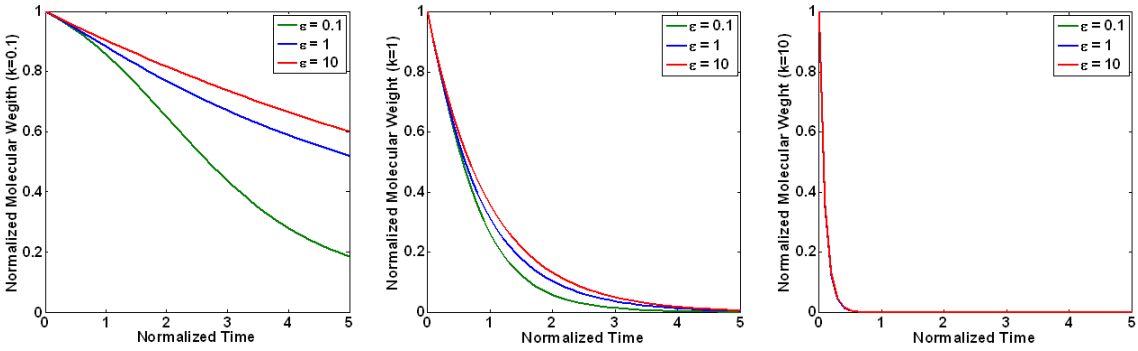

Figure 5.5 Molecular weight profiles (degradation) along time were demonstrated with different ε_A and $\bar{k}_{12}$ values: The left hand plot is for $\bar{k}_{12}$=0.1 with varying ε_A, the center plot is for $\bar{k}_{12}$=1, and the right hand plot is for $\bar{k}_{12}$ =10. For $\bar{k}_{12}$=10, the effect of ε_A vanishes. (curves in green: ε_A=0.1, curves in blue: ε_A=1, and curves in red: ε_A=10)

In Figure 5.5, normalized molecular weight profiles were presented. The molecular weights remaining in the polymer were calculated by integrating the remaining ester bond concentrations within polymer domain. With the reduced effects of uncatalyzed hydrolysis (smaller $\bar{k}_{12}$), the differential effects of the degradation profile by ε_A are evident. When $\bar{k}_{12}$ was increased to 10, no effects of ε_A were observed.

Another interesting factor is mass loss, which was modeled by out flux of acid end groups as shown in Figure 5.6. As ε_A increases (fast diffusion), initial burst of acid outflux was clearly demonstrated. The peak values of the bursts were proportional to $\bar{k}_{12}$. It should be noted that the boundary flux profile is bell shaped. This observation will be utilized as a simplified model for the homogenization of reaction diffusion in the following section.

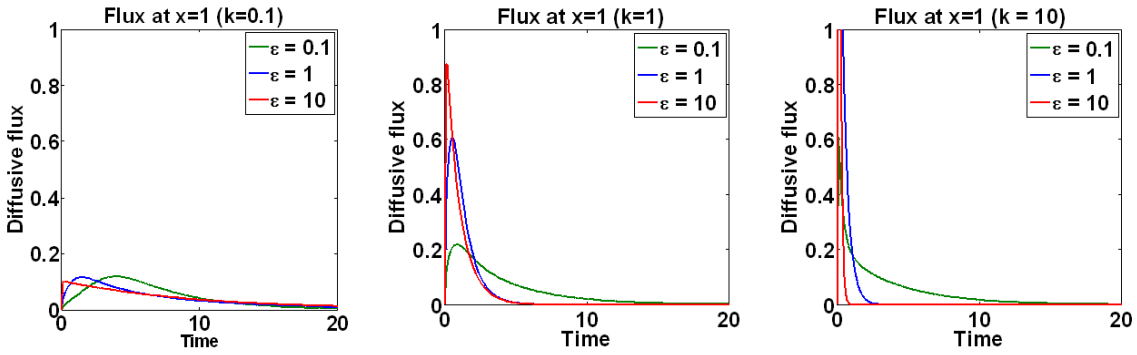

Figure 5.6 Fluxes of the small carboxylic acid end groups out of the polymer matrix were plotted over simulation time with varying ε_A values.

5.2.3 Degradation of Porous Scaffolds

Pore architectures such as pore size as well as porosity, and interconnectivity (diffusivity/permeability) have been correlated with tissue regeneration. The degradation of porous scaffold can also be affected by these architectural parameters. To investigate the effect of pore architecture on the degradation, microstructures with different physical sizes were modeled. Then, finite element models of two different scaffolds were prepared with Comsol Multiphysics (Figure 5.7). The diffusion reaction system of (5.12) and (5.13) was used to simulate the degradation of these scaffolds. Scaffolds composed of 2x2x2 unit microstructures were modeled by assigning symmetric boundary conditions. The diffusion of the carboxylic acid end group concentration at the opposite sides of symmetric planes were set at zero. The initial concentration of carboxylic acid was zero and the ester bond concentration was one.

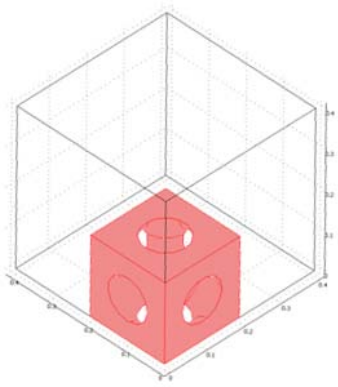

Figure 5.7 The simulation domain consists of 2x2x2 unit microstructure array (implemented by symmetric boundary conditions), and surrounding medium.

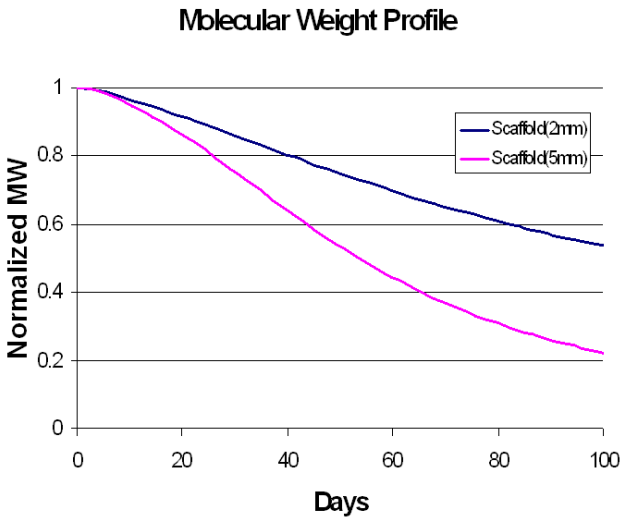

Figure 5.8 Comparison of molecular weight profiles between scaffolds with 2mm and 5mm unit microstructures. Scaffold with large unit microstructures degrade faster than those with small unit microstructures.

The simulation results demonstrated faster degradation of larger scaffolds (Figure 5.8). This result confirms that thicker polymer blocks degrade faster than thinner ones. In this simulation, ε_A was 0.002 for the scaffold with 5mm unit microstructures, and ε_A was set at 0.01 for the scaffold with 2mm unit microstructures. $\bar{k}_{12}$ was set 0.7 for both scaffolds. The differences in ε_A are due to the different characteristic lengths.

To further investigate the size effect, a series of degradation simulations were conducted with scaffolds of different pore size microstructures. Unit microstructures with cylindrical holes were modeled for this purpose by varying the hole diameters. The size of the unit microstructures was the same for all the models, thus the size of the scaffolds was the same, too. The results showed that the scaffolds with smaller hole size degraded faster than those with larger holes (Figure 5.9). This supports that the thicker polymer degrade faster than thinner polymer because the hole size is inversely proportional to the strut size in this case. It should be noted that the hole size is proportional to diffusivity/permeability for the scaffolds with cylindrical microstructures. Furthermore, one may postulate that scaffolds with high diffusivity degrade slowly due to fast removal of acidic product that is involved in the hydrolysis. Although it appears that mass transport properties of the scaffolds affected the degradation, current diffusion-reaction model cannot simulate the diffusion of the acidic products within pores. Thus, more rigorous investigation may need a multiscale modeling to account for the effects of detailed microstructures on the degradation.

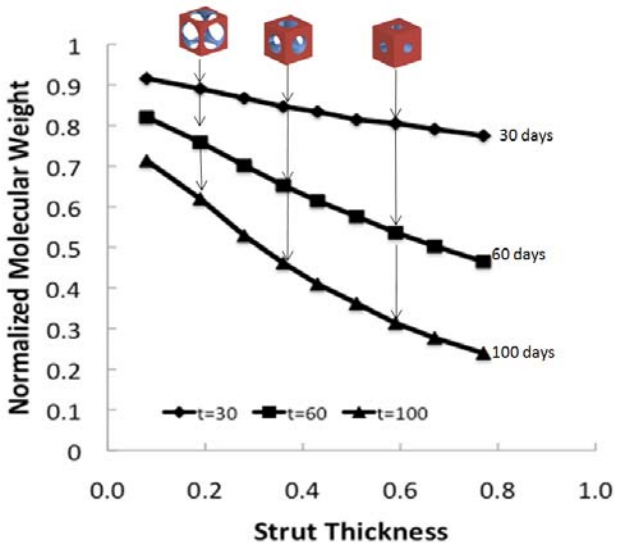

Figure 5.9 Molecular weight profiles were compared among scaffolds with different strut size microstructures. Larger strut size, or thickness, were shown to be related to faster degradation.

5.3 Homogenization Model for Hydrolytic Degradation of Porous Scaffold

This section provides the derivation of the homogenization model of diffusion-reaction system for the hydrolytic degradation of porous scaffold. Since we only consider a case in which diffusivities of a solute (carboxylic acid end group) in the solid and pore are highly two orders of magnitude different, this homogenization model presented in this thesis is not complete. However, this will offer a good starting point to extend the current diffusion-reaction model to a multiscale model.

5.3.1 The Governing System of Equations

The degradation of aliphatic polyesters is generally known to follow bulk erosion mechanism. The mechanism is briefly explained by initially rapid decrease in molecular weight and the consequent deceleration occurring upon the release of monomers. At the later stage, actual mass loss occurs because these small polymer chains become water

soluble and diffuse out of the polymer matrix. It is also known that these acidic products become involved again in the reaction, resulting in acid-catalyzed hydrolysis. The diffusion of the acidic product, or water soluble small chains, has been attributed to the heterogeneous erosion of bulk eroded polyesters. For example, Grizzi et al. compared the degradation of thick plates and thin films made from poly(DL-lactic acid) to investigate the size dependency of the degradation (Grizzi et al. 1995). The authors demonstrated that the inner region of the thick plates degrades faster than outer shell, ultimately resulting in a hollow structure at the end of degradation.

In our hierarchical scaffolds, the degradation behavior may be altered by the pore architecture. At the pore surface inside the scaffold, the water soluble monomers can release to the pore region as well as diffuse through the polymer matrix. Release from the hierarchical scaffold may be dependent on the effective diffusivity of the scaffold, which in turn can be controlled by the scaffold pore architecture as shown in chapter 3. If a scaffold is designed to possess low diffusivity, the accumulation of the acids may occur in the pore and affect the degradation of pore surface area. A computational model based on the multiscale homogenization method would be a good candidate for simulating the degradation of the porous scaffolds. We derived the homogenization of reaction-diffusion in chapter 2. The homogenized equations account for production and diffusion of the water soluble acids. The hydrolysis reaction is assumed to occur only in the solid matrix, so that the rate equation for the ester bond concentration being considered as local phenomenon.

The governing equation accounting for the reaction-diffusion of the water soluble small acidic chain is derived from equation (2.49), assuming linear reaction terms in the

local equation. The rate equation for the ester bond is coupled through these reaction terms at the local polymer domain.

The system of homogenized reaction-diffusion equations in nondimensional formis

$$\phi_1 \frac{\partial \bar{c}_1^{(0)}}{\partial \bar{t}} - \frac{\partial}{\partial x_i} \bar{D}_{ij}^H \frac{\partial \bar{c}_1^{(0)}}{\partial x_j} = -\frac{1}{|\Omega|} \int_\Gamma \bar{D}_{ij}^{(2)} \frac{\partial}{\partial y_j} \bar{c}_2^* n_i d\Gamma \tag{5.14}$$

$$\frac{\partial \bar{c}_2^*}{\partial \bar{t}} - \frac{\partial}{\partial y_i} \bar{D}_{ij}^{(2)} \frac{\partial}{\partial y_j} \bar{c}_2^* = T_{1L} k_1' \bar{c}_E + T_{1L} k_2' c_{2c} \bar{c}_E (\bar{c}_2^* + \bar{c}_1^{(0)}) - \frac{\partial \bar{c}_1^{(0)}}{\partial \bar{t}} \tag{5.15}$$

$$\frac{\partial \bar{c}_E}{\partial \bar{t}} = -T_{1L} k_1' \bar{c}_E - T_{1L} k_2' c_{2c} \bar{c}_E (\bar{c}_2^* + \bar{c}_1^{(0)}) \tag{5.16}$$

where k_1' and k_2' are uncatalyzed and acid-catalyzed reaction rates, respectively. $\bar{c}_1^{(0)}$ and $\bar{c}_2^*$ are carboxylic acid concentrations in the pore and polymer matrix, respectively, and $\bar{c}_E$ is the ester bond concentration. T_{1L} is the characteristic time for diffusion in the pore space defined in (2.33). $\bar{D}_{ij}^H$ is the effective diffusivity of the carboxylic acid end groups **in the pore** and $\bar{D}_{ij}^{(2)}$ is the nondimensional diffusivity of carboxylic acid end groups **in the polymer matrix**. c_{2c} is a characteristic concentration of the carboxylic acid end groups in the solid matrix. In fact, c_{2c} can be the initial ester bond concentration, as used in equations (5.12) and (5.13). Note that hydrolysis reaction occurs at solid matrix, which is Ω_2 in Figure 2.3. Thus, the rate equation for ester bond concentration is solved in the microstructure domain only. The equations (5.14)~(5.16) are homogenized version of equations (5.12) and (5.13). Also note that $\bar{c}_1^{(0)}$, the carboxylic acid concentration in the polymer matrix, is relative to $\bar{c}_2^*$, the carboxylic acid

concentration in the pore. That is, $\bar{c}_1^{(0)}$ is zero in the pore and at the pore-polymer matrix boundary and has values inside the polymer matrix.

In the following sections, we first investigated the behavior of the macroscopic equations by decoupling the system of equations (5.14)~(5.16), to see the effect of global source term on the response of macroscopic equation. Then, the coupled equation is directly solved by introducing microstructures at some sample locations.

5.3.2 Investigation of the Macroscopic Equation

The macroscopic equation (5.14) contains a source term which is dependent on the local boundary flux out of the solid polymer domain. The integration of the local flux along the solid-void boundary serves as a source term in the macroscopic equation. The efflux of acids, or release of the acidic small chains, is time dependent, as illustrated in Figure 5.6. To investigate the behavior of the macroscopic equation by the time dependent source term, we first tested the probability density function of the normal distribution as a time dependent source term in (5.14), to impose a standard bell shaped production of acids along the degradation time (Figure 5.6).

$$\phi_1 \frac{\partial \bar{c}_1^{(0)}}{\partial \bar{t}} - \frac{\partial}{\partial x_i} \bar{D}_{ij}^H \frac{\partial \bar{c}_1^{(0)}}{\partial x_j} = F(\bar{t}) \tag{5.17}$$

$$F(\bar{t}) = \frac{1}{\sqrt{2\pi\sigma^2}} \exp\left(- \frac{(\bar{t} - \mu)^2}{2\sigma^2} \right) \tag{5.18}$$

where σ is the variation and μ is the mean value.

Equation (5.17) was solved in a one-dimensional domain as illustrated in Figure 5.2. For the time dependent source term defined in (5.18), release of the small chains, were

measured at the polymer surface (x=1). As presented in Figure 5.10, changing the effective diffusivity in the equation resulted in different efflux profiles over time. Typical delays in the release profiles were observed with decreased effective diffusivity. However, the porosity (volume fraction of pore domain) of the microstructure is generally proportional to the effective diffusivity. Considering the linear relation between porosity and effective diffusivity, the differential effects of the diffusivity appears to vanish (Figure 5.11). For this purpose, we assumed the porosity equals the normalized effective diffusivity.

From these observations, we may predict the acidic chain release profiles for different microstructures. For example, a scaffold made of a microstructure with 50% porosity and 10% diffusivity will release the small polymer chains with a delayed profile. On the other hand, a scaffold with 50% porosity and 40% diffusivity will release the chains in a pattern following the source term profile.

In the homogenization formulation (equations (5.14)~(5.16)), the macroscopic equation and microscopic equation are coupled in both time and space. We expected that the solution of this coupling system will give more detailed effects ofmicrostructures on the degradation.

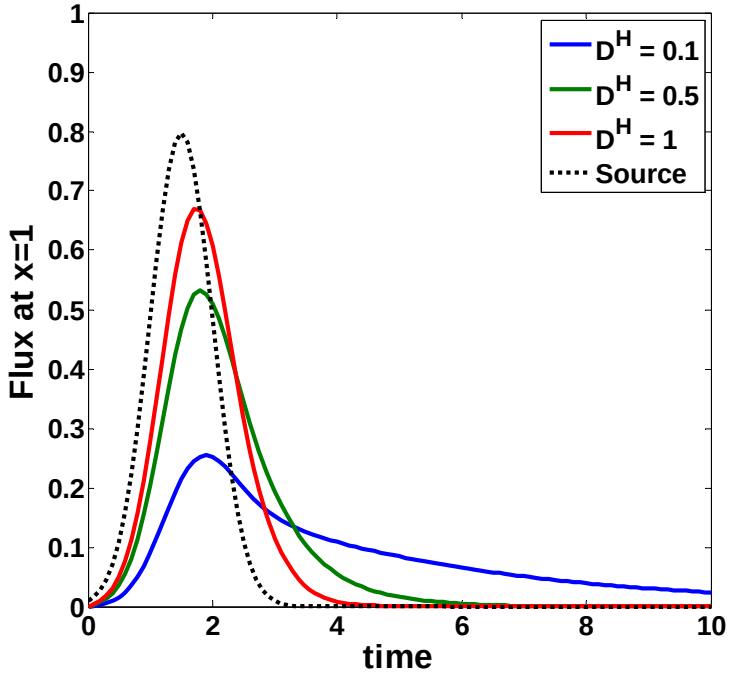

Figure 5.10 Without considering porosity at the time derivative term, the effective diffusivity affects the flux profile.

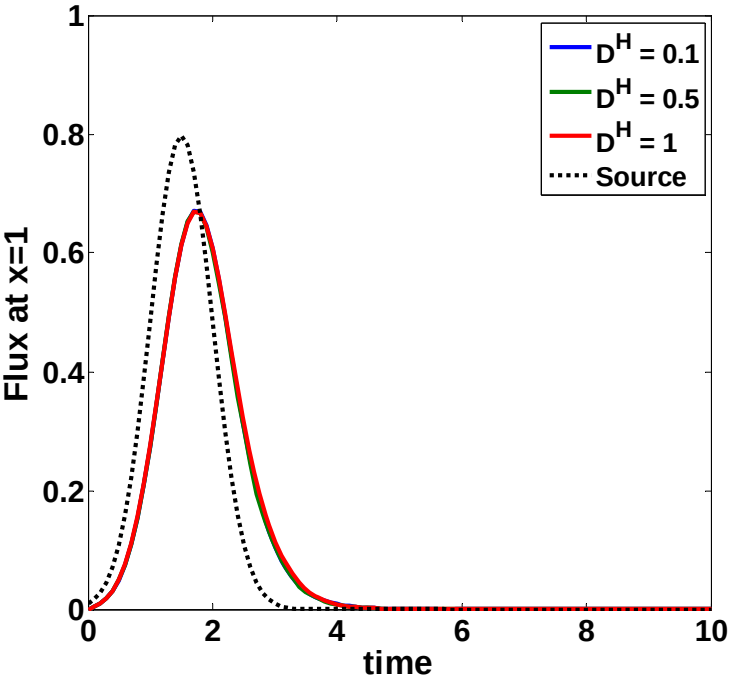

Figure 5.11 Effluxes were measured for a bell shaped time dependent source term. The effect of the effective diffusivity (D^H) was not observed.

5.3.3 Evaluation of the Non-Dimensional Parameters

Before solving the equations (5.14)~(5.16), the nondimensional parameters should be evaluated with physically relevant values. Suppose that the scaffold dimension (L) is 2 cm, and unit microstructural dimension (l) is 0.1 cm. Because the homogenized equation is valid when q=2 in relation (2.35), that is $T_{1L} \approx T_{2l}$, the diffusion of the carboxylic acid in the pore of the scaffold is comparable to the diffusion of the carboxylic acid in the polymer matrix within a unit microstructure. From the parameter values in Table 5.2 , the nondimensional coefficients in equations (5.15) and (5.16) can be estimated.

$$\begin{aligned} k'T_{1L} &\approx 0.35 \\ k'T_{1L}c_{2c} &\approx 0.1 \end{aligned} \tag{5.19}$$

Table 5.2 Parameters used in this study.

Parameter	Value	Description	Reference
D_1	1.22×10^{-3} (cm2/day)	Diffusivity in the pore	Estimated by the relation $D_1 = D_2L^2 / l_2$
D_2	1.218×10^{-5} (cm2/day)	Diffusivity in polymer matrix	(Wang et al. 2008)
C_{2c}	1.73×10^{-2} (mol/cm3)	Initial concentration of ester bonds	(Wang et al. 2008)
k_1'	4.29×10^{-4} (/mol/day)	Uncatalyzed reaction rate	(Wang et al. 2008)
k_2'	6.44×10^{-3} (/mol/day)	Autocatalysis reaction rate	(Antheunis et al. 2009)

5.3.4 Solving the coupled Multiscale Degradation Model

In the simulation model, illustrated in Figure 5.12, the macroscopic domain is a porous infinite plate with repeating unit microstructures, which is modeled as a one dimensional problem. For demonstration purpose, we assumed two dimensional microstructures at five sampling points in the macroscopic domain for demonstration purpose. The microstructure domain is further divided into a polymer matrix and pore space. The effective diffusivity used in the macroscopic equation is calculated from the homogenization of diffusion in the pore space. The microscopic equation (5.15) and (5.16) are solved in the polymer matrix domain and provide a time dependent source term. Because of the coupling of the macroscopic variable and its time derivative in equations (5.15), with the source term from local flux in (5.14), these equations should be solved together.

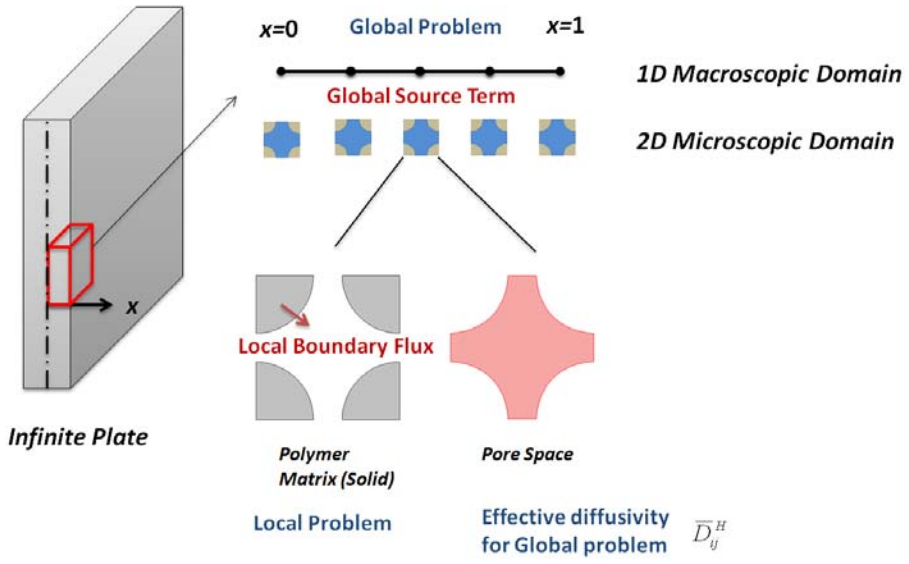

Figure 5.12 Schematics of the simulation domain. An infinite plate was modeled one dimensional problem, where x=0 at the center of the plate and x=1 at the plate surface. two dimensional microscopic domains were defined at five sampling points in the global domain for the local boundary value problems. Local boundary flux serves as a global source term.

A symmetric boundary condition was imposed at x=0 (center of the plate) while homogeneous boundary condition was imposed at x=1. In the local problem, periodic boundary conditions were imposed.

At the initial time point, the microscopic equation was solved five times with initial values from the five sampling points. Then, the integrated local boundary fluxes were fitted to a function of x, the global spatial variable. With this interpolated function as the source term, the macroscopic equation was solved. Then, the initial values for both equations were updated and moved to the next time step. Using FEMLab scripting, these solution steps were implemented within a loop, along with the effective diffusivity calculation.

5.3.5 Results

Using FEMLab, the effective diffusivity was evaluated as 0.343. With the assumption that the scaffold undergoes bulk erosion and there is no solid-fluid boundary change, the effective diffusivity remains constant throughout the simulation. The local characteristic concentration is shown in Figure 5.13.

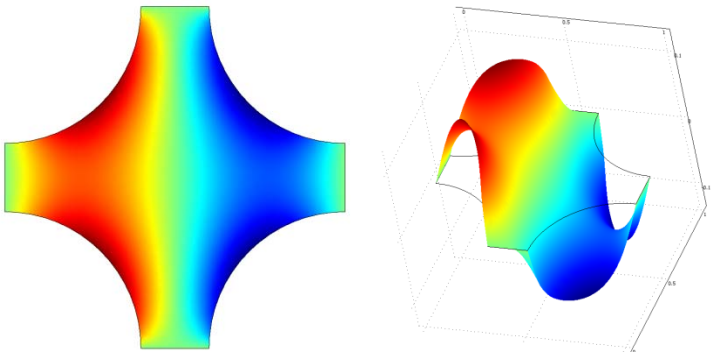

Figure 5.13 Characteristic concentration distribution in the pore domain. Volume averaging gives the effective diffusivity.

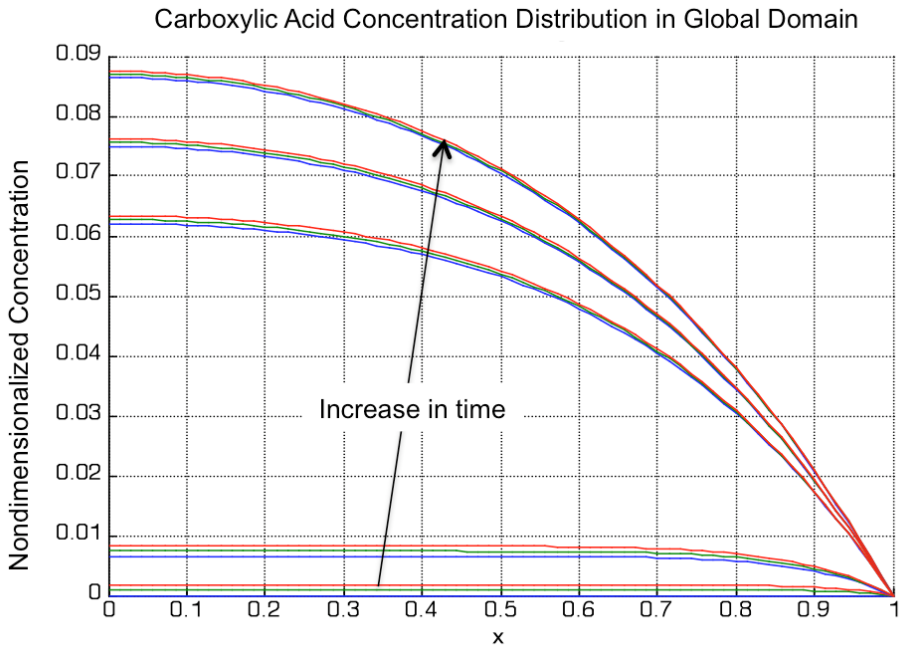

Figure 5.14 The change of distribution of carboxlyic acid end group concentrations were plotted at different time points. Note that at x=0, acid concentration is maximum while its time derivative is zero. Also note that at x=1, acid concentration is zero while its time derivative is maximum.

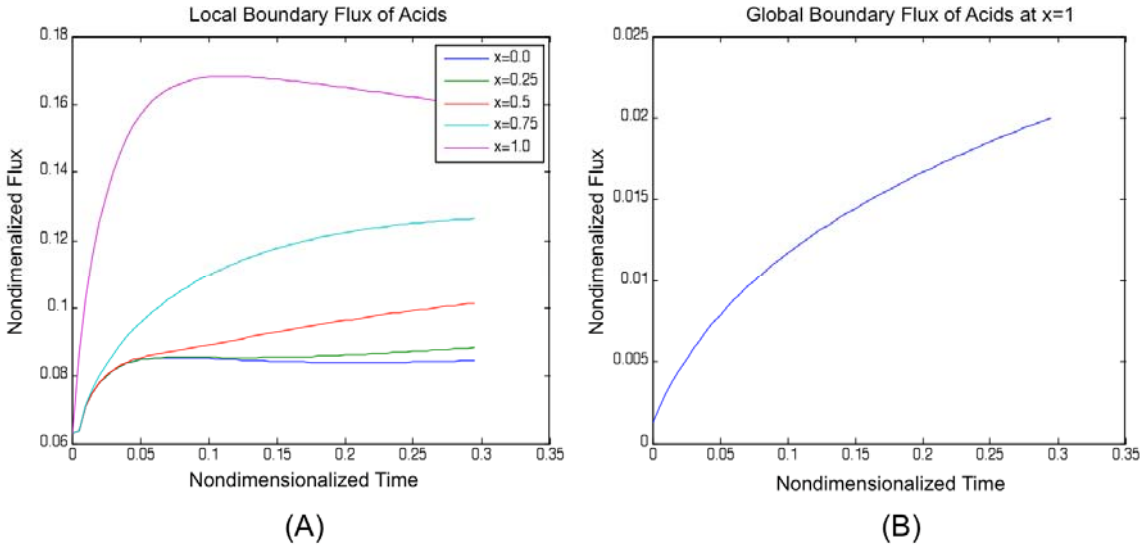

Figure 5.15 (A) Nondimensionalized efflux of carboxylic acid end groups at five representative unit microstructures were plotted as the simulation time. (B) Nondimensionalized efflux of carboxylic acid end groups at the boundary (x=1) of the global domain.

Figure 5.14 illustrates the change of distribution of carboxlyic acid end group concentration over different time points. It should be noted that at x=0, acid concentration is maximum while its time derivative is zero. Also note that at x=1, acid concentration is zero while its time derivative is maximum. These quantities are important because they affect the local boundary fluxes at different locations, which in turn affects the global quantities.

Figure 5.15 shows the time course of local acid end group flux at the solid-void boundary and the global acid end group flux at the global domain boundary (x=1). The profiles of local acid fluxes were different at different locations because of the effect of global concentration and its time derivative. It should be noted that the global flux was delayed compared to local acid flux at x=1. In the degradation of the bulk polymer matrix in section 5.2.2, similar delayed acid release was in Figure 5.6. With the presence of microstructures, delayed release occurred twice, locally and globally. This indicates that the design of microstructures may control the degradation of the porous scaffolds. Obviously, this argument needs further quantitative evaluations.

Figure 5.16 and Figure 5.17 illustrate the molecular weight profile and mass loss. The molecular weight profile was assumed to be proportional to ester bond concentrations within the polymer matrix, whereas the mass loss was measured as the cumulative release of carboxylic acid end groups. Both demonstrated typical degradation behavior. Although the current multiscale model assumes only one case – the high diffusion contrast between solid and pore, it may provide a more accurate prediction for the degradation of hierarchical scaffolds with the same order of diffusivity of acids in both pore space and polymer matrix.

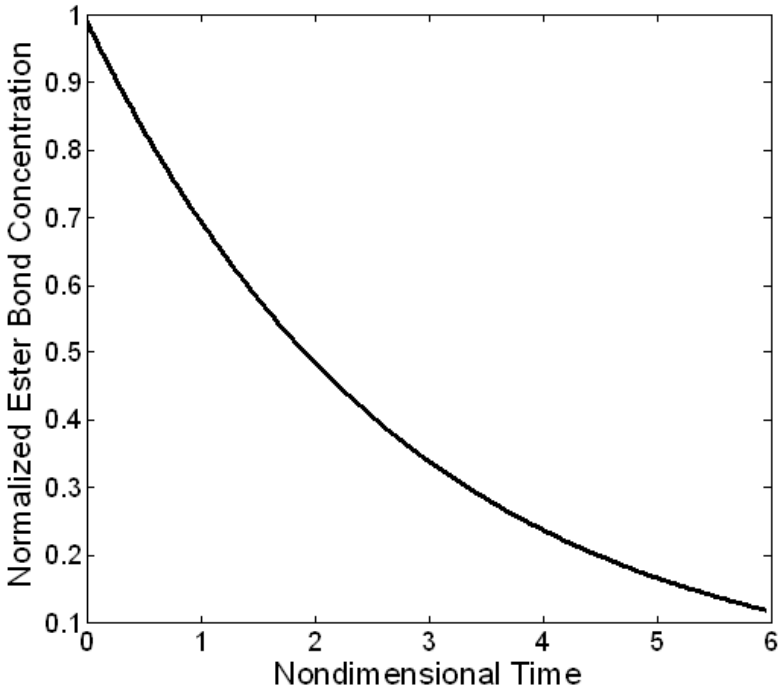

Figure 5.16 Normalized ester bond concentration (molecular weight profile) within the polymer matrix (solid region of porous scaffold) was demonstrated for k_1=0.35, k_2=0.1, D^H=0.343, and D_2=1.0.

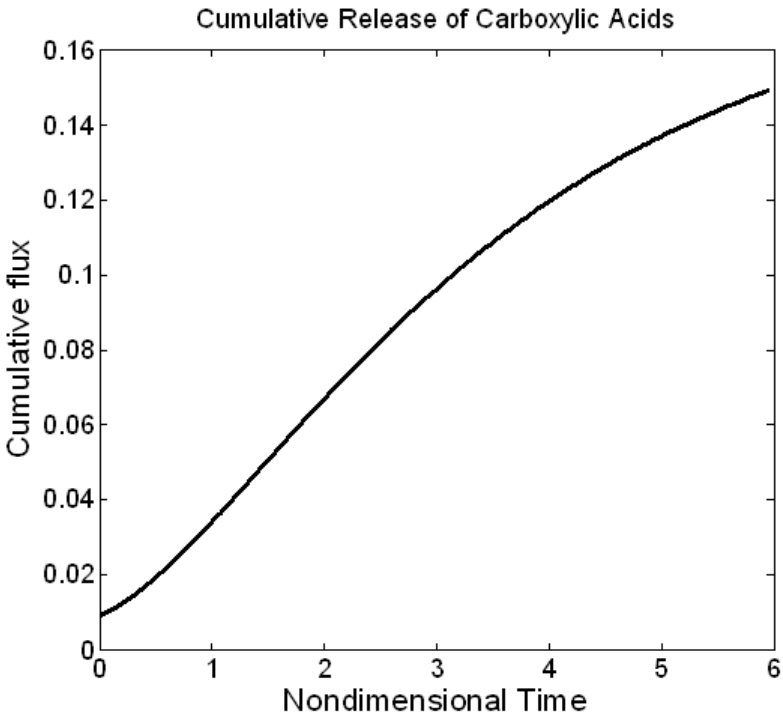

Figure 5.17 The cumulative efflux from the outer surface of the infinite plate (x=1).

5.4 Conclusion and Future Work

We were able to successfully demonstrate the hydrolytic degradation of hierarchical scaffolds made of biodegradable polyesters. Based on simple diffusion reaction equations, the complex processes during polymer degradation and erosion were qualitatively characterized, providing an important tool for the design of tissue engineering scaffolds involving degradation. For example, the nondimensional parameter for the ratio of hydrolysis reaction time to water diffusion can provide a rough idea of suitable biomaterials and device size. Furthermore, this tool makes it possible to predict the failure of implanted device with specific dimensions by using the nondimensional parameters accounting for the interplay between the hydrolysis reaction and the acidic product diffusion.

In the hierarchical tissue scaffolds, the above-mentioned phenomena are largely affected by pore architecture, including pore size, strut size, pore shape, and related functional properties. In order to investigate the effects of microstructures, a multiscale homogenization method was derived and applied to the hydrolysis reaction and carboxylic acid release. In this study, the effects of the microstructure on the release of carboxylic acid end groups, or small polymer chains, were investigated. However, this model needs further quantitative investigations in addition to comparisons between scaffolds with different pore architectures. Finally, to adequately predict device failure time *in vivo*, the model should address the changes of the mechanical properties along with the degradation. Additional validation of the current multi-scale model is required to provide necessary insight into the role of complex pore architecture on the ultimate

performance of hierarchical scaffolds. The elaborated validation of current multiscale model will further extend the knowledge of how the complex pore architecture finally affects the performance of the hierarchical scaffolds.

CHAPTER 6

CONCLUSION

6.1 Summary and Conclusion

As a multifunctional composite biomaterial, tissue engineering scaffolds need to be tailored to satisfy the properties and functions of healthy tissue, as well as maintain the desired function throughout tissue healing to ensure optimal tissue regeneration. In order to design a hierarchical scaffold that can meet these requirements, a systemic design framework employing the homogenization method and topology optimization may be required.

To design a hierarchical scaffold that can meet these requirements, a systemic design framework employing the homogenization method to characterize hierarchical scaffold design is invaluable. Characterizing the scaffold's mechanical and mass transport properties ensures a truly representative design framework. Because tissue functions are best represented by these properties, the scaffold properties should be tailored to match the properties of healthy tissues. The characterization method should consider the effect of pore architecture, which has been correlated to both tissue regeneration and scaffold performance. The design framework should also produce a pore

architecture that achieves prescribed mechanical and mass transport properties. For given design requirements, designers do not know the corresponding a priori de novo pore structures that give rise to specific effective properties. Structural optimization techniques such as topology optimization can provide versatile option in this case.

To elucidate the effects of scaffold design parameters on tissue regeneration, Solid freeform fabrication offers the best option for building the necessary complex 3D architecture with sufficient accuracy and reproducibility. Controlled pore architectures could be accurately reproduced in this study with consistent mechanical and mass transport properties, which will allow the verification of the design by in vitro and in vivo experiments. Without a proper fabrication method, it is not possible to correlate the designed properties to tissue regeneration.

Finally, the design framework should be able to address the changes of the designed properties accompanying scaffold degradation that are so critical to preventing premature scaffold failure and promoting appropriate regeneration of the target tissue. Although a scaffold is designed with tailored mechanical and mass transport properties, it starts degradation from in vitro culture throughout in vivo implantation. Thus, it is likely that the scaffold cannot provide sufficient function as designed. With the computational models for hydrolytic degradation, further controlling parameters can be identified to modify the original designs. With multiscale modeling techniques, more rigorous correlation can be obtained between pore architecture and degradation properties.

To implement and test the design framework for the hierarchical scaffolds, we presented in this work that the microstructure design with tailored mechanical and mass

transport properties, the design of porous biodegradable fusion cage using the integrated global-local topology optimization, and computational simulation of scaffold degradation.

As tissue function is characterized with mechanical stiffness, so the scaffold function was characterized by homogenization of elasticity. Good correlation was obtained between experimental and predicted moduli. To facilitate and control tissue ingrowth and biologic delivery, the effective diffusivity and permeability were calculated with the homogenization of diffusion and the homogenization of Stokes equation. Microstructures with tailored mechanical and mass transport properties were obtained by optimizing bulk modulus and diffusivity concurrently in a multiobjective formulation. Designed microstructures were optimal as they are on or close to theoretical upper bounds, indicating that both mechanical and mass transport properties are maximized.

As an example of the clinical application of the microstructural topology optimization, we also presented a porous inter-body fusion cage design using a global-local integerated topology optimization technique (Lin et al. 2004) that demonstrated sufficient mechanical properties to support lumbar inter-body loads. The integrated global-local topology optimization combined with SFF technique in PCL and HA is a promising method for the design of biodegradable fusion cages because it can produce a porous structure with optimal mechanical and mass transport properties. . Based on experimental and computational verification, optimally designed PCL cages have sufficient mechanical properties to support lumbar interbody loads. This combined with the longer degradation period of PCL may breathe more life into the solution of bio-resorbable cages for spinal fusion applications.

Finally, an effective mathematical model of porous biodegradable scaffold based on diffusion-reaction equations and multi-scale homogenization was demonstrated. Complex phenomena observed during polymer degradation were first demonstrated using diffusion-reaction equations. Then a multi-scale homogenization method was adapted to investigate the effects of a microstructure on the degradation profile. Because of the coupling in time and space in the homogenized equation, a solution method was proposed to approximate the continuum problem at discrete sampling points. Macroscopic acid release was demonstrated to follow the microscopic acid release into pore space. Combining the observations from the single scale and multiscale diffusion-reaction systems, different acid release profiles are expected.

6.2 Future Study

The homogenization method provides a theoretical background in the design of hierarchical scaffolds. However, the practical size of scaffold specimen is limited by the resolution of fabrication technique. Using PCL and HA powders, the smallest hole the selective laser sintering machine in this study could build is 800 um. The dimension of the scaffold, typically adopted in animal studies, is as small as 5 mm. In some cases the scale may not provide sufficient separation to apply the homogenization theory to? the design. However, the inclusion of higher order terms as correctors may compensate for the errors in such cases.

Microstructure design using topology optimization can be extended using other techniques for suppressing numerical instabilities such as perimeter control. One of the possible applications of optimal microstructures in the inter-body fusion would be

controlled release of biologics such as BMP2. In general, BMP2 related complications are attributed to the initial burst of release, which can cause adverse reactions at the surrounding soft tissues. An alternative approach is to deliver BMP2 requires high surface area for prolonged release (chapter 4). To this end, perimeter control or surface area control schemes commonly adapted in the topology optimization can be used to optimally control the release of such biologics.

For the fusion cage, a multilevel optimization technique was utilized to obtain maximum stiffness and permeability design. As a first step, we separated the multiscale problem into global and local scale problems, by solving a minimum compliance problem at a macroscopic scale and then applying optimized microstructures. In fact, the later applied microstructures can alter the originally designed global property. As proposed by Coelho et al. this may be avoided by solving the two scale problem simultaneously. At each time point, material density at the global domain serves as a volume fraction constraint in the local cell problems. The local cell problems are solved to provide the effective properties for the global problem. In this way, the alteration of properties will desist as the algorithm converges.

The multiscale modeling of hydrolytic degradation was proposed in this study based on the homogenization of diffusion reaction equations. Although the derivation followed a theoretically proven method, it remains to be challenged by actual application, requiring quantitative experimental validation, both in vitro and in vivo. Comparative studies of scaffolds with different pore architectures are also required for what reasons?

Finally, to predict the device failure time critical to scaffold success in high load bearing applications, the model should incorporate values for mechanical properties

garnered experimentally. Experimental measurements for hierarchically designed scaffolds will provide ultimate validation of our proposed model. In short, a single unifying theoretical framework embodying precise characterization of scaffolds, together with controlled design and fabrication, can provide the critical correlation between scaffold design parameters and tissue regeneration necessary for successful, tailored constructs.

BIBLIOGRAPHY

Adachi, T., Y. Osako, et al. (2006). "Framework for optimal design of porous scaffold microstructure by computational simulation of bone regeneration." Biomaterials **27**(21): 3964-3972.

Anderson, A. R. A. and M. A. J. Chaplain (1998). "A mathematical model for capillary network formation in the absence of endothelial cell proliferation." Applied Mathematics Letters **11**(3): 109-114.

Ang, K. C., K. F. Leong, et al. (2007). "Compressive properties and degradability of poly(epsilon-caprolatone)/hydroxyapatite composites under accelerated hydrolytic degradation." Journal of Biomedical Materials Research Part A **80A**(3): 655-660.

Antheunis, H., J. C. van der Meer, et al. (2009). "Improved Mathematical Model for the Hydrolytic Degradation of Aliphatic Polyesters." Macromolecules **42**(7): 2462-2471.

Aoki, Y., M. Yamagata, et al. (2009). "Posterior migration of fusion cages in degenerative lumbar disease treated with transforaminal lumbar interbody fusion: a report of three patients." Spine (Phila Pa 1976) **34**(1): E54-58.

Aronin, C. E. P., K. W. Sadik, et al. (2009). "Comparative effects of scaffold pore size, pore volume, and total void volume on cranial bone healing patterns using microsphere-based scaffolds." Journal of Biomedical Materials Research Part A **89A**(3): 632-641.

Auriault, J. L., C. Boutin, et al. (2009). Homogenization of coupled phenomena in heterogenous media. London, UK, J. Wiley.

Auriault, J. L., C. Geindreau, et al. (2005). "Filtration law in porous media with poor separation of scales." Transport in Porous Media **60**(1): 89-108.

Auriault, J. L. and J. Lewandowska (1995). "Non-gaussian diffusion modeling in composite porous media by homogenization: Tail effect." Transport in Porous Media **21**(1): 47-70.

Auriault, J. L. and J. Lewandowska (2001). "Upscaling: Cell symmetries and scale separation." Transport in Porous Media **43**(3): 473-485.

Avellaneda, M. and S. Torquato (1991). "Rigorous Link between Fluid Permeability, Electrical-Conductivity, and Relaxation-Times for Transport in Porous-Media." Physics of Fluids a-Fluid Dynamics **3**(11): 2529-2540.

Bagby, G. W. (1988). "Arthrodesis by the distraction-compression method using a stainless steel implant." Orthopedics **11**(6): 931-934.

Bendsøe, M. P. (1989). "Optimal shape design as a material distribution problem." Structural and Multidisciplinary Optimization **1**(4): 193-202.

Bendsoe, M. P. and N. Kikuchi (1988). "Generating Optimal Topologies in Structural Design Using a Homogenization Method." Computer Methods in Applied Mechanics and Engineering **71**(2): 197-224.

Bendsoe, M. P. and O. Sigmund (1999). "Material interpolation schemes in topology optimization." Archive of Applied Mechanics **69**(9-10): 635-654.

Bensoussan, A., J. L. Lions, et al. (1978). Asymptotic analysis for periodic structures. New York, North-Holland Pub. Co.

Boschetti, F., G. Pennati, et al. (2004). "Biomechanical properties of human articular cartilage under compressive loads." Biorheology **41**(3-4): 159-166.

Brand, R. A. (1992). "Autonomous informational stability in connective tissues." Med Hypotheses **37**(2): 107-114.

Brantigan, J. W. and A. D. Steffee (1993). "A carbon fiber implant to aid interbody lumbar fusion. Two-year clinical results in the first 26 patients." Spine (Phila Pa 1976) **18**(14): 2106-2107.

Challis, V. J., A. P. Roberts, et al. (2008). "Design of three dimensional isotropic microstructures for maximized stiffness and conductivity." International Journal of Solids and Structures **45**(14-15): 4130-4146.

Chen, L., H. Yang, et al. (2005). "Cage migration in spondylolisthesis treated with posterior lumbar interbody fusion using BAK cages." Spine (Phila Pa 1976) **30**(19): 2171-2175.

Chen, N. F., Z. A. Smith, et al. (2010). "Symptomatic ectopic bone formation after off-label use of recombinant human bone morphogenetic protein-2 in transforaminal lumbar interbody fusion." J Neurosurg Spine **12**(1): 40-46.

Cherkaev, A. V. and L. V. Gibiansky (1993). "Coupled Estimates for the Bulk and Shear Moduli of a 2-Dimensional Isotropic Elastic Composite." Journal of the Mechanics and Physics of Solids **41**(5): 937-980.

Cizek, G. R. and L. M. Boyd (2000). "Imaging pitfalls of interbody spinal implants." Spine (Phila Pa 1976) **25**(20): 2633-2636.

Cunningham, B. W., C. M. Orbegoso, et al. (2003). "The effect of spinal instrumentation particulate wear debris, , : an in vivo rabbit model and applied clinical study of retrieved instrumentation cases." The Spine Journal **3**(1): 19-32.

Cyster, L. A., D. M. Grant, et al. (2005). "The influence of dispersant concentration on the pore morphology of hydroxyapatite ceramics for bone tissue engineering." Biomaterials **26**(7): 697-702.

de Kruijf, N., S. W. Zhou, et al. (2007). "Topological design of structures and composite materials with multiobjectives." International Journal of Solids and Structures **44**(22-23): 7092-7109.

Demarteau, O., L. Pillet, et al. (2006). "Biomechanical characterization and in vitro mechanical injury of elderly human femoral head cartilage: comparison to adult bovine humeral head cartilage." Osteoarthritis Cartilage **14**(6): 589-596.

Deyo, R. A., D. T. Gray, et al. (2005). "United States trends in lumbar fusion surgery for degenerative conditions." Spine (Phila Pa 1976) **30**(12): 1441-1445; discussion 1446-1447.

Diaz, A. R. and N. Kikuchi (1992). "Solutions to Shape and Topology Eigenvalue Optimization Problems Using a Homogenization Method." International Journal for Numerical Methods in Engineering **35**(7): 1487-1502.

Ekstrom, L., S. Holm, et al. (2004). "In vivo porcine intradiscal pressure as a function of external loading." Journal of Spinal Disorders & Techniques **17**(4): 312-316.

Engelberg, I. and J. Kohn (1991). "Physico-mechanical properties of degradable polymers used in medical applications: a comparative study." Biomaterials **12**(3): 292-304.

Eshraghi, S. and S. Das (2010). "Mechanical and microstructural properties of polycaprolactone scaffolds with one-dimensional, two-dimensional, and three-dimensional orthogonally oriented porous architectures produced by selective laser sintering." Acta Biomaterialia **6**(7): 2467-2476.

Gersborg-Hansen, A., M. P. Bendsoe, et al. (2006). "Topology optimization of heat conduction problems using the finite volume method." Structural and Multidisciplinary Optimization **31**(4): 251-259.

Gersborg-Hansen, A., O. Sigmund, et al. (2005). "Topology optimization of channel flow problems." Structural and Multidisciplinary Optimization **30**(3): 181-192.

Gibiansky, L. V. and S. Torquato (1993). "Link between the Conductivity and Elastic-Moduli of Composite-Materials." Physical Review Letters **71**(18): 2927-2930.

Gibiansky, L. V. and S. Torquato (1995). "Rigorous Link between the Conductivity and Elastic-Moduli of Fiber-Reinforced Composite-Materials." Philosophical Transactions of the Royal Society of London Series a-Mathematical Physical and Engineering Sciences **353**(1702): 243-278.

Gibiansky, L. V. and S. Torquato (1996). "Connection between the conductivity and bulk modulus of isotropic composite materials." Proceedings of the Royal Society of London Series a-Mathematical Physical and Engineering Sciences **452**(1945): 253-283.

Goel, V. K. and L. G. Gilbertson (1997). "Basic science of spinal instrumentation." Clin Orthop Relat Res(335): 10-31.

Gopferich, A. (1997). "Erosion of composite polymer matrices." Biomaterials **18**(5): 397-403.

Gopferich, A. and R. Langer (1993). "Modeling of Polymer Erosion." Macromolecules **26**(16): 4105-4112.

Goulet, R. W., S. A. Goldstein, et al. (1994). "The relationship between the structural and orthogonal compressive properties of trabecular bone." J Biomech **27**(4): 375-389.

Grizzi, I., H. Garreau, et al. (1995). "Hydrolytic degradation of devices based on poly(DL-lactic acid) size-dependence." Biomaterials **16**(4): 305-311.

Guest, J. K. (2005). Design of Optimal Porous Material Structures for Maximized Stiffness and Permeability using Topology Optimization and Finite Element Methods. Department of Civil and Environmental Engineering, Princeton University. **PhD**.

Guest, J. K. and J. H. Prevost (2006). "Optimizing multifunctional materials: Design of microstructures for maximized stiffness and fluid permeability." International Journal of Solids and Structures **43**(22-23): 7028-7047.

Guest, J. K. and J. H. Prevost (2006). "Topology optimization of creeping fluid flows using a Darcy-Stokes finite element." International Journal for Numerical Methods in Engineering **66**(3): 461-484.

Guest, J. K., J. H. Prevost, et al. (2004). "Achieving minimum length scale in topology optimization using nodal design variables and projection functions." International Journal for Numerical Methods in Engineering **61**(2): 238-254.

Hashin, Z. and S. Shtrikman (1962). "A Variational Approach to Theory of Effective Magnetic Permeability of Multiphase Materials." Journal of Applied Physics **33**(10): 3125-&.

Hashin, Z. and S. Shtrikman (1963). "A Variational Approach to the Theory of the Elastic Behaviour of Multiphase Materials." Journal of the Mechanics and Physics of Solids **11**(2): 127-140.

Hassani, B. (1996). "A direct method to derive the boundary conditions of the homogenization equation for symmetric cells." Communications in Numerical Methods in Engineering **12**(3): 185-196.

Hollister, S. J. (2005). "Porous scaffold design for tissue engineering." Nat Mater **4**(7): 518-524.

Hollister, S. J. and N. Kikuchi (1992). "A comparison of homogenization and standard mechanics analyses for periodic porous composites." Computational Mechanics **10**(2): 73-95.

Hollister, S. J., R. A. Levy, et al. (2000). "An image-based approach for designing and manufacturing craniofacial scaffolds." Int J Oral Maxillofac Surg **29**(1): 67-71.

Hollister, S. J., E. E. Liao, et al. (2009). Defining Design Targets for Tissue Engineering Scaffolds**:** 521-537.

Hollister, S. J., C.-Y. Lin, et al. (2008). Computational Design and Simulation of Tissue Engineering Scaffolds. Virtual Prototyping & Bio Manufacturing in Medical Applications. B. Bidanda and P. J. Bartolo, Springer**:** 113-127.

Hollister, S. J. and C. Y. Lin (2007). "Computational design of tissue engineering scaffolds." Computer Methods in Applied Mechanics and Engineering **196**(31-32): 2991-2998.

Hollister, S. J., R. D. Maddox, et al. (2002). "Optimal design and fabrication of scaffolds to mimic tissue properties and satisfy biological constraints." Biomaterials **23**(20): 4095-4103.

Hughes, T. J. R., L. P. Franca, et al. (1986). "A new finite-element formulation for computational fluid-dynamics .5. Circumventing the babuska-brezzi condition - a stable petrov-galerkin formulation of the stokes problem accommodating equal-order interpolations." Computer Methods in Applied Mechanics and Engineering **59**(1): 85-99.

Hutmacher, D. W. (2000). "Scaffolds in tissue engineering bone and cartilage." Biomaterials **21**(24): 2529-2543.

Hutmacher, D. W. (2001). "Scaffold design and fabrication technologies for engineering tissues--state of the art and future perspectives." J Biomater Sci Polym Ed **12**(1): 107-124.

Jiya, T., T. Smit, et al. (2009). "Posterior lumbar interbody fusion using nonresorbable poly-ether-ether-ketone versus resorbable poly-L-lactide-co-D,L-lactide fusion devices: a prospective, randomized study to assess fusion and clinical outcome." Spine (Phila Pa 1976) **34**(3): 233-237.

Kanayama, M., B. W. Cunningham, et al. (2000). "In vitro biomechanical investigation of the stability and stress-shielding effect of lumbar interbody fusion devices." J Neurosurg **93**(2 Suppl): 259-265.

Kandziora, F., R. Pflugmacher, et al. (2004). "Bioabsorbable interbody cages in a sheep cervical spine fusion model." Spine (Phila Pa 1976) **29**(17): 1845-1855; discussion 1856.

Kang, H., C.-Y. Lin, et al. (2010). "Topology optimization of three dimensional tissue engineering scaffold architectures for prescribed bulk modulus and diffusivity." Structural and Multidisciplinary Optimization **42**(4): 633-644.

Karageorgiou, V. and D. Kaplan (2005). "Porosity of 3D biomaterial scaffolds and osteogenesis." Biomaterials **26**(27): 5474-5491.

Karjalainen, T., M. HiljanenVainio, et al. (1996). "Biodegradable lactone copolymers .3. Mechanical properties of epsilon-caprolactone and lactide copolymers after hydrolysis in vitro." Journal of Applied Polymer Science **59**(8): 1299-1304.

Kemppainen, J. M. and S. J. Hollister (2010). "Differential effects of designed scaffold permeability on chondrogenesis by chondrocytes and bone marrow stromal cells." Biomaterials **31**(2): 279-287.

Kim, B. S. and D. J. Mooney (1998). "Development of biocompatible synthetic extracellular matrices for tissue engineering." Trends Biotechnol **16**(5): 224-230.

Kuboki, Y., H. Takita, et al. (1998). "BMP-induced osteogenesis on the surface of hydroxyapatite with geometrically feasible and nonfeasible structures: topology of osteogenesis." J Biomed Mater Res **39**(2): 190-199.

Kuslich, S. D., C. L. Ulstrom, et al. (1998). "The Bagby and Kuslich Method of Lumbar Interbody Fusion: History, Techniques, and 2-Year Follow-up Results of a United States Prospective, Multicenter Trial." Spine **23**(11): 1267-1278.

Langer, R. and J. P. Vacanti (1993). "Tissue engineering." Science **260**(5110): 920-926.

Lee, C. K., C. C. Sun, et al. (1996). "Computation of permeability and dispersivities of solute or heat in periodic porous media." International Journal of Heat and Mass Transfer **39**(4): 661-676.

Li, S. M., H. Garreau, et al. (1990). "Structure-property relationships in the case of the degradation of massive poly(α-hydroxy acids) in aqueous media." Journal of Materials Science: Materials in Medicine **1**(3): 131-139.

Liebschner, M. A. K. and M. A. Wettergreen (2003). Optimization of Bone Scaffold Engineering for Load Bearing Applications.

Lin, C. Y., C. C. Hsiao, et al. (2004). "Interbody fusion cage design using integrated global layout and local microstructure topology optimization." Spine (Phila Pa 1976) **29**(16): 1747-1754.

Lin, C. Y., N. Kikuchi, et al. (2004). "A novel method for biomaterial scaffold internal architecture design to match bone elastic properties with desired porosity." J Biomech **37**(5): 623-636.

Lin, C. Y., R. M. Schek, et al. (2005). "Functional bone engineering using ex vivo gene therapy and topology-optimized, biodegradable polymer composite scaffolds." Tissue Eng **11**(9-10): 1589-1598.

Lin, C. Y., T. Wirtz, et al. (2007). "Structural and mechanical evaluations of a topology optimized titanium interbody fusion cage fabricated by selective laser melting process." J Biomed Mater Res A **83**(2): 272-279.

Lin, R. M., K. H. Tsai, et al. (1997). "Distribution and regional strength of trabecular bone in the porcine lumbar spine." Clin Biomech (Bristol, Avon) **12**(5): 331-336.

Lyu, S., R. Sparer, et al. (2005). "Analytical solutions to mathematical models of the surface and bulk erosion of solid polymers." Journal of Polymer Science Part B-Polymer Physics **43**(4): 383-397.

Lyu, S. and D. Untereker (2009). "Degradability of Polymers for Implantable Biomedical Devices." International Journal of Molecular Sciences **10**(9): 4033-4065.

Malda, J., D. E. Martens, et al. (2003). "Cartilage tissue engineering: controversy in the effect of oxygen." Crit Rev Biotechnol **23**(3): 175-194.

Malda, J., T. B. F. Woodfield, et al. (2004). "The effect of PEGT/PBT scaffold architecture on oxygen gradients in tissue engineered cartilaginous constructs." Biomaterials **25**(26): 5773-5780.

McAfee, P. C. (1999). "Interbody fusion cages in reconstructive operations on the spine." J Bone Joint Surg Am **81**(6): 859-880.

Mikos, A. G., M. D. Lyman, et al. (1994). "Wetting of poly(L-lactic acid) and poly(DL-lactic-co-glycolic acid) foams for tissue culture." Biomaterials **15**(1): 55-58.

Milroy, G. E., R. W. Smith, et al. (2003). "The Degradation of Polyglycolide in Water and Deuterium Oxide. Part II: Nuclear Reaction Analysis and Magnetic Resonance Imaging of Water Distribution." Polymer **44**(5): 1425-1435.

Mooney, D. J., D. F. Baldwin, et al. (1996). "Novel approach to fabricate porous sponges of poly(D,L-lactic-co-glycolic acid) without the use of organic solvents." Biomaterials **17**(14): 1417-1422.

Murphy, W. L., D. H. Kohn, et al. (2000). "Growth of continuous bonelike mineral within porous poly(lactide-co-glycolide) scaffolds in vitro." J Biomed Mater Res **50**(1): 50-58.

Nachemson, A. (1966). "The load on lumbar disks in different positions of the body." Clin Orthop Relat Res **45**: 107-122.

Pankratov, L., A. Piatnitskii, et al. (2003). "Homogenized model of reaction-diffusion in a porous medium." Comptes Rendus Mecanique **331**(4): 253-258.

Pedersen, C. B. W. (2004). "Crashworthiness design of transient frame structures using topology optimization." Computer Methods in Applied Mechanics and Engineering **193**(6-8): 653-678.

Pitt, C. G., F. I. Chasalow, et al. (1981). "Aliphatic polyesters 1. The degradation of poly(epsilon-caprolactone) in vivo." Journal of Applied Polymer Science **26**(11): 3779-3787.

Pitt, C. G. and Z. W. Gu (1987). "Modification of the rates of chain cleavage of poly-epsilon-caprolactone and related polyesters in the solid state." Journal of Controlled Release **4**(4): 283-292.

Ray, C. D. (1997). "Threaded titanium cages for lumbar interbody fusions." Spine (Phila Pa 1976) **22**(6): 667-679; discussion 679-680.

Robertson, D. D., G. B. Sharma, et al. (2009). "Bone Densitometry Within Titanium Lumbar Interbody Fusion Cages A Computed Tomography Feasibility Study." Spine **34**(25): 2792-2796.

Roosa, S. M., J. M. Kemppainen, et al. (2010). "The pore size of polycaprolactone scaffolds has limited influence on bone regeneration in an in vivo model." J Biomed Mater Res A **92**(1): 359-368.

Rothstein, S. N., W. J. Federspiel, et al. (2009). "A unified mathematical model for the prediction of controlled release from surface and bulk eroding polymer matrices." Biomaterials **30**(8): 1657-1664.

Saito, E., H. Kang, et al. (2010). "Experimental and computational characterization of designed and fabricated 50:50 PLGA porous scaffolds for human trabecular bone applications." Journal of Materials Science: Materials in Medicine **21**(8): 2371-2383.

Sanchez-Palencia, E., A. Zaoui, et al. (1987). Homogenization techniques for composite media : lectures delivered at the CISM International Center for Mechanical Sciences, Udine, Italy, July 1-5, 1985. Berlin ; New York, Springer-Verlag.

Schek, R. M., J. M. Taboas, et al. (2005). "Tissue engineering osteochondral implants for temporomandibular joint repair." Orthod Craniofac Res **8**(4): 313-319.

Schultz, A., G. Andersson, et al. (1982). "Loads on the lumbar spine. Validation of a biomechanical analysis by measurements of intradiscal pressures and myoelectric signals." J Bone Joint Surg Am **64**(5): 713-720.

Shiraziadl, A., A. M. Ahmed, et al. (1986). "A Finite-Element Study of a Lumbar Motion Segment Subjected to Pure Sagittal Plane Moments." Journal of Biomechanics **19**(4): 331-350.

Shor, L., S. Gueceri, et al. (2008). "Solid freeform fabrication of polycaprolactone/hydroxyapatite tissue scaffolds." Journal of Manufacturing Science and Engineering-Transactions of the Asme **130**(2): -.

Sigmund, O. (1994). Design of material structures using topology optimization, Technical University of Denmark. **PhD**.

Sigmund, O. (1994). "Materials with Prescribed Constitutive Parameters - an Inverse Homogenization Problem." International Journal of Solids and Structures **31**(17): 2313-2329.

Sigmund, O. (1994). "Tailoring Materials for Specific Needs." Journal of Intelligent Material Systems and Structures **5**(6): 736-742.

Sigmund, O. (1995). "Tailoring Materials with Prescribed Elastic Properties." Mechanics of Materials **20**(4): 351-368.

Sigmund, O. (2001). "Design of multiphysics actuators using topology optimization - Part I: One-material structures." Computer Methods in Applied Mechanics and Engineering **190**(49-50): 6577-6604.

Sigmund, O. and J. Petersson (1998). "Numerical instabilities in topology optimization: A survey on procedures dealing with checkerboards, mesh-dependencies and local minima." Structural Optimization **16**(1): 68-75.

Simmons, C. A., S. A. Meguid, et al. (2001). "Differences in osseointegration rate due to implant surface geometry can be explained by local tissue strains." Journal of Orthopaedic Research **19**(2): 187-194.

Siparsky, G. L., K. J. Voorhees, et al. (1998). "Hydrolysis of polylactic acid (PLA) and polycaprolactone (PCL) in aqueous acetonitrile solutions: Autocatalysis." Journal of Environmental Polymer Degradation **6**(1): 31-41.

Smit, T. H. (2002). "The use of a quadruped as an in vivo model for the study of the spine - biomechanical considerations." Eur Spine J **11**(2): 137-144.

Smit, T. H., T. A. Engels, et al. (2008). "Time-dependent mechanical strength of 70/30 Poly(L, DL-lactide): shedding light on the premature failure of degradable spinal cages." Spine (Phila Pa 1976) **33**(1): 14-18.

Smit, T. H., M. R. Krijnen, et al. (2006). "Application of polylactides in spinal cages: studies in a goat model." J Mater Sci Mater Med **17**(12): 1237-1244.

Smith, K. R., T. R. Hunt, et al. (1991). "The effect of a stiff spinal implant on the bone-mineral content of the lumbar spine in dogs." J Bone Joint Surg Am **73**(1): 115-123.

Svanberg, K. (1987). "The Method of Moving Asymptotes - a New Method for Structural Optimization." International Journal for Numerical Methods in Engineering **24**(2): 359-373.

Taboas, J. M., R. D. Maddox, et al. (2003). "Indirect solid free form fabrication of local and global porous, biomimetic and composite 3D polymer-ceramic scaffolds." Biomaterials **24**(1): 181-194.

Takahashi, I., S. Kikuchi, et al. (2006). "Mechanical load of the lumbar spine during forward bending motion of the trunk-a biomechanical study." Spine (Phila Pa 1976) **31**(1): 18-23.

Thomson, R. C., M. J. Yaszemski, et al. (1995). "Fabrication of biodegradable polymer scaffolds to engineer trabecular bone." J Biomater Sci Polym Ed **7**(1): 23-38.

Torquato, S. (2002). Random Heterogeneous Materials: microstructure and macroscopic properties. New York, Springer.

Torquato, S., S. Hyun, et al. (2003). "Optimal design of manufacturable three-dimensional composites with multifunctional characteristics." Journal of Applied Physics **94**(9): 5748-5755.

Ueda, H. and Y. Tabata (2003). "Polyhydroxyalkanonate derivatives in current clinical applications and trials." Advanced Drug Delivery Reviews **55**(4): 501-518.

Vaccaro, A. R., K. Singh, et al. (2003). "The use of bioabsorbable implants in the spine." The Spine Journal **3**(3): 227-237.

van Dijk, M., T. H. Smit, et al. (2003). "The use of poly-L-lactic acid in lumbar interbody cages: design and biomechanical evaluation in vitro." European Spine Journal **12**(1): 34-40.

van Dijk, M., T. H. Smit, et al. (2002). "Bioabsorbable poly-L-lactic acid cages for lumbar interbody fusion: three-year follow-up radiographic, histologic, and histomorphometric analysis in goats." Spine (Phila Pa 1976) **27**(23): 2706-2714.

van Dijk, M., T. H. Smit, et al. (2002). "The effect of cage stiffness on the rate of lumbar interbody fusion: an in vivo model using poly(l-lactic Acid) and titanium cages." Spine (Phila Pa 1976) **27**(7): 682-688.

van Dijk, M., P. J. van Diest, et al. (2005). "Four-year follow-up of poly-L-lactic Acid cages for lumbar interbody fusion in goats." J Long Term Eff Med Implants **15**(2): 125-138.

Vert, M., S. M. Li, et al. (1994). "Attempts to map the structure and degradation characteristics of aliphatic polyesters derived from lactic and glycolic acids." J Biomater Sci Polym Ed **6**(7): 639-649.

von Burkersroda, F., L. Schedl, et al. (2002). "Why degradable polymers undergo surface erosion or bulk erosion." Biomaterials **23**(21): 4221-4231.

Wang, M. Y., S. Zhou, et al. (2004). "Nonlinear diffusions in topology optimization." Structural and Multidisciplinary Optimization **28**(4): 262-276.

Wang, Y., J. Pan, et al. (2008). "A phenomenological model for the degradation of biodegradable polymers." Biomaterials **29**(23): 3393-3401.

Weiner, B. K. and R. D. Fraser (1998). "Spine update lumbar interbody cages." Spine (Phila Pa 1976) **23**(5): 634-640.

Whang, K., C. H. Thomas, et al. (1995). "A Novel Method to Fabricate Bioabsorbable Scaffolds." Polymer **36**(4): 837-842.

Whitecloud, T. S., 3rd, F. P. Castro, Jr., et al. (1998). "Degenerative conditions of the lumbar spine treated with intervertebral titanium cages and posterior instrumentation for circumferential fusion." J Spinal Disord **11**(6): 479-486.

Williams, J. M., A. Adewunmi, et al. (2005). "Bone tissue engineering using polycaprolactone scaffolds fabricated via selective laser sintering." Biomaterials **26**(23): 4817-4827.

Zhang, H., F. Migneco, et al. (2010). "Chemically-Conjugated Bone Morphogenetic Protein-2 on Three-Dimensional Polycaprolactone (PCL) Scaffolds Stimulates Osteogenic Activity in Bone Marrow Stromal Cells." Tissue Engineering Part A.

Zhong, Z. C., S. H. Wei, et al. (2006). "Finite element analysis of the lumbar spine with a new cage using a topology optimization method." Medical Engineering & Physics **28**(1): 90-98.